Graphitic Carbon Nitride Based Composite Photocatalyst for Methylene Blue Dye Degradation in Aqueous Solution

MINTESINOT TAMIRU MENGISTU

A Thesis Submitted to

The department of Materials Science and Engineering

School of Mechanical, Chemical, and Materials Engineering

Presented in Partial Fulfillment of the Requirement for the Degree of Master's in Materials Science and Engineering

Office of Graduate Studies

Adama Science and Technology University

Submission Date: June, 2022

Graphitic Carbon Nitride Based Composite Photocatalyst for Methylene Blue Dye Degradation in Aqueous Solution

MINTESINOT TAMIRU

Main Advisor: Dr. DINSEFA MENSUR ANDOSHE

Co-Advisor: Prof. JUNG YOUNG KIM

A Thesis Submitted to

The department of Materials Science and Engineering

School of Mechanical, Chemical, and Materials Engineering

Presented in Partial Fulfillment of the Requirement for the Degree of Master's in Materials Science and Engineering

Office of Graduate Studies

Adama Science and Technology University

Submission Date: June, 2022

Declaration

I hereby declare that this Master Thesis entitled “Graphitic Carbon Nitride Based Composite Photocatalyst for Methylene Blue Dye Degradation in Aqueous Solution” is my original work. That is, it has not been submitted for the award of any academic degree, diploma or certificate in any other university. All sources of materials that are used for this thesis have been duly acknowledged through citation

_____	_____	_____
Name of student	Signature	Date

Recommendation

I/we, the advisor(s) of this thesis, hereby certify that I/we have read the revised version of the thesis entitled “Graphitic Carbon Nitride Based Composite Photocatalyst for Methylene Blue Dye Degradation in Aqueous Solution “prepared under my/our guidance by Mintesinot Tamiru submitted in partial fulfillment of the requirements for the degree of Mater’s of Science in material science and engineering. Therefore, I/we recommend the submission of revised version of the thesis to the department following the applicable procedures.

_____	_____	_____
Major Advisor/Supervisor	Signature	Date
_____	_____	_____
Co-advisor/Co-supervisor	Signature	Date

Approval

I/we, the advisors of the thesis entitled “Graphitic Carbon Nitride Based Composite Photocatalyst for Methylene Blue Dye Degradation in Aqueous Solution” and developed by Mintesinot Tamiru hereby certify that the recommendation and suggestions made by the board of examiners are appropriately incorporated into the final version of the thesis.

_____	_____	_____
Major Advisor/Supervisor	Signature	Date
_____	_____	_____
Co-advisor/ Co-supervisor	Signature	Date

Approval of Board of Reviewers

We, the undersigned, members of the Board of Examiners of the thesis by Mintesinot Tamiru have read and evaluated the thesis entitled “Graphitic Carbon Nitride Based Composite Photocatalyst for Methylene Blue Dye Degradation in Aqueous Solution” and examined the candidate during open defense. This is, therefore, to certify that the thesis is accepted for partial fulfillment of the requirement of the degree of Master of Science in material science and engineering.

Chairperson	Signature	Date
Reviewer 1	Signature	Date
Reviewer 2	Signature	Date

Finally, approval and acceptance of the thesis is contingent upon submission of its final copy to the Office of Postgraduate Studies (OPGS) through the Department Graduate Council (DGC) and School Graduate Committee (SGC).

Department Head	Signature	Date
School Dean	Signature	Date
Office of Postgraduate Studies,	Dean Signature	Date

ACKNOWLEDGMENTS

First and foremost, I thank the Lord God Almighty for giving me the strength and grace to do this task. First and foremost, I'd like to thank my adviser, Dr. DINSEFA MENSUR ANDOSH, for his patience, advice, and constructive criticism. His advice was invaluable during my thesis study. I'd like to thank my co-adviser, Prof. JUNG YOUNG KIM, for his useful counsel and insightful comments. I'd like to thank the Material Science and Engineering program's Technical Staff, Mr. DEMEKE TESFAYE and Mr. HENOK MEKONEN, for their encouragement and assistance.

TABLE OF CONTENT

LIST OF FIGURES

LIST OF TABLES

ACRONYM

AOP	Advanced oxidation processes
BET	Brunauer-Emmett-Teller
CB	Conduction band
e^-	Electron
Eg	Bandgap energy
E_{CB}	Conduction band edge potential
E_{VB}	Valence band edge potential
EIS	Electrochemical Impedance Spectroscopy
FTIR	Fourier transforms infrared spectroscopy
GZC-1	Graphitic carbon nitride with 5wt% of zinc oxide and cobalt oxide each
GZC-2	Graphitic carbon nitride with 10wt% of zinc oxide and cobalt oxide each
GZC-3	Graphitic carbon nitride with 15wt% of zinc oxide and cobalt oxide each
GZC-4	Graphitic carbon nitride with 20wt% of zinc oxide and cobalt oxide each
GZC-5	Graphitic carbon nitride with 25wt% of zinc oxide and cobalt oxide each
h^+	Hole
MB	Methylene blue
PL	Photoluminescence
SEM	Scanning Electron Microscopy
UV–Vis	Ultraviolet-visible spectroscopy
XRD	X-Ray Diffraction

Abstract

Design and synthesis of artificial photocatalysts for dye removal from wastewater have become one of the key strategies to acquire treated water as a potential solution to global energy and environmental problems. Because of its unique features, graphitic carbon nitride (g-C_3N_4) has shown new potential uses in the photocatalytic field in recent years. However, the photocatalytic efficiency of virgin g-C_3N_4 is limited by its low surface area, narrow visible light absorbance, and high photo-induced electron-hole pair recombination rate. In this thesis, a simple wet impregnation method was employed to synthesize g-C_3N_4/ZnO/Co_3O_4 heterojunction photocatalysts with increased light absorbance, surface area, and efficient separation of photogenerated charge carries. To characterize the as-prepared samples, X-ray diffraction (XRD), scanning electron microscopy (SEM), UV-vis diffuse reflectance spectroscopy, photoluminescence spectroscopy (Pl), electrochemical impedance spectroscopy (EIS), Brunauer–Emmett–Teller (BET), and Fourier-transform infrared spectroscopy (FTIR) were used. XRD confirms the proper phase formation of g-C_3N_4, ZnO, and Co_3O_4. When g-C_3N_4 is formed into a composite, its surface area increases, and the use of cellulose as a template for the synthesis of ZnO and Co_3O_4 results in good dispersion, small grain size, and a high specific surface area. The measurement of the energy band gap of a g-C_3N_4/ZnO/Co_3O_4 composite showed redshifted optical absorption to the visible range. The PL intensity decreases due to heterojunction creation, and this PL quenching results in an enhanced rate of separation for photogenerated electron-hole pairs, as also seen by EIS. Under visible-light irradiation, the photocatalytic activity of the GZC-3 composites was about 8.2, 3.3, and 2.5-fold more than that of the g-C_3N_4, g-C_3N_4/ZnO, and g-C_3N_4/Co_3O_4 samples. The stability experiment revealed that GZC-3 demonstrates a relatively higher photocatalytic activity after 4 recycles. Based on Mott–Schottky plots of energy band matching within g-C_3N_4, ZnO, and Co_3O_4, a synergistic dual Z-scheme g-C_3N_4/ZnO/Co_3O_4 photocatalyst may be created. The developed photocatalyst could efficiently photodegrade MB dye. As a result, the eco-friendly photocatalyst could be widely used in the treatment of dye-contaminated wastewater.

Key words: g-C_3N_4/ZnO/Co_3O_4 composite, Photocatalyst, heterojunction, Photocatalytic degradation

CHAPTER ONE

1 Introduction

1.1 Overview

The ever-increasing global energy demand, excessive use of fossil fuels, and accompanying environmental difficulties such as greenhouse gas emissions and wastewater pollution are major challenges affecting society today. Organic dye is one of a significant source of contaminants. Organic contaminants in wastewater are very hazardous, and they have the potential to form carcinogens that are dangerous to humans, animals, and entire ecosystems (O'neill et al., 2000). There are approximately 10,000 different varieties of commercially used dyes, with an annual production of around 0.7 billion tons (Rajeshwar et al., 2008). Worryingly, around 1-20% of these colors are lost during the dyeing process and are discharged as textile effluents (Lellis, Fávaro-Polonio, Pamphile, & Polonio, 2019).

To protect the environment, more effective measures, such as limiting the discharge of toxic and potentially dangerous contaminants, must be implemented. To solve this problem, a variety of approaches such as ion exchange (Eom, Lee, Kim, & Lee, 2005), coagulation flocculation (Lee, Morad, Teng, & Poh, 2012), oxidation (Brodowska, Nowak, & Śmigielski, 2018), electrochemical treatment (S. Yuan, Li, & Wang, 2013), and membrane filtration (Hube et al., 2020) have been used to extract organic pollutants from contaminated sources. Among the numerous potential answers to this problem, photocatalysis has emerged as an intriguing approach because of its low cost, nontoxicity, safety, and renewable nature. Sunlight illumination may be used as an energy source in the photocatalytic process. Sunshine is a plentiful, clean, and safe energy source. The sun provides around 3×10^{24} J of energy to the earth's surface per year. This is four orders of magnitude greater than the global energy consumption for humanity. To carry out diverse catalytic processes, suitable semiconducting photocatalysts with enhanced absorbance over the whole solar spectrum area are required (Sang, Liu, & Umar, 2015). Previously, several semiconducting photocatalysts were developed to achieve efficient energy conversion employed for CO_2 reduction; water splitting to generate H_2 and O_2; and pollutant degradation and reduction (X. Li et al., 2019).

TiO_2, which was discovered in 1972 by Fujishima for photoelectrochemical water splitting, is the most extensively used photocatalyst today (Fujishima & Honda, 1972). This is a watershed moment in the realm of photocatalysts. The typical TiO_2 catalyst, on the other hand, must be

stimulated by UV irradiation, which accounts for less than 5% of the whole solar spectrum. This has prompted researchers to create innovative materials with lower bandgap energy (Eg) to improve sensitivity to increasingly plentiful visible light photons. As the visible-light-driven photocatalyst, many modified-TiO_2 or non-TiO_2 materials have been developed (Santosh Kumar, Karthikeyan, & Lee, 2018; C. Liu, Dong, & Chen, 2019; Na, Seo, & Lee, 2020; Yaghoubi et al., 2015; L. Zhang, Wang, Chen, Wong, & Liu, 2011).

Graphitic carbon nitride (g-C_3N_4) has lately received a lot of attention since it is the most stable allotrope of carbon nitride. g-C_3N_4 possesses $\prod$-conjugated planar layers akin to graphite, giving it great thermal and chemical stability as well as an attractive electrical structure (Xuefei Li et al., 2009). As a result, it could be used as a direct semiconductor catalyst in sustainable chemistry. g-C_3N_4 has distinct properties such as a good electrical and optical structure, as well as strong photochemical stability, and is considered a potential photocatalyst (Chang et al., 2013; Song, Zhang, Wu, & Wei, 2012). g-C_3N_4 has been shown to function well in photo-degrading organics when exposed to visible light (Yong Wang et al., 2010). However, the photocatalytic efficiency of g-C_3N_4 is far from ideal due to low surface area, narrow visible light absorption, and high recombination rate. Several ways have been used to overcome these limitations. Since g-C_3N_4 has a stacked layered structure which results to have limited surface area, several chemical, and physical approaches have been used to break the weak van der waals forces between stacked layers of g-C_3N_4. Exfoliation of g-C_3N_4 into nanosheets not only gives a high surface area with a large number of active sites, but it also has the benefit of having a shorter diffusion length with a low recombination rate probability when compared to bulk g-C_3N_4 (F. Dong, Li, Wang, & Ho, 2015; Yanping Liu et al., 2021; Niu, Zhang, Liu, & Cheng, 2012; L. Yang et al., 2018).

Doping with metals and nonmetals has also been found to be an effective method for increasing visible light absorption using bandgap engineering. Nonmetal doping because of their high ionization energies and electronegativity, May easily form covalent bonds with other compounds by accepting electrons during the reaction. Nonmetal insertion, in general, disrupts the symmetry of g-C_3N_4 and causes electron-hole couples to separate faster. The nonmetallic dopants include oxygen (Putri et al., 2020), phosphorus (K. Zhao, Khan, Qi, Liu, & Khataee, 2020), sulfur (Jourshabani, Shariatinia, & Badiei, 2017), carbon (Jourshabani et al., 2017), halogen (Jiadong Li et al., 2017),and boron (Lei et al., 2021) could narrow the bandgap of g-C_3N_4 and enhance its light-

harvesting capability. Theoretical calculations revealed that when the phosphorous atom occupied the C1 position, the bandgap decreased from 2.70 eV to 2.22 eV. As a result, more visible light may be produced while also creating more excited electrons (S. Guo et al., 2017). Qiao's group showed that P-doping porous g-C_3N_4 nanosheets can drastically narrow the intrinsic bandgap from 2.98 to 2.66 eV and promote photo-excitation of electrons from the VB of P-doped g-C_3N_4, due to the formation of vacant midgap states below the CB minimum of g-C_3N_4 through the hybridization of C 2s2p, N 2s2p, and P 3s3p as a result, visible light absorption is improved (Ran, Ma, Gao, Du, & Qiao, 2015).Concerning of high recombination rate in gC_3N_4 can be suppressed by noble metal loading on g-C_3N_4 surface or coupling it with other semiconductors such as TiO_2/g-C_3N_4 (Ali & Kim, 2021), graphene oxide/gC_3N_4 (Tong et al., 2015),Au/g-C_3N_4 (P. M. Mishra, Pattnaik, & Devi, 2021)/g-C_3N_4/α-Fe_2O_3 (Khurram, Nisa, Javed, Wang, & Hussien, 2022),g-C_3N_4/Ag_2O/TiO_2 (Long et al., 2021),g-C_3N_4/Bi_2WO_6 (Opoku, Govender, van Sittert, & Govender, 2018), Ag/g-C_3N_4 (Thorat et al., 2019), g-C_3N_4 /Co_3O_4/V_2O_5 (Palanisamy et al., 2021), Cu doped ZnO/g-C_3N_4 (Ahmad, 2020), g-C_3N_4 /Co_3O_4 (Han et al., 2014)etc. ZnO is an attractive inexpensive and non-toxic semiconductor material with good application prospects in the fields of photoelectric conversion, photoelectric sensor, and photocatalysis having a wide direct bandgap of 3.2 eV to 3.3 eV a self-activated semiconductor material (Amutha et al., 2014; Y. Hong et al., 2013; J. Wang, Chen, Xiang, & Komarneni, 2018). It has been reported that ZnO coupled g-C_3N_4 composites have been shown to increase the oxidation potential and removal efficiency of inorganic and organic contaminants such as rhodamine B and methylene blue. However, due to the decreased absorption of visible light in the solar spectrum, the application of g-C_3N_4/ZnO composite has restricted activity in the visible light area. To solve this issue, a p-type transition metal oxide semiconductor (Co_3O_4) with a high surface area, great thermal stability, non-toxicity, and excellent optical property energy bandgap (2.1 eV) can be used (Yile Wang et al., 2020).

In this present work, the ternary photocatalyst of g-C_3N_4/ZnO/Co_3O_4 composite was prepared through a simple wet impregnation process. For the synthesis of metal oxide, we have used cellulose extracted from enset fiber as a template since hydroxyl group on cellulose act as efficient hydrophilic substrates for the nucleation and growth of metal oxide, giving high specific surface area and pore size distribution. A variety of analytical techniques were used to evaluate the synthesized samples. Their catalytic activities were evaluated by the degradation of methylene blue (MB), under visible light irradiation.

1.2 Statement of the Problem

The unique fascinating photocatalytic properties of g-C_3N_4, such as a good electrical, and optical structure, strong photochemical stability, good redox capacity, and easy preparation makes it the focus of attention in recent decades and considered a potential photocatalyst (R. He, Liang, Li, & Bai, 2020). The photocatalytic activity of g-C_3N_4 remains unconvincing for practical applications due to three fundamental issues. To begin with, graphitic carbon nitride has a low surface area (10 m^2g^{-1}) (Dyjak, Kiciński, & Huczko, 2015; Tian, Liu, Asiri, Sun, & He, 2015; Z. Wang et al., 2015; X.-S. Zhang, Tian, Hu, & Jiang, 2015). In addition, to limited visible light absorption, the bandgap for g-C_3N_4 is 2.7 eV, which corresponds to a threshold wavelength of approximately 460 nm, which is still too large for efficient visible-light harvesting and leaves the majority of the visible light spectrum unexplored (Tay et al., 2015). Finally, due to the high recombination rate of produced charge carriers, the radical species responsible for the redox reaction during photocatalysis do not develop effectively. These three essential parameters determine the photocatalytic ability of materials. Few studies have combined all of the aforementioned strategies to improve the photocatalytic properties of g-C_3N_4. The present research aims to improve not only visible light absorption but also electron-hole pair separation and active surface area. As a result, in this study, bulk g-C_3N_4 was exfoliated to attain a higher active surface area with a greater number of exposed active sites. Following that, ZnO and Co_3O_4 heterojunction g-C_3N_4 to minimize the rate of electron-hole pair recombination. Thus, the current study provides a complete analysis of integrating all of the above-mentioned methodologies and their influence on improving the performance of g-C_3N_4 towards industrial dye degradation.

1.3 General Objective

Graphitic Carbon Nitride Based Composite Photocatalyst for Methylene Blue Dye Degradation in Aqueous Solution.

1.3.1 Specific Objectives

- Extracting cellulose from enset fiber
- Synthesizing g-C_3N_4 with an easy thermal polymerization method
- Synthesizing ZnO and Co_3O_4 with a chemical precipitation method
- Synthesizing g-C_3N_4/ ZnO/ Co_3O_4 composite with a simple wet impregnation method

- Characterizing the synthesized materials by using different materials and to evaluate the photocatalytic activities towards a photodegradation of methylene blue

1.4 Significance of the Study

It has been a huge problem in the contemporary period to provide clean water for those who consume freshwater. More than 1000 industrial-origin organic compounds have been found in various water sources (Hignite & Azarnoff, 1977). Pharmaceuticals, surfactants, flame retardants, perfumes, plasticizers, and other trace chemicals, which are often associated with human ailments, have been discovered in discharged wastewater (Focazio et al., 2008). In Ethiopia every year, over 62 million people lack adequate sanitation facilities, and over 2.1 million die as a result of illnesses caused by polluted water (Gizaw, 2014). As a result, organic contaminants in wastewater have posed a major hazard to human health. The threat of organic contaminants in the water is serious because most organic molecules are hazardous and seldom self-degrade in nature. The goal of this thesis is to design and fabricate efficient g-C_3N_4-based photocatalysts with enhanced photocatalytic activities under visible light irradiation so that they can be effectively used for manufacturing industries to treat large amounts of contaminated water because the material is cost-effective, can be synthesized in mass production, and the method is simple to implement.

CHAPTER TWO

2 Background and Literature Review

2.1 Basic Principles of Photocatalysis

The term "photocatalysis" first appeared in scholarly literature in 1911. The use of sunlight to assist chemical processes is known as photocatalysis. The well-known energy band theory helps explain the physical mechanisms of heterogeneous photocatalysis in general (Fox & Dulay, 1993). The theory explains the semiconductor band structure arrangement, in which the valance band (V_B) consists of a series of closely spaced energy levels that arise from covalent interactions between atoms and another series of continuums lying at the upper energy state known as the conduction band (C_B), which is associated with the conduction properties of a semiconductor.

The bandgap is a fixed energy gap (E_g) that separates the electrically fully occupied V_B and the unoccupied C_B at absolute zero, which also specifies the semiconductor's susceptibility to irradiation wavelength. As seen in Figure-2.1, the fundamental mechanism of heterogeneous photocatalysis has been well proposed. In general, heterogeneous photocatalysis contains seven critical phases that may be divided into three basic processes: light-harvesting and charge excitation (step 1), charge separation and transfer (step 2), and surface electrocatalytic reactions (step 3).

When a semiconductor catalyst is irradiated with photons with energies equivalent to or greater than the E_g of the semiconductor, an electron (e^-) is promoted from the V_B to the C_B, leaving a hole (h^+) in the V_B thereby accumulating photogenerated electrons in the C_B and holes in the V_B as illustrated in Figure-2.1 (step one). The accumulated electrons and holes subsequently migrate to the surface Figure-2.1 (step two). Energetic enough electrons and holes that migrate to the surface of the semiconductor without recombination can be trapped by the surface active sites and further stimulate the electrocatalytic reduction and oxidation reactions of the reactants adsorbed on the semiconductor, respectively as illustrated in Figure-2.1 step-3 (B. P. Mishra & Parida, 2021; P. Mishra, Patnaik, & Parida, 2019). The holes that are localized on the surface can either oxidize the pollutant directly or can react with H_2O/OH to produce hydroxyl radicals ($OH^{\bullet}$). The photogenerated electron that is localized on the surface can either reduce the pollutant directly or can react with adsorbed oxygen to produce a the $O_2^{\bullet}$ radicals. Unfavorable charge recombination in the bulk and on the surface of a semiconductor is detrimental to charge separation and transfer

to surface/interface active sites, which has been viewed as the determining factor for photocatalytic quantum efficiency (Schneider et al., 2014). There have been several semiconductor materials utilized up to this point, but recently graphitic carbon nitride has garnered a lot of interest in the field of photoctalysis.

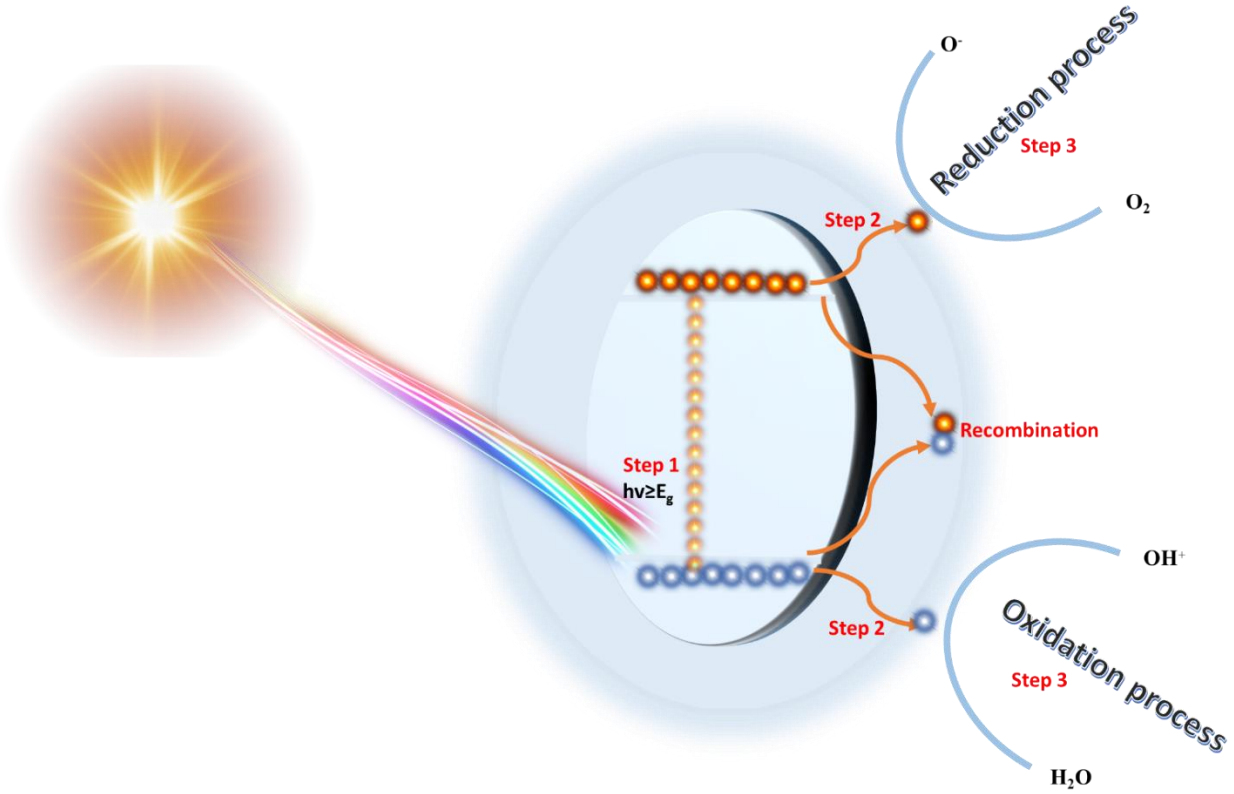

Figure-2.1 The fundamental mechanism of heterogeneous photocatalysis.

2.2 Graphitic Carbon Nitride (g-C_3N_4)

Graphitic carbon nitride (g-C_3N_4) has a stacked 2D layered structure with an interplanar spacing of 0.326 nm and is connected by weak van der Waals interactions (Manimozhi, Mathankumar, & Prakash, 2021). It is also a metal-free semiconducting material that has drawn significant attention towards photocatalysis for its excellence in the field. In recent years, there has been a rise in interest in g-C_3N_4-based photocatalysis. According to Figure-2.2, there is a rising interest in using g-C_3N_4 as a photocatalyst for environmental remediation (Alaghmandfard & Ghandi, 2022).

The photocatalytic effectiveness of g-C_3N_4 based photocatalysts is primarily determined by the crystal structure, surface physicochemical, stability, optical, adsorption, electrochemical, photoelectrochemical, and electronic characteristics of g-C_3N_4. As a result, basic knowledge and

deterministic control of these chemical and structural parameters will allow for the scalable manufacturing of g-C_3N_4 photocatalyst with optimal photocatalytic performance. Thereby some of the fundamental properties of g-C_3N_4 are discussed below.

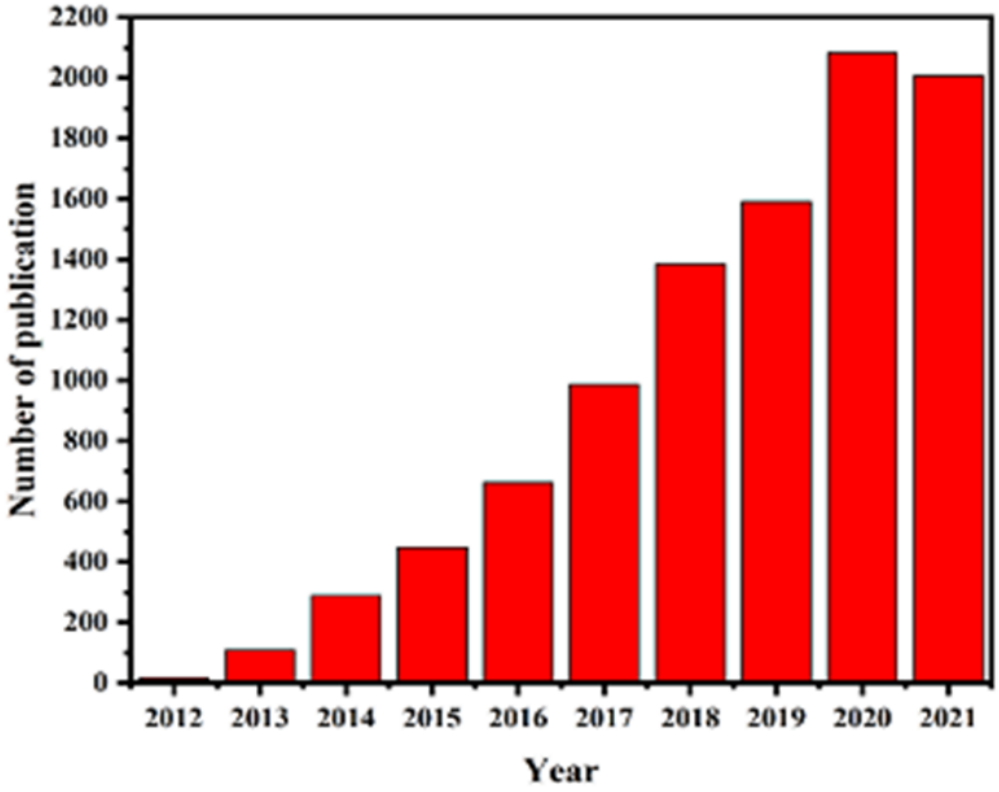

Figure-2.2 Number of annual publications (a) using "g-C_3N_4" as a keyword since 2012 (Alaghmandfard & Ghandi, 2022).*

2.2.1 Structural Properties of Graphitic Carbon Nitride

Although g-C_3N_4 does not exist in nature, it can be easily synthesized from inexpensive nitrogen-rich organic precursors such as urea, melamine, melamine hydrochloride, cyanamide, thiourea, and dicyandiamide Figure-2.3 (a) (J. Zhu, Xiao, Li, & Carabineiro, 2014). Graphitic Carbon Nitride is the most stable carbon nitride allotrope under ambient conditions. There are seven distinct phases in g-C_3N_4, including alpha-C_3N_4, beta-C_3N_4, cubic C_3N_4, pseudocubic C_3N_4, g-h-triazine, g-h-heptazine, and g-o-triazine, with band gaps of 5.49, 4.85, 4.30, 4.13, 2.97, 2.88, and 0.93 eV (Y. Xu & Gao, 2012). Among seven phases, except for the pseudocubic and g-h-triazine phases, possess indirect band gaps in their bulk structures (Maeda et al., 2009; Teter & Hemley, 1996; Y. Xu & Gao, 2012). The g-h-triazine and g-heptazine phases have appropriate band gaps

for visible-light absorption of 2.97 and 2.88 eV, respectively, supporting their usage in diverse photocatalytic domains.

Graphitic Carbon's Structure Nitride is similar to graphite in that the carbon lattice is periodically replaced with nitrogen atoms (Xinchen Wang et al., 2009; J. Zhu et al., 2014). There are two types of g-C_3N_4 structural isomers: one made of s-triazine Figure-2.3 (b) and another made of tri-s-triazine Figure-2.3 (c). The Planar structures are formed by connecting different repeating units with tertiary amino groups. The tri-s-triazine building blocks are more energetically stable than the s-triazine units, according to both experimental and DFT calculations (Kroke et al., 2002; Thomas et al., 2008).

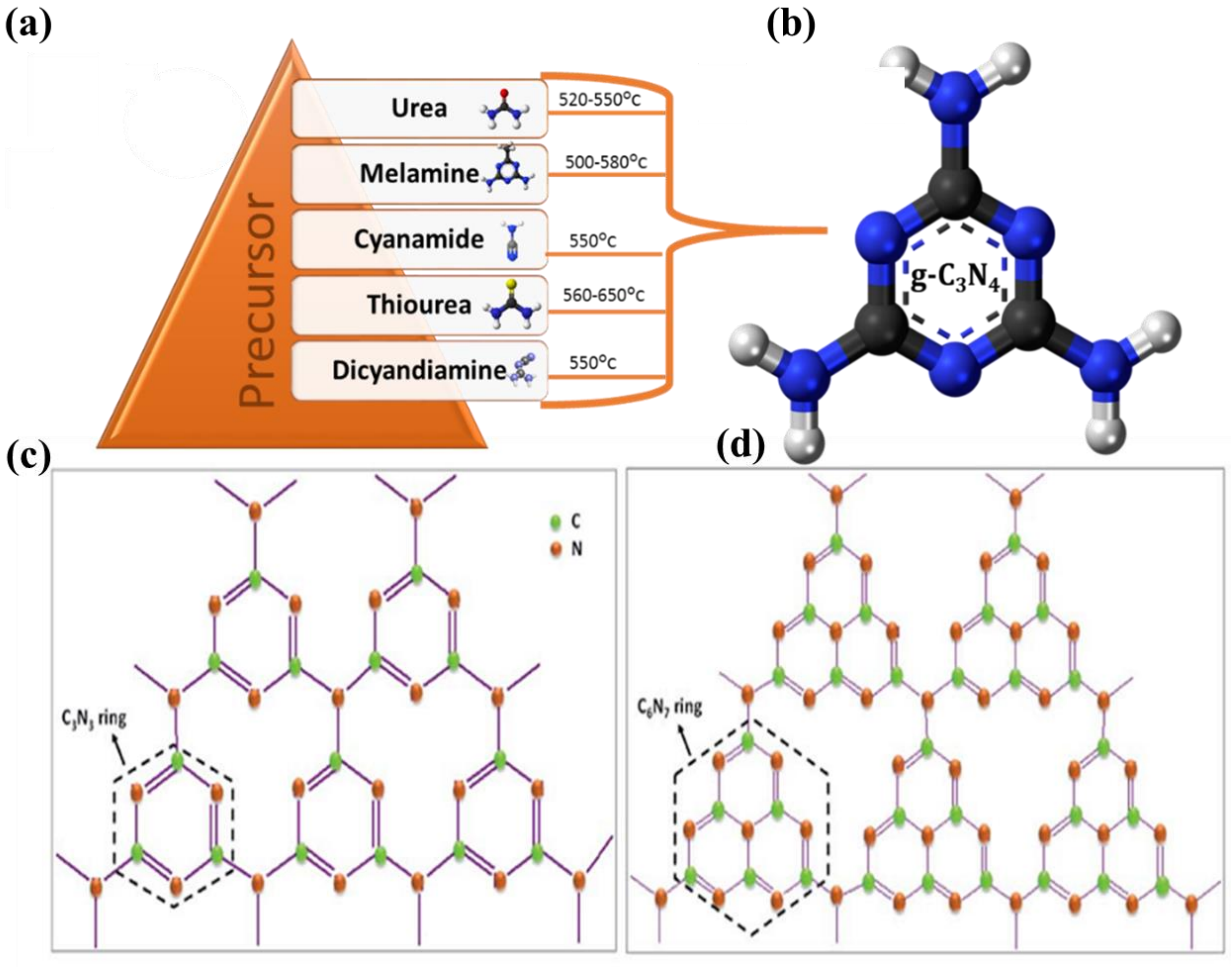

Figure-2.3 (a) Synthesis precursors and calcination temperature for g-C_3N_4 preparation. (b and c) s-triazine and tri-s-triazine structures of g-C_3N_4 (Kong et al., 2021).

2.2.2 Surface Physicochemical Properties

Several surface imperfections on the surface of g-C_3N_4 material are known to cause the formation of multiple functionalities. During the polycondensation process, primary and/or secondary amine groups (e.g., CNH_2 and C_2NH) on the terminal edges of the single layer of g-C_3N_4 as seen in Figure-2.4 may be produced by a trace quantity of hydrogen impurity (Thomas et al., 2008; J. Zhu et al., 2014). As a result, it is not surprising that g-C_3N_4 materials with surface defects and electron-rich properties also exhibit the distinctive nucleophilic character from basic surface functionalities for CO_2 activation or H-bonding motifs as shown in Figure-2.4, allowing them to be more valuable in catalysis than defect-free g-C_3N_4 materials (Thomas et al., 2008). However, the hydrophobic nature of the nanocarbon surface may result in the formation of a weakly interacting interfacial layer which greatly limits electron transit and separation as well as surface electrocatalytic processes (Lingyu Zhou et al., 2016).

According to the studies, the hydrophilicity of g-C_3N_4 materials can be improved further by introducing oxygen-containing functional groups (hydroxyl and carboxyl) via chemical oxidation, which greatly improves their dispersion in aqueous solutions while also improving interfacial coupling and photocatalytic activities (J. Yuan, Yi, Tang, Liu, & Luo, 2020). Modification of functional groups in the g-C_3N_4 structure can boost photocatalytic activity by adding active sites, enhancing hydrophilicity, and facilitating charge separation (Meng et al., 2018). Furthermore, the many basic groups (NH, N, NH_2, and NC) on the surface of g-C_3N_4 are clearly understood to be useful for the removal of acidic hazardous compounds by chemical adsorption based on electrostatic interactions (Yingai Li et al., 2010). Material stability is another significant property in the field of phtocatalysis.

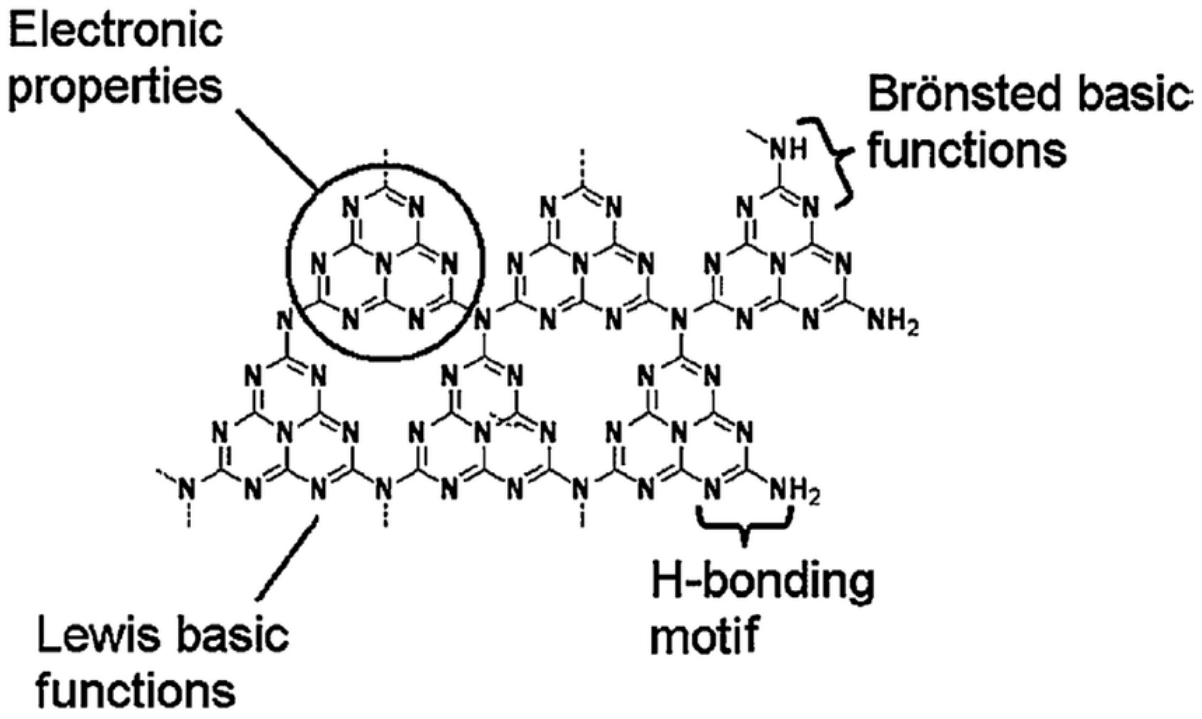

Figure-2.4 Multiple functional surface properties of polymeric g-C_3N_4 material with defects (Thomas et al., 2008).

2.2.3 Stability Properties

Figure-2.5 (a) the thermogravimetric analysis for g-C_3N_4 indicated that TGA curves of g-C_3N_4 were obtained under different conditions, demonstrating that the material is stable up to 600˚C, either in N_2, O_2, or air atmosphere. This indicates that g-C_3N_4 can resist high temperatures, even in an oxidizing atmosphere, and that weight loss over 600°C is caused by direct thermal disintegration rather than oxidation by O_2 (to generate oxides such as CO or CO_2) (J. Zhu, Wei, Chen, Zhao, & Thomas, 2010).

Figure-2.5 (b) shows TG-DSC analysis, indicating that melamine sublimation and thermal condensation occur at temperatures ranging from 297 to 390˚C, as determined by strong endothermic DSC, de-ammoniation (545°C), and subsequent oxidation breakdown (630–750˚C) of g-C_3N_4 material. The total decomposition temperature of g-C_3N_4 ranges from 700 to 750˚C, which is consistent with the findings of Gillan (Cui et al., 2011; Gillan, 2000). Furthermore, graphitic carbon nitride is insoluble in water, most acids and bases, and organic solvents (Thomas et al., 2008; Yong Wang, Wang, & Antonietti, 2012). However, there have been reports of exceptions when the material has been treated with molten alkali metal hydroxides and strong

acids (Y. Zhang, Thomas, Antonietti, & Wang, 2009). According to studies, utilizing various chemicals can change the electrical properties of graphitic carbon nitride.

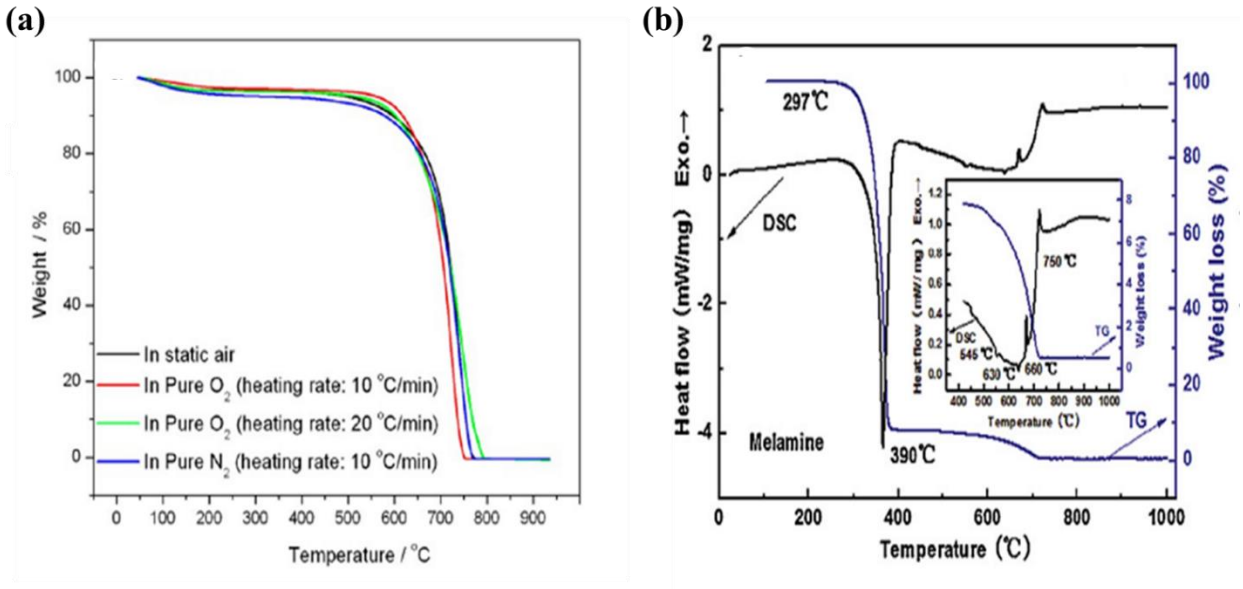

Figure-2.5 (a) TGA curves for g-C_3N_4 conducted in different atmospheres. (b) TG-DSC thermograms for heating the melamine (Yan, Li, & Zou, 2009).

2.2.4 Electronic Properties

It is generally understood that appropriate electrical characteristics play critical roles in improved photocatalysis. Density-functional-theory (DFT) computations were used to get detailed oxidation and reduction levels of valance and conduction bands to gain insight into its electronic structure. The results reveal that the highest occupied molecular orbital/lowest unoccupied molecular orbital (HOMO-LUMO) gaps of a melem molecule, polymeric melon, and an infinite sheet of a hypothetically totally condensed g-C_3N_4 were 3.5, 2.6, and 2.1 eV, respectively (Xinchen Wang et al., 2009). Polymeric melon's calculated band gap is quite near to the experimentally determined medium-band gap of 2.7 eV (Wen, Xie, Chen, & Li, 2017). The valence band (Figure-2.6 (a)) and conduction band (Figure-2.6 (b)) wave function studies are mainly derived from nitrogen Pz orbitals and carbon Pz orbitals, which serve as oxidation and reduction sites for O_2 and H_2 evolution processes, respectively (Mamba & Mishra, 2016; Ye, Wang, Wu, & Yuan, 2015).

Aside from DFT computations, the band edge locations of g-C_3N_4 materials may be established using electrochemical impedance spectra (EIS) and valence band X-ray photoelectron spectra

(VB-XPS), respectively (Xin Li et al., 2015). Wang et al. used the M–S technique to determine the flat-band potentials of bulk g-C_3N_4, revealing that the conduction band and valance band edges are positioned at -1.3 and 1.4 V versus NHE at pH 7, respectively (X Wang, Blechert, & Antonietti, 2012; Jinshui Zhang et al., 2010; Y. Zheng, Lin, Wang, & Wang, 2015). Meanwhile, Yan et al. (Yan, Lv, Li, & Zou, 2010) used the VB-XPS method to get precise conduction band and valance band edges of bulk g-C_3N_4 at 1.53 and 1.16 V vs NHE at pH 7, respectively (Yan et al., 2010). However, these two outcomes appear to be slightly contradicting. The primary cause is that many researchers confuse the flat-band potential with the conduction band potential. In reality, the conduction band potential of an n-type semiconductor is roughly -0.1 to -0.2 V more negative than the flat-band potential (Xin Li et al., 2015). Considering the tiny discrepancy (0.2 V) between the flat-band potential and the conduction band potential, there was full agreement between these two experimental outcomes.

Because g-C_3N_4 has a suitably negative CB, the CB electrons on its surface have gained a high reducing capacity that may be employed for the evolution of H_2 via photocatalytic water splitting, CO_2 reduction, and organic pollutant degradation, and different chemical synthesis processes (Mamba & Mishra, 2016). Furthermore, the underlying electrical characteristics and charge carrier dynamics, including the microscopic dynamic processes of charge creation, recombination, separation, and transfer, are important in determining photocatalytic performance (Xin Li et al., 2015; N. Zhang, Yang, Liu, Sun, & Xu, 2015). Thus, a thorough understanding of electrical characteristics and charge carrier dynamics is critical for designing and building more efficient and stable g-C_3N_4-based photocatalysts.

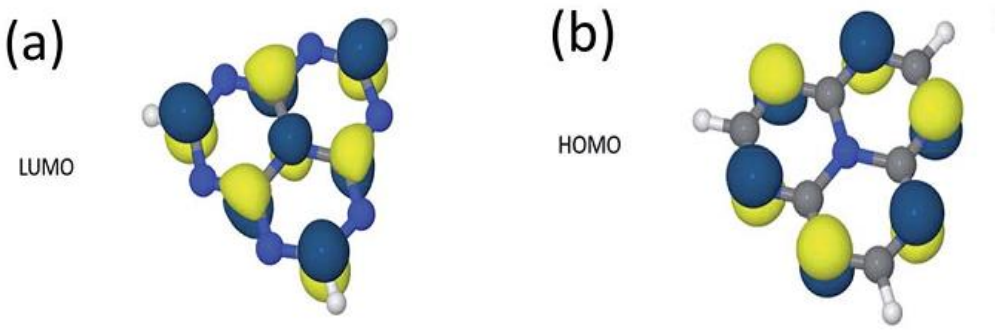

Figure-2.6 (a) Hartree Fock orbitals for the HOMO and LUMO of the heptazine water system calculated with the aug cc pVDZ basis set (Ehrmaier, Domcke, & Opalka, 2018).

2.3 Preparation of g-C_3N_4

Several methods for synthesizing g-C_3N_4 with diverse structures and electronic properties have been researched. Such methods include chemical vapor deposition (CVD), solvothermal, physical vapor deposition (PVD), ionothermal synthesis, single-step nitridation, solid-state, sonochemical, and thermal condensation (Schwinghammer et al., 2014; Sobahi & Amin, 2019; Thomas et al., 2008; Xinchen Wang et al., 2009). Thermal condensation of nitrogen-rich precursors, on the other hand, has proven to be the most appealing approach for preparing g-C_3N_4 for large-scale manufacture due to its simplicity and use of affordable, widely available precursors. It starts with N-rich organic molecules that polymerize into g-C_3N_4 by a simple calcination process at temperatures ranging from 450 to 650°C [114].

On a large scale, g-C_3N_4 is synthesized by pyrolysis of urea under ambient pressure without the use of any additives. This approach consists of four phases. First, at a low temperature (200°C), urea ($CO(NH_2)_2$) is pyrolyzed to isocyanic acid (HNCO). Isocyanic acid is then transformed into cyanuric acid, which is then turned into melamine via self-supported NH_3 (g). Melamine is then condensed at roughly 390 °C to generate melam, which then self-condenses to form melem ($C_6H_6N_{10}$). Melem is subsequently pyrolyzed and condensed at 500 °C to yield melon ($-[C_6H_3N_9]_n$) with a low degree of polymerization. Finally, these melon are further condensed at 520–550 °C to create g-C_3N_4 with a high degree of polymerization. Figure-2.7 (a) depicts a schematic illustration of the synthesis process of g-C_3N_4 from urea pyrolysis, as discussed previously (Amorin et al., 2019; Bernhard, Peitz, Elsener, Wokaun, & Kröcher, 2012; Schaber, Colson, Higgins, & Thielen, 2004; Thomas et al., 2008; J. Xu et al., 2013).

The hydrothermal technique of this nanomaterial synthesis technology offers various advantages, including the capacity to synthesize products with a rapid crystal growth rate, high purity, good crystal structure, and low agglomeration. It reduces the potential of impurities and structural faults, which are frequently caused by high-temperature calcination or certain post-treatment [117,118]. Furthermore, the as-obtained compounds had lower bandgap energy, better charge transfer and separation, and higher photocatalytic activity. Low yields, the requirement for specialized equipment and organic solvents, and waste liquor treatment are also possible downsides. Currently, a diverse variety of g-C_3N_4 with distinct nanoarchitecture and multidimensional morphology has

been widely produced by varying the reaction temperature, pressure, and solvent type, as well as the addition of catalysts and additives.

The electrochemical deposition (ECD) method not only uses simple equipment, operates at a low temperature, and is easy to control, but it also effectively decreases the energy barrier of the C–N bonding process (Q. Lu et al., 2015). For example, Bai et al (Bai, Li, & Cao, 2010). Used a silica nanosphere template to describe a simple and effective electrodeposition strategy for generating hollow g-C_3N_4 microspheres. They created g-C_3N_4 microspheres with numerous nanoparticles using dicyandiamide as a precursor in an acetone solvent for 10 minutes at 50°C and 1200V. The dicyandiamide precursor will be polarized and broken by the high fields surrounding the silicon sphere at the electrode surface, creating a certain quantity of high nitrogen CN_x clusters, which is conducive to the creation of g-C_3N_4 nanoparticles. In atmospheric circumstances and at lower temperatures, the ECD technique helps regulate the synthesis of g-C_3N_4 with particular nanostructures. Furthermore, due to the insolubility of g-C_3N_4 powder, it is difficult to generate a film with a large area and smooth surface using the typical wet-process (Gu et al., 2017; J. Xu & Shalom, 2016). As a result, one of the most often used methods for creating well-dispersed g-C_3N_4 thin films with large surface areas is the ECD method (Ou, Wang, Wu, Zhao, & Wang, 2019). The ECD method, on the other hand, necessitates the use of specialized electrolysis apparatus and current, increasing the difficulty and cost of the preparation operation. As a result, it is far less common than the two previously mentioned methods.

Along with the general direction of green, controllable, and refined over the last decade, various new methods for synthesizing g-C_3N_4 based nanomaterials, such as copolymerization (Jinshui Zhang et al., 2010), chemical vapor deposition (Ying Liu, Yu, & Zhang, 2014; Yangang Wang, Wang, Zuo, Zhang, & Cui, 2014; Yadav et al., 2020), and microwave-assisted methods (Hu, Chu, Wang, & Wu, 2017; Y. Yu, Zhou, & Wang, 2016), have been extensively developed.

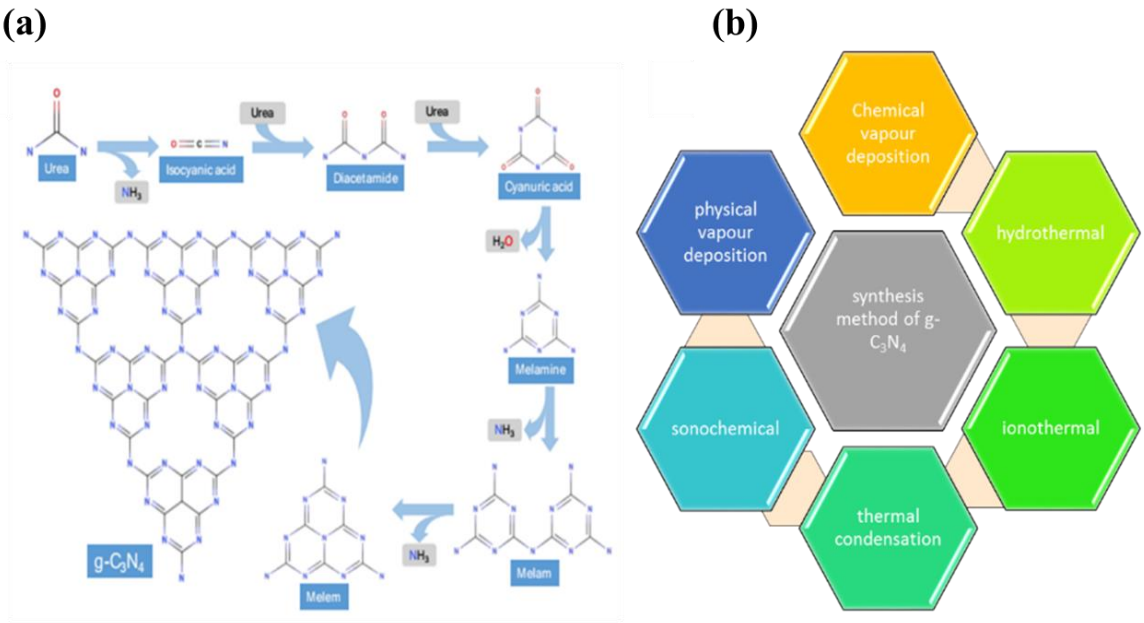

Figure-2.7 (a) Schematic representation For the synthesis process of the g-C_3N_4 from urea pyrolysis (Amorin et al., 2019), (b) synthesis methods for graphitic carbon nitride.

2.4 Modification of g-C_3N_4 for Improved Photocatalytic Activity

Despite its remarkable electronic, optical, and simple synthesis mechanisms, the photocatalytic activity of g-C_3N_4 remains unconvincing for practical applications due to the strong recombination of photogenerated electron-hole pairs, low surface area and narrow absorption of visible light the degrading ability of this metal-free polymeric photocatalyst remains limited. Numerous efforts have been made to improve the g-C_3N_4 to get an ideal photocatalyst such as surface modification, doping, composite, etc.

2.4.1 Surface Enhancement of g-C_3N_4

Because g-C_3N_4 has a stacked layered structure with a restricted surface area, numerous chemical and physical techniques have been explored to break the weak van der waals forces between the stacked layers. When compared to bulk g-C_3N_4, exfoliation of g-C_3N_4 into nanosheets provides not only a high surface area with a large number of active sites but also a shorter diffusion length with a low recombination rate likelihood (G. Dong, Zhang, Pan, & Qiu, 2014; Santosh Kumar, Surendar, Kumar, Baruah, & Shanker, 2014; Schwinghammer et al., 2014). Because holes are substantially less mobile than electrons [106], the increased surface area may enhance hole

migration to the surface and subsequent reactions rather than hole recombination with electrons and energy loss (Fonash, 2010).

Graphitic carbon nitride synthesized via thermal polycondensation of melamine or dicyandiamide, a common N-rich precursor, generally shows a limited surface area (<10 m^2 g^{-1}) Figure-2.8 (a). The enhanced surface area and photocatalytic activity of urea-based g-C_3N_4 are most likely attributable to a substantial quantity of gaseous by-product emission (e.g., NH_3, H_2O) in thermal polycondensation. Several strategies have taken advantage of the by-product formation of gaseous by-products by adding a precursor with low thermal stability to create pores and improve the surface area. For example, for g-C_3N_4 synthesis, NH_4Cl was blended with dicyandiamide, and the precursors produced g-C_3N_4 nanosheets with a significantly increased surface area (52.9 vs. 2.9 m^2 g^{-1}) Figure-2.8 (b) (X. Lu et al., 2014).

To expand the surface area of g-C_3N_4, a more advanced supramolecular technique, also known as soft templating was used. In brief, the precursors (e.g., melamine and cyanuric acid) form a supramolecular complex by hydrogen bonding, and they create porous g-C_3N_4 during thermal polycondensation since one precursor (cyanuric acid) is thermally unstable and decomposes into gaseous by-products. According to Zheng et al (Q. Zheng et al., 2016). The surface area was increased 8.0-fold, from 9.8 m^2 g^{-1} (melamine-based g-C_3N_4) to 78.8 m^2 g^{-1} (melamine–cyanuric acid-based g-C_3N_4 Figure-2.8 (c) (Q. Zheng et al., 2016).

Thermal exfoliation and liquid exfoliation are the two most commonly explored techniques for producing g-C_3N_4 nanosheets with a considerably greater surface area to boost photocatalytic activity (Jinshui Zhang, Chen, & Wang, 2015). To summarize, as bulk g-C_3N_4 is synthesized, it is exposed to post-thermal treatment in the air (e.g., 500°C) or ultra-sonication in a solvent with favorable surface energy (e.g., water, isopropanol) to form g-C_3N_4 nanosheets. After thermal exfoliation Figure-2.8 (d) and liquid exfoliation Figure-2.8 (e), the surface area of the nanosheets reached 306 or 384 m^2 g^{-1}, respectively (Niu et al., 2012; S. Yang et al., 2013).

The hard templating approach, which is nearly identical to the conventional casting process, employs thermally resistant hard templates (e.g., silica nanoparticles, ordered mesoporous silica, anodic aluminum oxide, and calcium carbonate) to design a variety of g-C_3N_4 structures and geometries and to build hierarchical pore architectures (Ong, Tan, Ng, Yong, & Chai, 2016). This method resulted in well-defined pore diameters and g-C_3N_4 distribution, as well as a considerably

enhanced surface area (517 m^2 g^{-1}) Figure-2.8 (f) (Jinshui Zhang, Guo, & Wang, 2013). However, the post-treatment of removing hard templates with corrosive, hazardous chemicals (e.g., HF, NH_4HF_2) to generate pores may restrict large-scale, sustainable g-C_3N_4 material manufacturing.

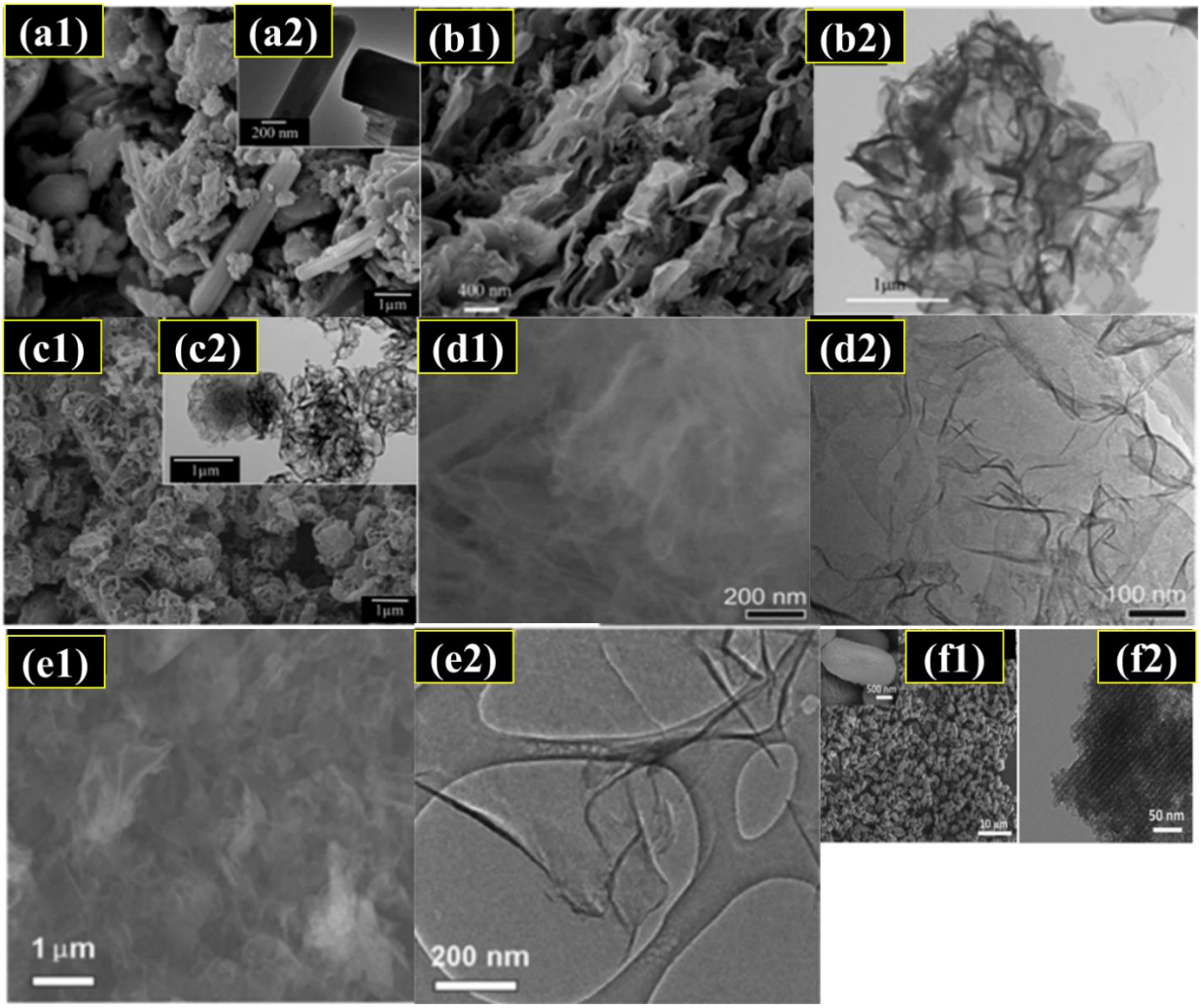

Figure-2.8 (a1 and a2) Scanning electron microscopy and (b1 and b2) transmission electron microscopy of g-C_3N_4 synthesized from melamine (Q. Zheng et al., 2016),(X. Lu et al., 2014), (c1 and c2) g-C_3N_4 nanosheets synthesized from dicyandiamide and NH4Cporous g-C_3N_4 synthesized from melamine and cyanuric

acid via a supramolecular method (Q. Zheng et al., 2016), (d1 and d2) g-C_3N_4 nanosheets synthesized via thermal exfoliation (Niu et al., 2012), (e1 and e2) g-C_3N_4 nanosheets synthesized via liquid exfoliation (S. Yang et al., 2013), and (f1 and f2) mesoporous g-C_3N_4 synthesized using silica as a hard template (Jinshui Zhang et al., 2013).

2.4.2 Doping Graphitic Carbon Nitride

Many researchers have worked on improving the absorption of graphitic carbon nitride by doping to move the absorption of graphitic carbon nitride to a more visible range. In general, the introduction of metallic impurities causes new binding functions, endowing the doped system with unique photocatalytic capabilities by reducing the bandgap and increasing visible light absorption (Tonda, Kumar, Kandula, & Shanker, 2014; Xiong, Cen, Zhang, & Dong, 2016; J. Xu et al., 2014). To introduce metal ions into the carbon nitride framework, the relevant soluble salt is evenly mixed with the g-C_3N_4 precursor during the thermal condensation process. While the graphitic carbon nitride precursor undergoing polymerization, metallic impurities will be doped into the g-C_3N_4 framework at the same time.

Hu et al (Shaozheng Hu et al., 2015). Prepared g-C_3N_4 Using dicyandiamide and potassium hydrate as precursors and dopants respectively, with different concentrations of potassium (0.02, 0.05, 0.07, and 0.09 M) on g-C_3N_4. Based on XRD analysis with varied potassium content, no peak for a potassium-related species is detected, although an apparent shift toward a lower 2θ value was observed for all potassium catalysts, as shown in Figure-2.9 (a). This is probably due to potassium doping into the interstitial sites as shown in Figure-2.9 (b) of in-planar g-C_3N_4, which enlarged the interlayer spacing. They also discovered that the CB and VB potentials of g-C_3N_4 could be modified by varying the potassium concentration, as shown in Figure-2.9 (c). When potassium concentrations are 0.05M and 0.07M, the band alignment is more appropriate to generate $OH^{\bullet}$ and $O_2^{\bullet}$ than other dopant concentrations, resulting in a considerably greater photodegradation rate (Shaozheng Hu et al., 2015). Using dicyandiamide and sodium hydrate as precursors, Zhang et al (Jian Zhang, Hu, & Wang, 2014). Synthesized a Na doped g-C_3N_4 photocatalyst with an adjustable bandgap. After sodium doping of the g-C_3N_4 photocatalyst, identical results were achieved in terms of band alignment with potassium doped (Jian Zhang et al., 2014). The CB and VB potentials of g-C_3N_4 could be tuned by controlling the sodium concentration. However, the RhB degradation rate of sodium doped was lower than potassium doped g-C_3N_4 under the same condition. This indicated that although the effects of potassium doping and sodium doping on g-C_3N_4 were similar, potassium doping was more suitable for enhancing photocatalytic activity (Shaozheng Hu et al., 2015; Jian Zhang et al., 2014).

Aside from alkali-metal doping, additional metal doping was researched. Indeed, g-C_3N_4 may easily trap metal cations due to the strong interactions between the cations and the negatively charged nitrogen atoms assigned to lone pairs of electrons in the nitrogen spots of g-C_3N_4 (SW Hu et al., 2015). Tonda et al (Tonda et al., 2014). Developed a simple and cost-effective method for producing iron-doped g-C_3N_4 nanosheets. They discovered that iron doping had a significant impact on the electronic and optical properties of g-C_3N_4 nanosheets, as increasing the iron content caused a red shift and increased absorption in the visible light range, as shown in Figure-2.9 (d). According to the XPS result Figure-2.9 (e), the iron species is in the 3^+ oxidation state, which can operate as a transient photogenerated electron and hole trapping site. These trapped electrons can decrease O_2 to $O_2^{\bullet}$. Meanwhile, valance holes can use Fe^{3+} as a mediator to oxidize OH or H_2O molecules to $OH^{\bullet}$. The photoluminescence in Figure-2.9 (f) indicates that the photoinduced charge carriers have a longer life span (Tonda et al., 2014). As a result, the photocatalytic activity for RhB degradation was greatly increased.

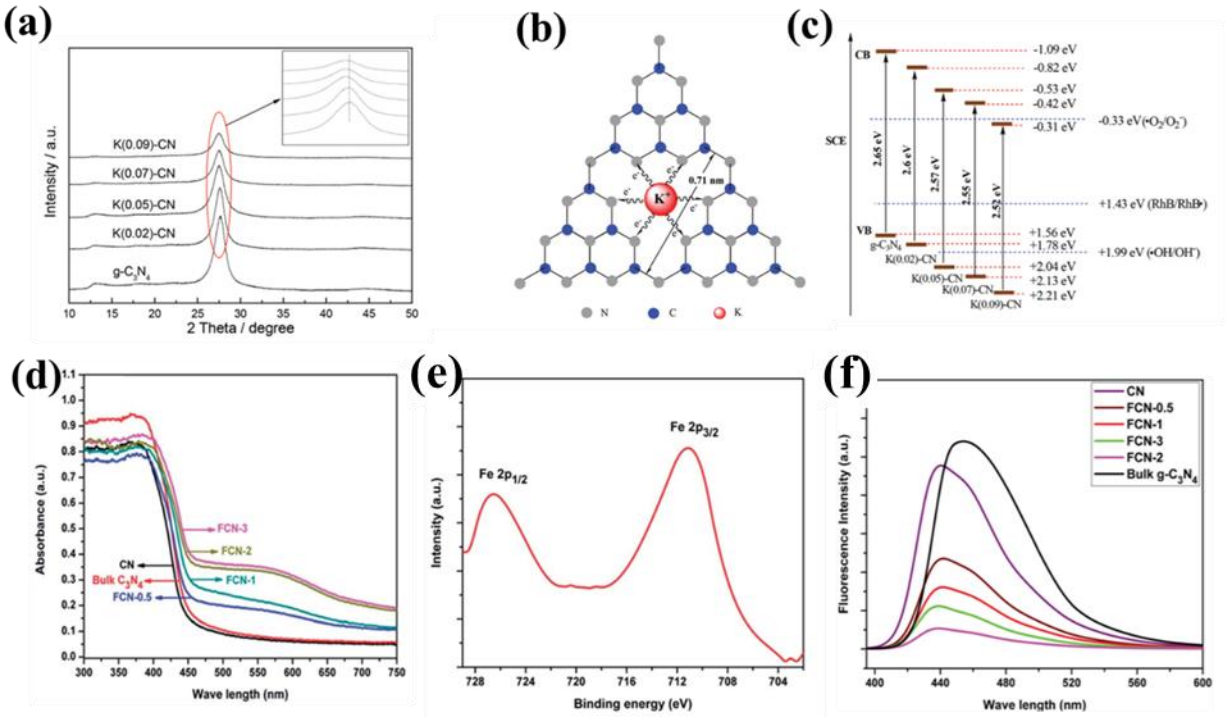

Figure-2.9 (a) XRD patterns of as-prepared g-C_3N_4 and potassium doped g-C_3N_4 (Shaozheng Hu et al., 2015). (b) Possible doping site for K ions in g-C_3N_4 (Shaozheng Hu et al., 2015). (c) Bandgap structures of as-prepared g-C_3N_4 and potassium doped g-C_3N_4 (Shaozheng Hu et al., 2015). (d) Optical absorption spectra of the synthesized bulk g-C_3N_4, and pure and Fe-doped g-C_3N_4 nanosheets(Tonda et al., 2014). (e)

XPS spectra of the synthesized Fe-doped g-C_3N_4 nanosheets of Fe 2p spectrum (Tonda et al., 2014). (f) room temperature photoluminescence (PL) spectra of the synthesized bulk g-C_3N_4, and pure and Fe-doped g-C_3N_4 nanosheets (Tonda et al., 2014).

A simple pyrolysis process employing common precursors was used to create molybdenum doped g-C_3N_4 catalysts (Yangang Wang, Xu, et al., 2016). They discovered that introducing molybdenum species may significantly lower the recombination rate of photogenerated charges, increase surface area, lengthen visible light sensitivity, and achieve a mesoporous structure with narrow bandgap energy. As a result, molybdenum doped g-C_3N_4 catalysts showed much greater CO_2 reduction activity. Yttrium, a rare earth element, was also utilized to dope on g-C_3N_4 for improved RhB degradation using a simple pyrolysis technique using urea as a precursor and yttrium nitrate as the yttrium source (Yangang Wang, Li, et al., 2016).

In general, the introduction of metal ions can result in the development of new energy levels in the band-gap, the extension of the visible light response, and the suppression of the electron-hole charge recombination rate. Despite numerous studies on alkali metal or transition metal-doped g-C_3N_4, some disadvantages of metal doping have been discovered. The thermal stability of doped ions, for example, is low. Furthermore, the newly formed energy bands may operate as recombination centers, resulting in lower quantum efficiencies (Li Zhou et al., 2016).

Non-metal doping has received a lot of attention to keep the metal-free property of g-C_3N_4. Furthermore, nonmetals have large ionization energies and electronegativity. As a result, nonmetals may often establish covalent bonds by acquiring electrons when interacting with other molecules (Li Zhou et al., 2016). Sulfur doping primarily replaces the nitrogen atom in the g-C_3N_4 matrix, giving it a significantly enhanced surface area and an effective reduction in bandgap energy due to the interaction of 3p sulfur states with 2p nitrogen levels. The reduction of bandgap energy enhances light absorption. The presence of an isolated atomic orbital of sulfur in the bandgap of g-C_3N_4 can affect the VB and CB potentials. Although numerous doping agents such as thiourea, H_2S, benzyl disulfide, tri-thiocyanic acid, thioacetamide, and others have been used in the case of sulfur doping. Thiourea has become more popular for in situ synthesis since it is conveniently accessible and affordable (Jourshabani et al., 2017; Starukh & Praus, 2020; K. Wang et al., 2015). Liu et al (G. Liu et al., 2010). Processed pure g-C_3N_4 powder in a gaseous H_2S environment at 450˚C to produce sulfur-doped g-C_3N_4. The S-doped g-C_3N_4 exhibits an enhanced VB width, an

elevated CB minimum, and a significantly lowered absorbance as shown in Figure-2.10 (a). This one-of-a-kind electronic structure, created by homogenous replacement of sulfur for lattice nitrogen and a concurrent quantum confinement effect, results in Sulfur-doped g-C_3N_4 with good photoreduction of H_2 evolution and photo-oxidation of phenol because of more negative conduction band (G. Liu et al., 2010). Hong et al (J. Hong, Xia, Wang, & Xu, 2012). Demonstrated the in-situ creation of Sulfur-doped mesoporous-g-C_3N_4 utilizing thiourea and SiO_2 nanoparticles through a simple calcination technique (J. Hong et al., 2012). SiO_2 nanoparticles with particle sizes ranging from 10 to 20 nm are employed as a hard template to raise the surface area to 128 m^2g^{-1}. The Mott-Schottky plot Figure-2.10 (b and c) was used to determine the n-type semiconducting nature and band potentials of Sulfur-doped mpg-C_3N_4. mpg-C_3N_4 and S doped mpg-C_3N_4 flat band potentials were determined to be -1.05 eV and -0,08 eV, respectively. A downward shift (0.25 eV) in CB potential was found from the bandgap and flat band potential. Although a slight decrease in CB potential reduces reduction ability, photocatalytic activity is caused by a reduced bandgap and increased light absorption. However, an increase in CB potential was recorded in ex-situ S-doped mpg-C_3N_4 due to a variation in S-doping location (J. Hong et al., 2012).

One challenge in photocatalysis is determining how to effectively adjust a photocatalysts bandgap. Reducing the bandgap allows for the harvesting of photons with lower energy or a longer wavelength, promoting the use of more solar energy. However, harvesting lower energy photons does not always imply improved photocatalytic performance, because photogenerated charges (i.e., electrons and holes) with a lower energy level, or lower oxidizing or reduction power, cannot effectively activate O_2/H_2O, and oxidize contaminants. A g-C_3N_4 sample with the lowest recorded band gap of 1.5 eV, for example, showed an 8.4-fold drop in reactivity for RhB degradation compared to another g-C_3N_4 sample with a bandgap of 2.1 eV, even though both samples were synthesized from triazole precursors (Dontsova et al., 2015). Figure-2.10 (d) compares the reduction potentials of a number of g-C_3N_4 samples and reference photocatalysts with known band gaps and band energy levels. Figure-2.10 (d) indicates that under thermodynamically favorable conditions, some g-C_3N_4 samples with a smaller bandgap cannot create ROS (i.e., O_2/HO_2) or oxidize impurities (Q. Zheng, Shen, & Shuai, 2017). Although these samples are susceptible to low-energy photons and create separated charges, the charges prefer to recombine rather than promote pollutant degradation and pathogen eradication.

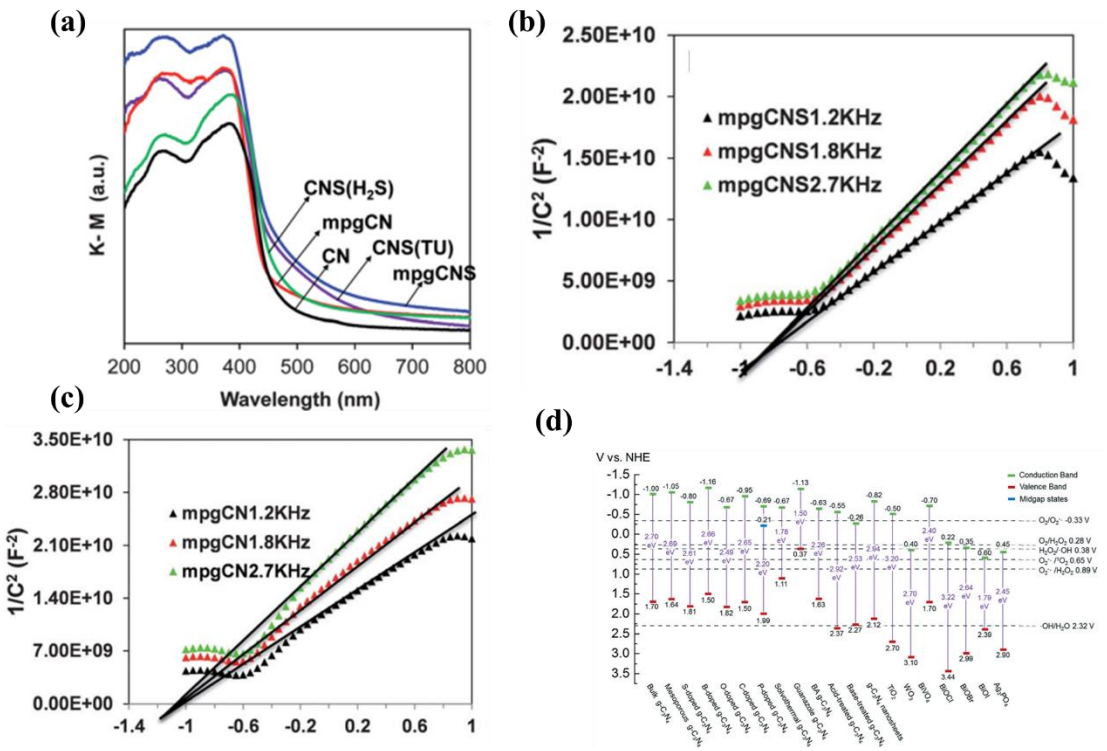

Figure-2.10 (a) UV–vis DRS spectra of mpgCNS and the control g-C_3N_4 samples (G. Liu et al., 2010). (b and c) Mott–Schottky plots of mpgCN and mpgCNS samples (G. Liu et al., 2010). (d) compares the reduction potentials of a number of g-C_3N_4 samples and reference photocatalysts (J. Hong et al., 2012).

2.4.3 g-C_3N_4 Composite

Some of the photogenerated electrons recombine with the holes rather than being employed in surface reactions to form the needed reactive species. The charge carriers compete to be recombined within a short period following generation. Figure-2.11 (a) summarizes the lifespan of photogenerated charges and active species produced (S. Das & Daud, 2014). Due to surface or bulk recombination, the absorbed energy is emitted in the form of heat or light, decreasing the photocatalytic efficiency. To enhance the separation efficiency of the electron-hole pairs, as well as the lifespan of the created reactive species, one of the best options is by coupling it with other semiconductors with matching band structures. Due to the flexibility and opened-up 2D morphology of g-C_3N_4 nanosheets are considered an ideal matrix for the construction of heterostructures with different components (Schneider et al., 2014).

The incorporation of two different semiconductors with separate bandgaps and electronic arrangements results in band bending at the interface known as the heterojunction (Vinodgopal &

Kamat, 1995). The heterojunctions are classified into three types based on the bandgap and the alignment of the VB and CB, i.e., type-I, type-II, and type-III. For the type-I category, also known as straddling band alignment as shown in Figure-2.11 (b), The band edges of semiconductor B with the smaller bandgap are contained within the VB and CB edges of semiconductor A with the greater bandgap. The effective separation of charge carriers is not visible, and the redox ability is much reduced in the case of the type-I heterojunction, since following light irradiation, both photogenerated charge carriers aggregate across the VB and CB of semiconductor B (Yuzhen Li, Wang, Huo, Li, & Shi, 2020; Y. Zhu, Wan, Wen, Chu, & Jiang, 2019).

The most frequent kind of charge transfer is the type-II heterojunction (staggered type), as seen in Figure-2.11 (c), in which the VB and CB of semiconductor A are located above the respective energy levels of semiconductor B. As a consequence, when exposed to light, photogenerated electrons rush to the CB of semiconductor B, while holes migrate to the VB of semiconductor A, assuring spatial electron and hole separation (Acharya, Nayak, Pattnaik, Acharya, & Parida, 2020; C. He, Zhang, Zhang, & Li, 2019; Sahoo, Das, Patnaik, & Parida, 2020).

The third kind, known as the broken type or type-III, is designed such that the bandgaps of both semiconductors do not overlap, i.e., both the VB and CB of semiconductor B remain above the CB band of semiconductor A (Figure-2.11 (d)). Because of the above-mentioned band structure, there is no charge carrier movement and hence no spatial separation, making it unsuitable for charge separation.

Among the mentioned heterojunctions, type-II, i.e., the staggered type, is the most useful heterostructure and is widely used in the field of photocatalysis because the significant enhancement of spatial electron-hole separation has been observed, resulting in slower recombination rates and thus prolonging the lifetime of respective charge carriers, allowing the oxidation/reduction reactions to proceed in distinct semiconductors (Cai et al., 2019). However, the type-II heterostructure has numerous limitations that hinder its widespread applicability in photocatalysis. Given the electrostatic force of repulsion, it is difficult for electrons to migrate to the CB with higher electron density and holes to migrate to the VB with higher hole density. As electrons migrate to the CB of semiconductor B with lower reduction potential and holes gather on the VB of semiconductor A with lower oxidation potential, the oxidation and reduction abilities of the migrating holes and electrons decline. To address the aforementioned issues, it is critical to

build a novel photocatalytic system. Recently, Z-scheme photocatalysts have gained popularity because they not only prevent recombination of photogenerated electron-hole pairs but also preserve significant redox activity as illustrated in Figure-2.11 (e) (Yan Wu et al., 2018; Zhou, Yu, & Jaroniec, 2014).

The Z scheme concept is derived from imitating the natural photosynthesis process that occurs in the chlorophyll of green plants to enable the thermodynamically uphill conversion of H_2O and CO_2 by gathering energy from solar light. O_2 and carbohydrates are generated throughout the process from H_2O and CO_2 via a two-step photo-excitation process, as shown in Figure-2.11 (f). Photosystems I (PS I) and II (PS II) capture photons at 700 and 680 nm and excite electrons to a higher electronic state. The electrons in PS II were then transferred to PS I through the electron transfer chain (electron mediator). Furthermore, the electrons of PS I have activated once again, resulting in the reduction of co-enzyme $NADP^+$ into NADP, which is employed to convert CO_2 into carbohydrate. A water oxidation process happens at the manganese calcium oxide cluster on the donor side of PS II (Tachibana, Vayssieres, & Durrant, 2012; Umena, Kawakami, Shen, & Kamiya, 2011). In plants, the two processes occur concurrently in time but independently in space. Photoexcited electrons in PS II can move to PS I through an electron mediator in an artificial Z-scheme system. As a result, the photogenerated electrons of PS I and the left holes of PS II have a high redox ability. Artificial Z-scheme systems have been widely employed in water splitting, CO_2 reduction, pollutant degradation, and other applications due to their unique advantages in redox ability and charge separation efficiency.

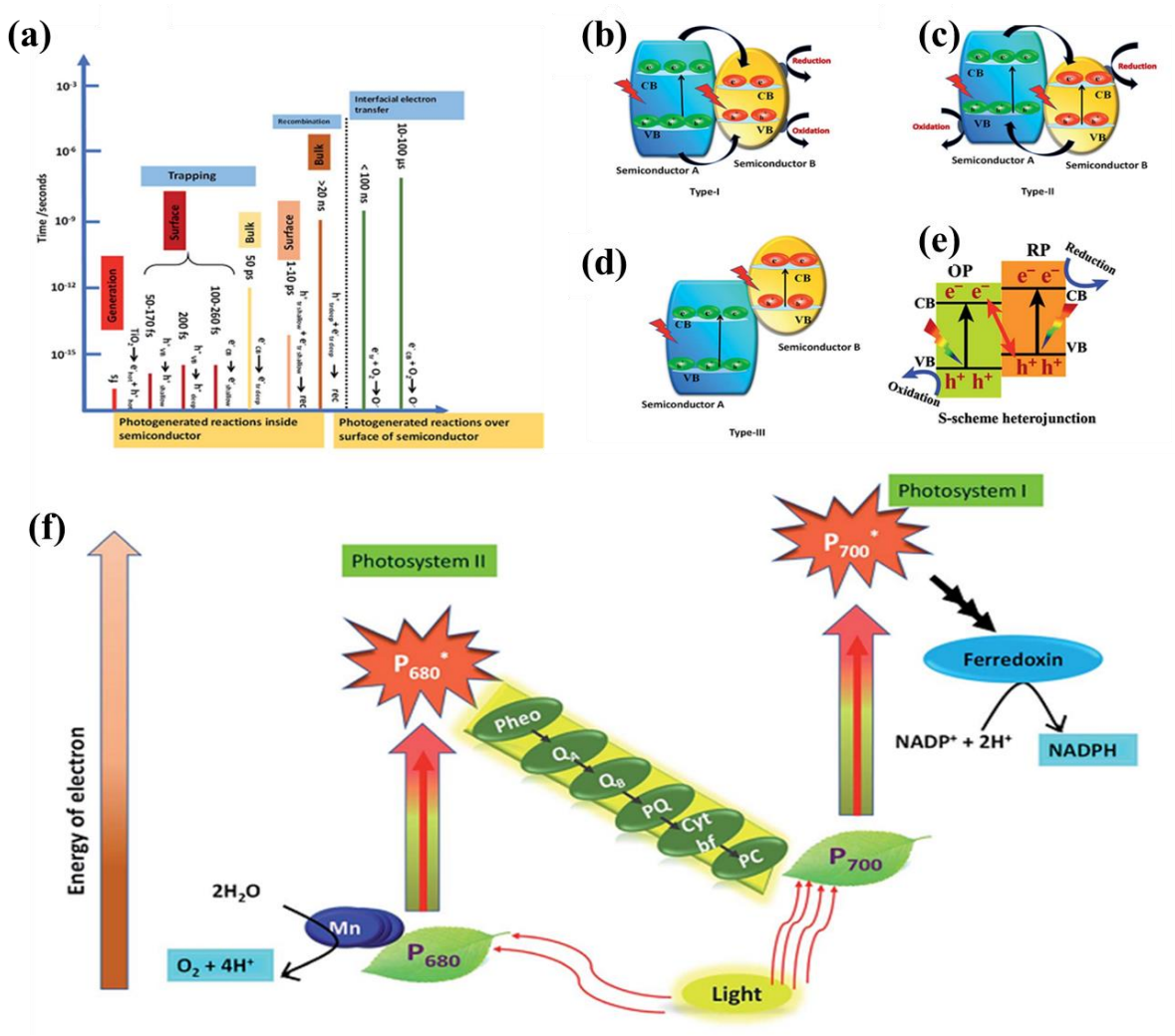

Figure-2.11 (a) lifespan of photogenerated charges and active species over a TiO_2 semiconductor (B. P. Mishra & Parida, 2021). (b) Schematic illustration of (b) type-I; (c) type-II; (d) type-III; and (e) z scheme heterojunctions (Q. Xu, Zhang, Cheng, Fan, & Yu, 2020).(f) Schematic illustration of natural photosynthesis (B. P. Mishra & Parida, 2021).

Chunyan Du et al (Du et al., 2021). Investigated Z-scheme g-C_3N_4 / MnO_2 /GO ternary heterostructure for the degradation of Tetracycline Hydrochloride (TC-HCl) under visible light illumination. This heterostructure demonstrated higher catalytic activity than the bulk g-C_3N_4 for MnO_2 content of 20% and GO content of 10%. The improved photoactivity was ascribed to the close physical contact between the g-C_3N_4, MnO_2, and GO that occurs as a result of the homogenous distribution of the microspheres across the g-C_3N_4 fakes, which is known to lengthen the light absorption edge. Furthermore, the electrochemical impedance spectra,

photoluminescence, and permanent photo-current responses illustrated in Figure-2.12 (a, b, and c) indicate that photoinduced charge carriers have a longer lifetime. Following that, the active radical trapping experiment confirmed the Z scheme charge transfer mechanism as illustrated in Figure-2.12 (d), which demonstrated electron-hole separation and produced a contact surface that acted as a charge facilitation bridge, hence improving photocatalytic performance. The catalyst demonstrated outstanding photostability and usability for up to four cycles, making it a viable choice for photodegradation applications (Du et al., 2021).

The Z-scheme Ag@AgBr/g-C_3N_4 plasmonic photocatalyst retained photoinduced electrons and holes with strong reduction and oxidation power in the CB of g-C_3N_4 and VB of AgBr, respectively, achieving high efficient MB photodegradation. The produced Br^0 atoms and superoxide radicals with high oxidizing capacities during photocatalysis are advantageous for further enhancing the degradation process (Y. Yang et al., 2014).

Wu et al (Yuhang Wu, Song, Chai, Huang, & Wang, 2020). Designed a metallic mediator-based Z scheme system, Bi_2MoO_6/Bi/g-C_3N_4, to study the photooxidation of formaldehyde under visible light irradiation. The Z scheme composite demonstrated improved gaseous Formaldehyde (HCHO) degradation and might be used for C_6H_6 and CH_3-$COOCH_2CH_3$ purification. Because of the dispersion of small Bi_2MoO_6 particles, the composite had a higher surface area (61.28 m^2 g^{-1}) and hence improved adsorption capabilities illustrated in Figure-2.12 (e). The DFT analysis supported the stronger adsorption properties. To study the charge separation efficiency, the fluorescence decay and photoluminescence spectra (Figure-2.12 (f and g)) were analyzed which shows effective charge separation and increment in the lied span of charge carries for the composite. The KubelkaMunk function confirmed that the charge transfer mechanism is of the Z scheme type. The hypothesized process is depicted in Figure-2.12 (h), in which Bi NPs are deposited at the junction of Bi_2MoO_6 and g-C_3N_4, facilitating electron flow and successfully segregating charge carriers while preserving strong redox capacity (Yuhang Wu et al., 2020).

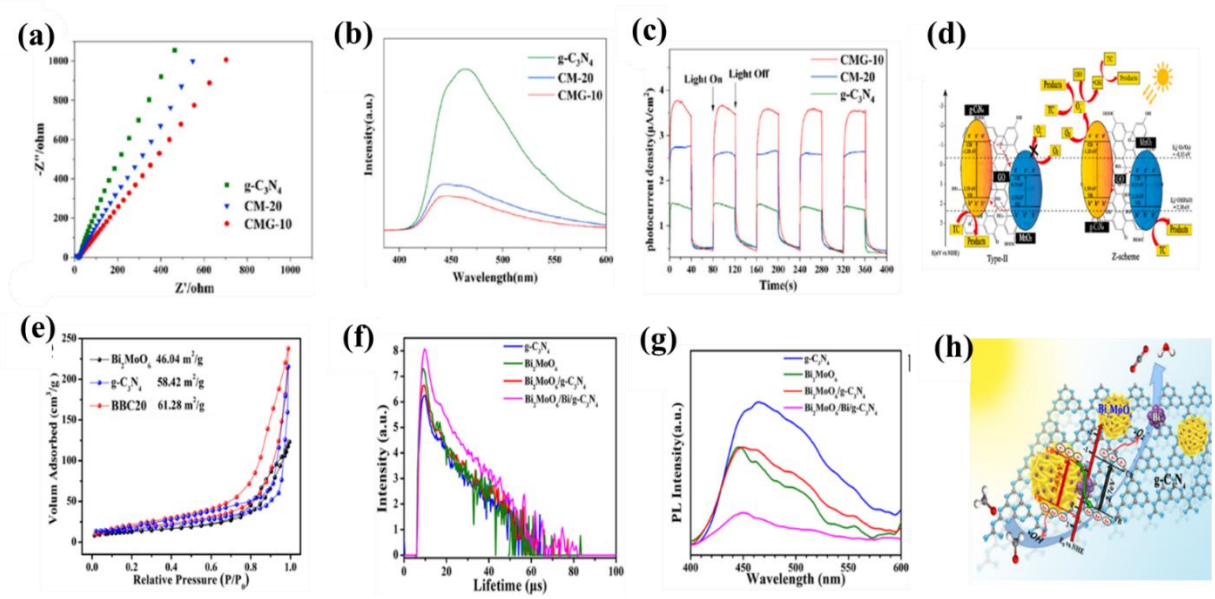

Figure-2.12 (a) the EIS (b) PL spectra (c) Transient photocurrent responses of g-C_3N_4, CM-20 and CMG-10 (Du et al., 2021). (d) Photocatalytic mechanism scheme of CMG-10 composites (Du et al., 2021). (e) Nitrogen adsorption-desorption isotherms (f) PL spectra (g) fluorescence decay spectra of g-C_3N_4, Bi_2MoO_6 and BBC20 (Yuhang Wu et al., 2020).(h) Schematic diagram of photocatalytic oxidation of HCHO in Bi_2MoO_6/Bi/g-C_3N_4 under visible light (Yuhang Wu et al., 2020).

Jung et al (Jung, Pham, & Shin, 2018). Synthesized g-C_3N_4-ZnO at different thermal treatment and condensation temperatures (T = 350, 400, 450, and 500°C). By raising the thermal treatment temperature, the BET specific area and ZnO crystallite size of the produced Z-scheme g-C_3N_4-ZnO structure are reduced (Jung et al., 2018). Other researchers that used thermal treatment to create g-C_3N_4-ZnO stated that the optimal quantity of g-C_3N_4 content in the composite is 5.0 wt.% (W. Liu, Wang, Xu, & Chen, 2012)

Yi and colleagues effectively manufactured the 2D/3D g-C_3N_4/UiO-66 Z scheme nanocomposite and investigated its photocatalytic activity in the reduction of chromium (Cr (VI)) under visible light irradiation. The PL spectra of $BG_{60}U_{40}$ (Figure-2.13 (a)) revealed an emission peak at 440 nm, confirming that the lifetime of photoexcited charge carriers was increased. The EIS investigation presented in Figure-2.13 (b) clarified the composite's increased charge separation efficiency as well as interfacial charge transfer. The Cr (VI) reduction abilities at different pH levels were studied, and the degradation rate constant was greatest at pH 2 (Figure-2.13 (c)) (Yi et al., 2019).

Wang et al (C.-H. Wang et al., 2017). Changed the deposition sequence of WO_3 and g-C_3N_4 to generate two distinct types of charge transfer routes type II and Z-scheme heterojunction film has been effectively constructed on the transparent conducting substrate for photoelectrochemical oxidation of water as illustrated in Figure-2.13 (e). The PL spectra (Figure-2.13 (f and g)) demonstrated charge separation of carries, although both forms of junction demonstrated effective charge separation, the z-scheme demonstrated more separation of charge carriers, which was also demonstrated in the EIS investigation (Figure-2.13 h and i). Although greater photocurrents were reported for type (II) charge transfer, the photocurrent enhancement factor for the Z-scheme-based photoelectrode proved to be superior (Figure-2.13 (j and k)) (C.-H. Wang et al., 2017).

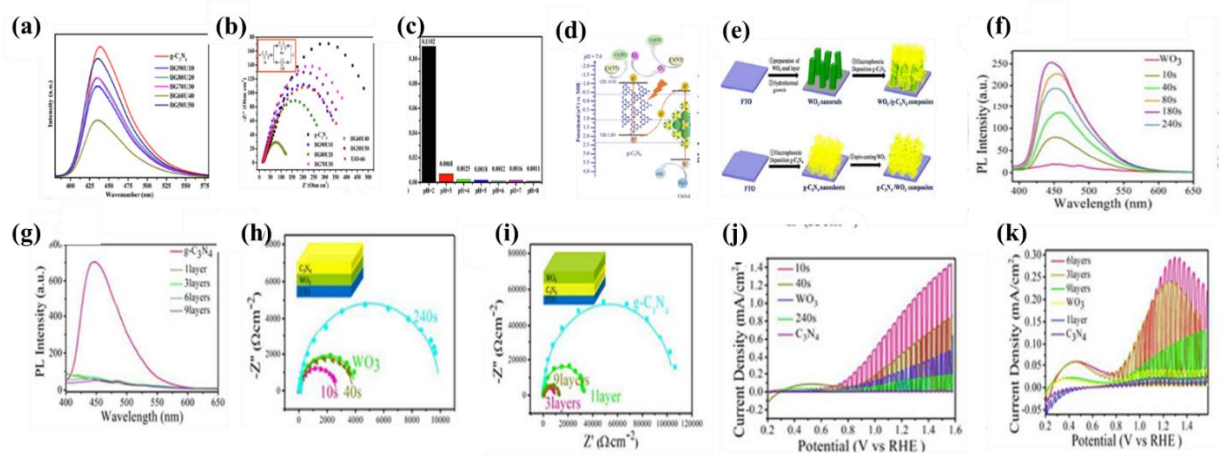

Figure-2.13 (a) The PL spectra (b) EIS analysis of the samples (c) The k values over the different initial pH photocatalysts (Yi et al., 2019). (e and f) Schematic diagrams for the preparation of type II WO_3/g-C_3N_4 and Z-scheme g-C_3N_4/WO_3 heterojunction photoanodes (C.-H. Wang et al., 2017). (h and I) are PL spectra of the samples (C.-H. Wang et al., 2017). (j and k) Photocurrent response i-t curve (C.-H. Wang et al., 2017).

Important publications over the years regarding g-C_3N_4-based photocatalysts have been summarized in Table 1 based on a modification of graphitic carbon nitride for the degradation of pollutants. Even though various studies have concentrated on the sensitization and decorating of semiconductors with g-C_3N_4, research on the application of g-C_3N_4 as a host, which commonly forms the Z-scheme, is still in its early phases and hence needs more attention. Because of its extremely negative conduction band, g-C_3N_4 has a higher redox potential in Z-scheme configurations than type (II), which is critical for wastewater treatment. In this present work, the ternary photocatalyst of the g-C_3N_4-ZnO-Co_3O_4 composite was prepared through a simple wet

impregnation process to improve not only visible light absorption but also electron-hole pair separation and active surface area. Few studies have combined all of the aforementioned strategies to improve the photocatalytic properties of g-C_3N_4. For the synthesis of metal oxide, we have used cellulose from "enset" fiber as a template since hydroxyl group on cellulose act as efficient hydrophilic substrates for the nucleation and growth of metal oxide, giving high specific surface area and pore size distribution. A variety of analytical techniques were used to evaluate the synthesized samples. Their catalytic activities were evaluated by the degradation of methylene blue (MB), under visible light irradiation.

Table-2.1 g-C_3N_4-based photocatalysts for pollutant degradation.

No.	Photocatlys	Synthesis method	Light source	Target pollutant	Degradation time	Efficiency (%)	Ref.
Surface Modification							
1	g-C_3N_4	Plasma Treatment	-	RhB	60 min	60	(Ji et al., 2017)
2	g-C_3N_4	Chemical exfoliation	-	RhB	120 min	60	(T. Huang et al., 2022)
3	g-C_3N_4	Thermal exfoliation	-	RhB	60 min	86	(Rono, Kibet, Martincigh, & Nyamori, 2021)
4	g-C_3N_4	Soft template	350 W tungsten lamp	MB	120 min	52.3	(Y. Li et al., 2019)
5	g-C_3N_4	Soft template	120-W metal vapor lamp	RhB	60 min	93	(de Lima et al., 2020)
Doping							
6	Y/g-C_3N_4	Thermal polymerization	500W xenon lamp	RhB	110 min	100	(Yanagang Wang, Li, et al., 2016)

7	Zr/g-C_3N_4	Thermal polymerization	500W xenon lamp	RhB	110 min	100	(Y. Wang et al., 2015)
8	Cu/g-C_3N_4	Thermal polymerization	350 W tungsten lamp	MO	120 min	90.2	(Le et al., 2016)
9	Ce/g-C_3N_4	Thermal polymerization	250W sodium lamp	RhB	120 min	90	(R. Jin, Hu, Gui, & Liu, 2015)
10	Co/g-C_3N_4	Thermal polymerization	-	RhB	135 min	90	(D. Das, Banerjee, Das, Das, & Chattopadhyay, 2017)
11	B and P/g-C_3N_4	hydrothermal	8 × 8 W visible lamps	diclofenac	90 min	95	(Ganganboina, Nguyen, Nguyen, Kuncoro, & Doong, 2021)
12	O/g-C_3N_4	hydrothermal	-	MB	3 hr	81	(Jianghua Li et al., 2012)
13	Mn/g-C_3N_4	Thermal polymerization	300W xenon lamp	MB	3 hr	96.1	(J.-C. Wang et al., 2018)
14	Fe/g-C_3N_4	Thermal polymerization	sunlight irradiation	RhB	30 min	99	(Tonda et al., 2014)
15	C/g-C_3N_4	Thermal polymerization	sunlight irradiation	Tetracycline	90 min	95	(Panneri et al., 2017)

16	Ag/g-C_3N_4	-	300W xenon lamp	MB	240 min	100	(X. Liu, Tang, Xia, Qin, & Zhang, 2020)
17	P and O/g-C_3N_4	Thermal polymerization	350W xenon lamp	fluoroquinolone	80 min	6.2 times higher	(J. Huang et al., 2019)
18	Zn/g-C_3N_4	Thermal polymerization	300W xenon lamp	MO	240 min	95	(Z.-T. Wang, Xu, Zhou, & Zhang, 2019)
Composites							
19	g-C_3N_4/MnO_2	Wet-chemical method	300W xenon lamp	**RhB**	60 min	91.3	(Xia, Zhu, Cheng, Yu, & Xu, 2018)
20	gC_3N_4/Bi_2WO_6	Refux method	300W xenon lamp	Tetracycline	60 min	87	(M. Zhang et al., 2019)
21	g-C_3N_4/Ag_2WO_4	Precipitation method	300W xenon lamp	MO	150 min	95	(B. Zhu, Xia, Li, Ho, & Yu, 2017)
22	g-C_3N_4/UiO-66	Ball milling method	300W xenon lamp	Cr(VI) reduction	40 min	99	(Yi et al., 2019)
23	g-C_3N_4/ZnO	Thermal atomic layer deposition reactor	300W xenon lamp	Cephalexin	60 min	98.9	(N. Li et al., 2018)
24	g-C_3N_4/TiO_2	Wetness impregnation	-	Isoniazid	-	79.5	(Jo & Natarajan, 2015)

25	$CdS/Ag/g\text{-}C_3N_4$	Hydrothermal	250W xenon lamp	RhB and TC	90 min	81.9and 86.4	(Qin et al., 2018)
26	$Ag_2CrO_4/Ag/g\text{-}C_3N_4$	Photoreduction	500W xenon lamp	2,4-DCP	90 min	62	(Gong, Quan, Yu, & Chen, 2017)
27	$g\text{-}C_3N_4/SiO_2$	Thermal polymerization	300W xenon lamp	RhB	150 min	94.3	(Lin et al., 2015)
28	g-C3N4/Ag2O	precipitation method	300W xenon lamp	MO, phenol and RhB	30,180 and 40 min	90,82 and 100	(M. Xu, Han, & Dong, 2013)
29	$g\text{-}C_3N_4/SiO_2$	Thermal polymerization	300W xenon lamp	RhB	150 min	94.3	(Peng, Zheng, Feng, Yu, & Dong, 2020)
30	$g\text{-}C_3N_4/\ Co_3O_4\text{-}V_2O_5$	wet impregnation	500W halogen lamp	MB + MY	80 min	93.8	(Palanisamy et al., 2021)
31	$g\text{-}C_3N_4/Fe_3O_4/Ag_3VO_4$	ultrasonic irradiation	50 W LED	RhB	240 min	98	(Mousavi & Habibi-Yangjeh, 2015)
32	$g\text{-}C_3N_4/WO_3$	Solid state method	300W xenon lamp	MB	90 min	95	(X. Liu et al., 2017)
33	$g\text{-}C_3N_4/SnS$	chemical deposition	150W xenon lamp	RhB	60 min	62	(Jia et al., 2020)
34	$WO_3/g\text{-}C_3N_4/Bi_2O_3$	Solid state synthesis	300W xenon lamp	Tetracycline	120 min	69.3	(Jiang et al., 2018)
35	$MIL53(Fe)/Ag/g\ C_3N_4$	Ultrasonic	100 W CFL lamp	clioquinol	100 min	95	(Patra, Rahut, & Basu, 2018)

36	CdS/CQDs/g-C_3N_4	Thermal polymerization	300W xenon lamp	RhB,MB and phenol	20, 120, and 120 min	100, 98, and 58	(Feng et al., 2020)
37	g-C_3N_4/ Co_3O_4/Zno	wet impregnation	250 w halogen lamp	MB	60 min	97.4	Present work

CHAPTER THREE

3 Methodology and Material

3.1 Chemicals

Enset fiber was purchased from a local market in Hawass, South Ethiopia, Glacial acetic acid (Riedel-de Haën), sodium hydroxide 97% (HiMedia, Mumbai, India), and formic acid (98%) (Central Drug House (P) Ltd. New Delhi, India), hydrogen peroxide 30% (CARLO ERBA Reagents, France), Urea (CH_4N_2O), sulfuric acid (H_2SO_4), cobalt (II) nitrate hexahydrate (($Co(NO_3)_2 \cdot 6 H_2O$), Zinc nitrate hexahydrate $Zn(NO_3)_2 \cdot 6H_2O$ were purchased from Merck and Loba company. Methylene blue ($C16H_{18}N_3SCl$) dye is purchased from Sigma Aldrich, All the compounds were used exactly as established without additional refinement.

3.2 Samples Synthesis

3.2.1 Synthesis of Cellulose

The synthesis of cellulose was carried out with a little modification (Figure-3.1) (Gabriel, Belete, Syrowatka, Neubert, & Gebre-Mariam, 2020). The plant by-products were cleaned and dried in an oven at 80°C. To eliminate reaming dust, the raw material is boiled with a 2% NaOH (1:40) W/V ratio for 2 hours, then dried in an oven at 70°C and diced. The second Alkaline pretreatment was carried out on a hot plate at 90°C for 1.5 hours in 10% NaOH solutions with a solid to liquid ratio of 1:10 (w/v) of dry material. Byproduct residues were regularly filtered and washed with hot distilled water. The pulps were then treated for 1.5 hours on a hotplate at 90°C with a solution of 20% formic acid /20% acetic acid /7.5% H_2O_2 (2:1:2) at a byproduct to liquor ratio of 1:10 (w/v). To separate the cooking liquid (which contains lignin and hemicellulose) from the cellulose, the delignified pulps were filtered and washed with hot water.

Bleaching was performed by treating the pulps with 7.5% H_2O_2 in an alkaline medium of 10% NaOH solutions at a ratio of 1:10 (w/v) for 30 minutes at 70°C the pulps were washed many times with hot distilled water to remove residual lignin before being dried in an oven at 60°C until a consistent weight was produced. The bleaching process was carried out twice. Finally, 5 g cellulose was added to a 250 ml 50% H_2SO_4 aqueous solution for 30 minutes at 60°C before being diluted with distilled water. The acid-assisted precipitate was centrifuged and washed with distilled water

until the ph was neutral, after which the cellulose gel was ultrasonically dispersed in 1 liter of distilled water and stored for further use.

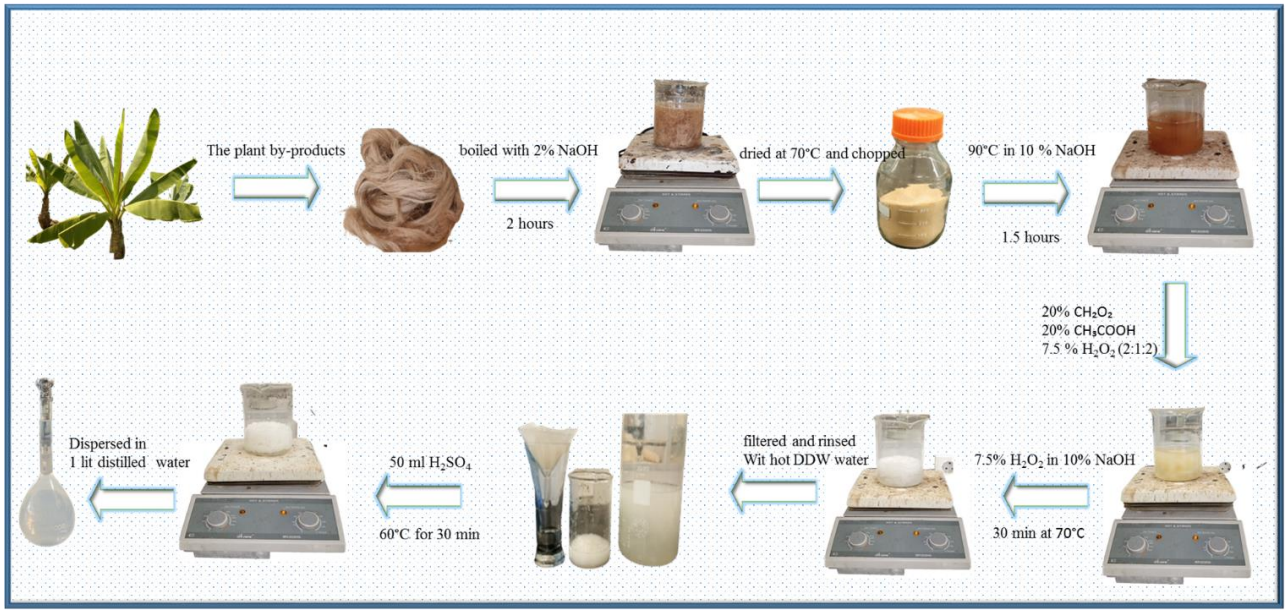

Figure-3.1 Schematic illustration of the celluloses Synthesis process.

3.2.2 Synthesis of ZnO

The simple chemical precipitation process was used to create ZnO (Figure-3.2) (Goswami, Adhikary, & Bhattacharjee, 2018). In a nutshell, 0.1 M of Zn $(NO_3)_2$•$6H_2O$ was dissolved in 200 ml of dispersed cellulose solution under vigorous stirring. The prepared solution was stirred for 30 minutes to ensure adequate dissolution. The pH of the prepared solution was raised to 10 for precipitation by adding 1 M NaOH dropwise with continuous stirring. The addition of NaOH was halted after pH 10 was reached. Then the solution was stirred for 2hr at 60°c. Later, the solution was aged for 24hr. The precipitate was centrifuged and washed with distilled water followed by ethanol. After washing, the precipitate was recovered and dried in an oven at 100°C for 2 hours. The dried sample was then calcined in a muffle furnace at 500°C for 2 hours. After being ground to a powder, the calcined ZnO was recovered from the furnace and used in future studies.

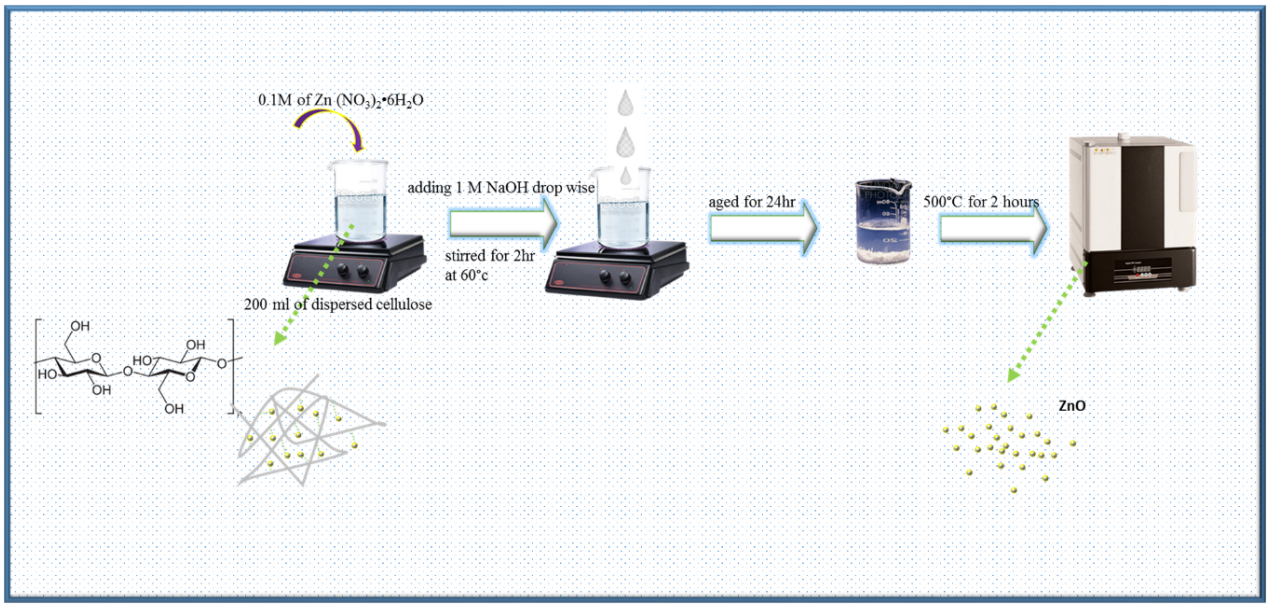

Figure-3.2 Schematic illustration of ZnO Synthesis process.

3.2.3 Synthesis of Co_3O_4

Co_3O_4 was synthesized using the simple chemical precipitation method (Figure-3.3) (Dubey, Kumar, Kumar, & Sharma, 2018). Briefly, 0.1 M of Co $(NO_3)_2 \cdot 6H_2O$ was dissolved in 200 ml of dispersed cellulose solution under vigorous stirring. The prepared solution was stirred for 30 minutes to ensure adequate dissolution. The pH of the prepared solution was raised to 10 for precipitation by adding 1 M NaOH dropwise with continuous stirring. The addition of NaOH was halted after pH 10 was reached. Then the solution was stirred for 2hr at 60°c. Later, the solution was aged for 24hr. The precipitate was centrifuged and washed with distilled water followed by ethanol. After washing, the precipitate was recovered and dried in an oven at 100°C for 2 hours. The dried sample was then calcined in a muffle furnace at 400°c for 2 hours. After being ground to a powder, the calcined Co_3O_4 was recovered from the furnace and used in future studies.

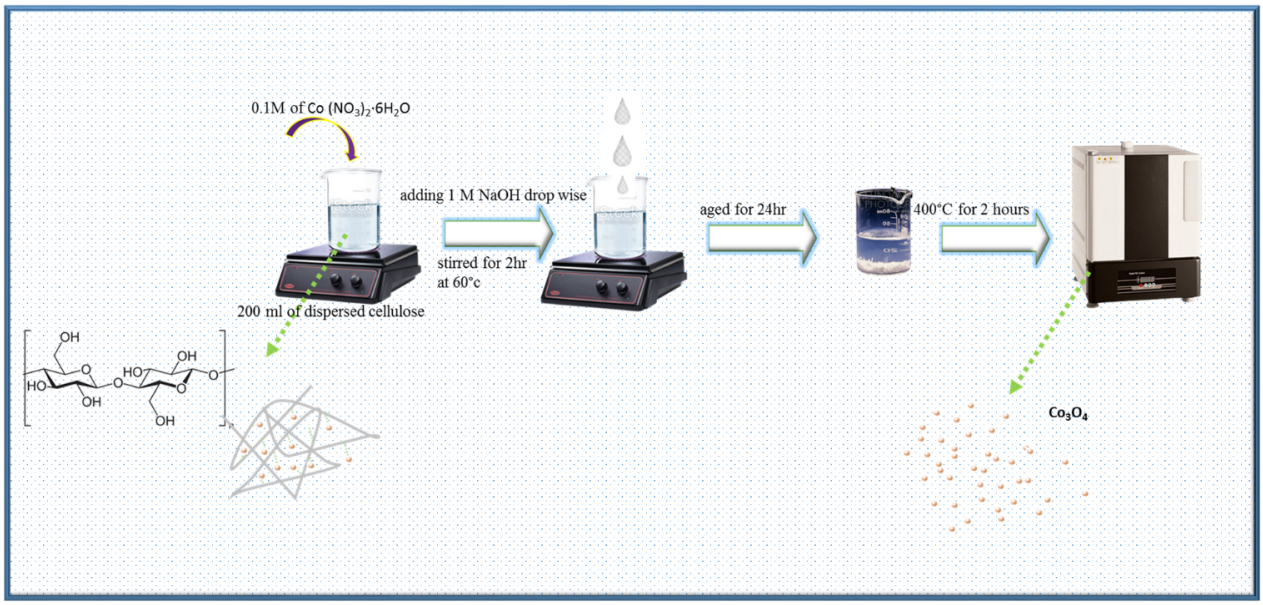

Figure-3.3 Schematic illustrations of the Co_3O_4 Synthesis process.

3.2.4 Synthesis of g-C_3N_4

The g-C_3N_4 was synthesized using a simple thermal pyrolysis process (Figure-3.4) (Palanisamy et al., 2021). 10 g of urea powder was added into a Crucible covered with a lid and heated at 2°C min^{-1} up to 550 °C in a muffle furnace for 4h. After allowing cool to room temperature, the resultant pale yellow sponge-like product was collected and ground into powder in a mortar. 500 mg of as-synthesized powder was dispersed in 30 ml H_2SO_4 and stirred for 24hr at room temperature to weaken the bonds between the interlayers. This solution was diluted using 200 ml double distilled water (DDW) and ultra-sonicated for 8 h to exfoliate the gC_3N_4 layers. The suspension was separated from the residual solution and washed with DDW and ethanol several times to remove any residual acid. Finally, the mixture was dried at 80 °C to obtain g-C_3N_4.

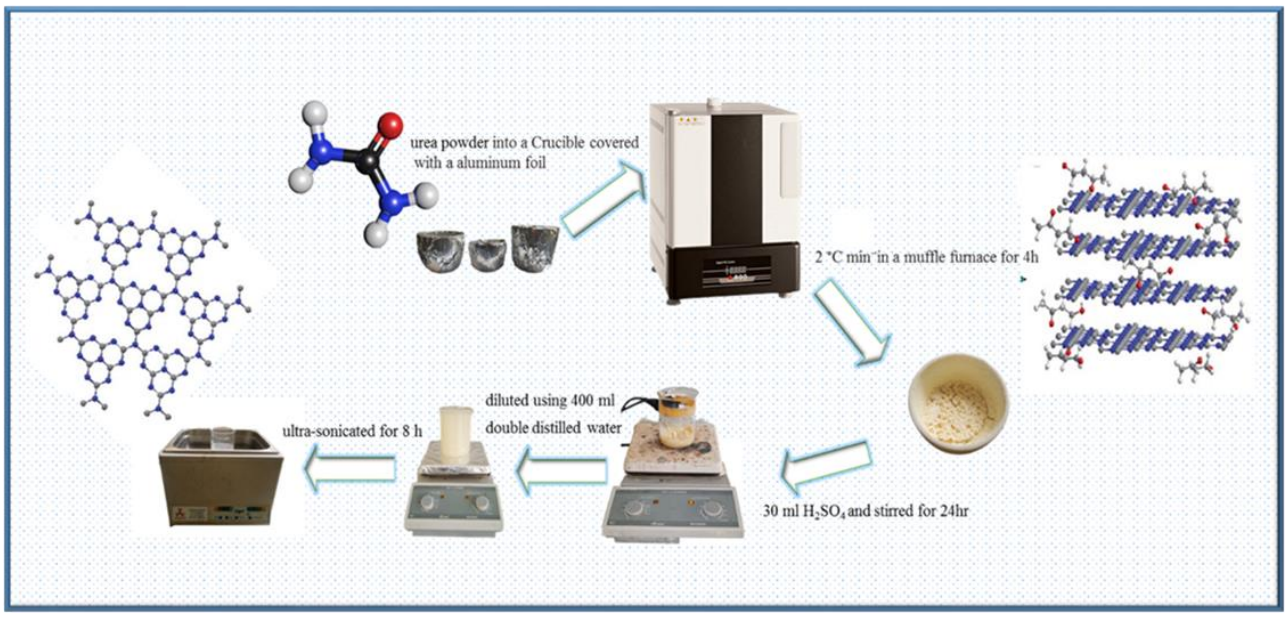

Figure-3.4 Schematic illustration of the g-C_3N_4 Synthesis process.

3.2.5 Synthesis of g-C_3N_4/ZnO/Co_3O_4 Composite

A wet impregnation process was used to make the g-C_3N_4/ZnO/Co_3O_4 composite (Figure-3.5). Typically, the different weight ratios of Co_3O_4 and ZnO samples were added to g-C_3N_4 in 30 ml of ethanol solution, namely 10% (GZC-1), 20% (GZC-2), 30% (GZC-3), 40% (GZC-4), and 50% (GZC-5)). The mixed solution was ultrasonically treated for 30 min and stirred for 2 hr. The obtained solid was then dried for 6 h at 70˚C, a similar method was used to prepare the g-C_3N_4-Co_3O_4 composite and g-C_3N_4-ZnO.

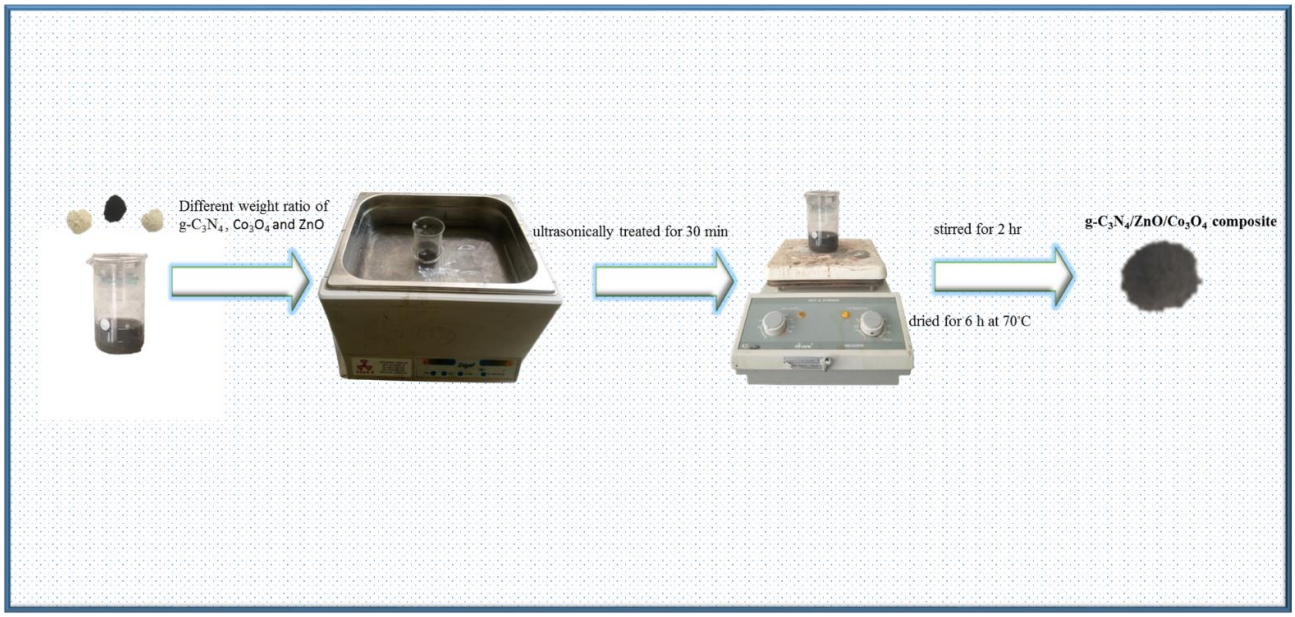

Figure-3.5 schematic illustration of g-C_3N_4/ZnO/Co_3O_4 composite Synthesis process.

3.3 Characterization

The phase and crystallinity of samples were determined by x-ray diffraction (XRD) (ShimadzuXRD-7000) with CuK α radiation. Fourier transform infrared (FTIR) analysis was done by using Spectrum 65 FT-IR (Perk in Elmer) in the range 4000–400cm−1 using KBrpellets. The optical absorption spectra were measured using Shimadzu 3600 UV–Vis-NIR spectrophotometer in the wavelength range of 200–800 nm using $BaSO_4$ as a reference. Brunauer, Emmett, and Teller (BET) specific surface area measurements were recorded by N_2 adsorption using an ASAP 2020 HD88 surface area analyzer. Photoluminescence spectra of the prepared samples were recorded using a fluorescence spectrophotometer (PE-LS55, USA) fitted with a xenon lamp at an exciton wavelength of 326 nm. Electrochemical impedance spectroscopy (EIS) and Mott-Schottky plot were measured using a three-electrode system with an Autolab PGSTAT 302 N electrochemical test system (Metrohm Autolab B.V.) where Pt wire and Ag/AgCl electrode were used as the counter and reference electrodes, respectively.

3.4 Photocatalytic Performance

To study the photocatalytic performance of all samples, a vertical photoreactor was set up with a 250 W halogen lamp as the light source. Typically, around 30 mg of photocatalyst sample was dispersed in a 100 ml (10ppm) aqueous suspension of MB. To achieve adsorption-desorption equilibrium between the photocatalyst and dye, the suspension was kept under constant stirring for

30 min before the photocatalytic degradation test. After each successive light irradiation interval, 4 ml of suspension was drawn and centrifuged to separate supernatant from photocatalyst powder. UV-Vis spectrophotometer was used to measure the intensity of the MB absorption band at 547 nm to determine the concentration of dye in the residual solution. We kept the distance between the surface of the suspension solution and the light source constant throughout the experiment at 5 cm. The degradation efficiency (η) of the MB dye was calculated as follows:

$$\eta = \left(Co - \frac{Ct}{Co}\right) \times 100\% \ldots\ldots\ldots\ldots\ldots\ldots\ldots\ldots\ldots\ldots\ldots\ldots\ldots\ldots eqution\ (1)$$

Where C_0 and C_t are the concentrations of the MB dye at the initial and specified irradiation times, respectively. All the tests were repeated twice to confirm the result.

CHAPTER FOUR

4.1 Results and Discussion

4.1.1 X-ray Diffraction Analysis

The phase purity and crystal structure were examined using XRD. Figures-3.6 (a-c) depict experimental data for cellulose, g-C_3N_4, Co_3O_4, ZnO, g-C_3N_4/Co_3O_4, g-C_3N_4/ZnO, and g-C_3N_4/ZnO/Co_3O_4 composite analyzed by XRD. Cellulose is classified into four categories (I, I, II, III, and IV cellulose) based on the material from which it is extracted and the chemicals employed in the treatment process (Seddiqi et al., 2021). Figure-4.1 (a) shows that the XRD patterns revealed peaks at 16°, 22°, and 34° at (2θ) with the assigned crystallographic planes of (110), (200), and (400), respectively, indicating Cellulose I, as well as no doublet in the intensity of the main peak, indicating no morphological change due to chemical treatment, and the absence of doublet indicating the absence of cellulose II (Morán, Alvarez, Cyras, & Vázquez, 2008).

Figure-4.1 (b) shows two distinct peaks for pure g-C_3N_4, one with a strong signal at 27.5° and the other with a faint signal at 13.2°, which correspond to the (002) and (100) planes of g-C_3N_4 (JCPDS-87-1526) (Peng et al., 2020). These corresponding crystal planes are attributed to tri-s-triazine units and aromatic interlayer stacking, respectively (Morán et al., 2008). The peak intensity of plane (002) is very weak, suggesting a decrease in the number of layers in the stacking due to exfoliation using sulfuric acid (Thorat et al., 2019).

The XRD pattern of the ZnO was also shown in Figure-4.1 (b) and found to be in total agreement with the standard JCPDS pattern (JCPDS-36-1451) (H. Liu, Zhong, Govindaraju, & Yun, 2019). The diffraction peak at 2θ values of 31.68°, 34.4°, 36.17°, 47.53°, 56.6°, 62.88°, 64.39°, 68.03°, 69.14°, and 77.03° which correspond to (100), (002), (101), (102), (110), (103), (200), (112), (201), (004), and (202) diffraction planes of hexagonal wurtzite phase of ZnO.

The diffraction peaks at 2θ values of 18.9°, 31.6°, 36.8°, 44.8°, 59.3°, and 65.2° correspond to the cubic face-centered Co_3O_4 crystal planes of (111), (220) (211) (222) (400), (422), (511), (440), and (533), respectively (Figure-4.1 (b)). It was found that it had a good agreement with the reported results phase (JCPDS-43-1003) (W. Li et al., 2013).

The XRD patterns of g-C_3N4, g-C_3N_4/Co_3O_4, g-C_3N_4/ZnO, and prepared g-C_3N_4/ZnO/Co_3O_4 composite catalysts with different weight percent contents of zinc oxide and cobalt oxide to

graphitic carbon nitride are shown in Figure-4.1 (c). In the $gC_3N_4/ZnO/Co_3O_4$ composite display, the corresponding diffraction peaks of g-C_3N_4, hexagonal wurtzite ZnO, and cubic Co_3O_4 are evident. In the composites, a similar peak shape and position as g-C_3N_4, ZnO, and Co_3O_4 was observed as shown in Figure-4.1 (c). This means that the interaction of ZnO, Co_3O_4 with g-C_3N_4 does not affect the original lattice structure of g-C_3N_4. However, the diffraction peaks of ZnO and Co_3O_4 steadily strengthened at the cost of the g-C_3N_4 peaks as the ZnO and Co_3O_4concentrations increased. Furthermore, no additional peak is seen in the samples for any possible impurities or phases.

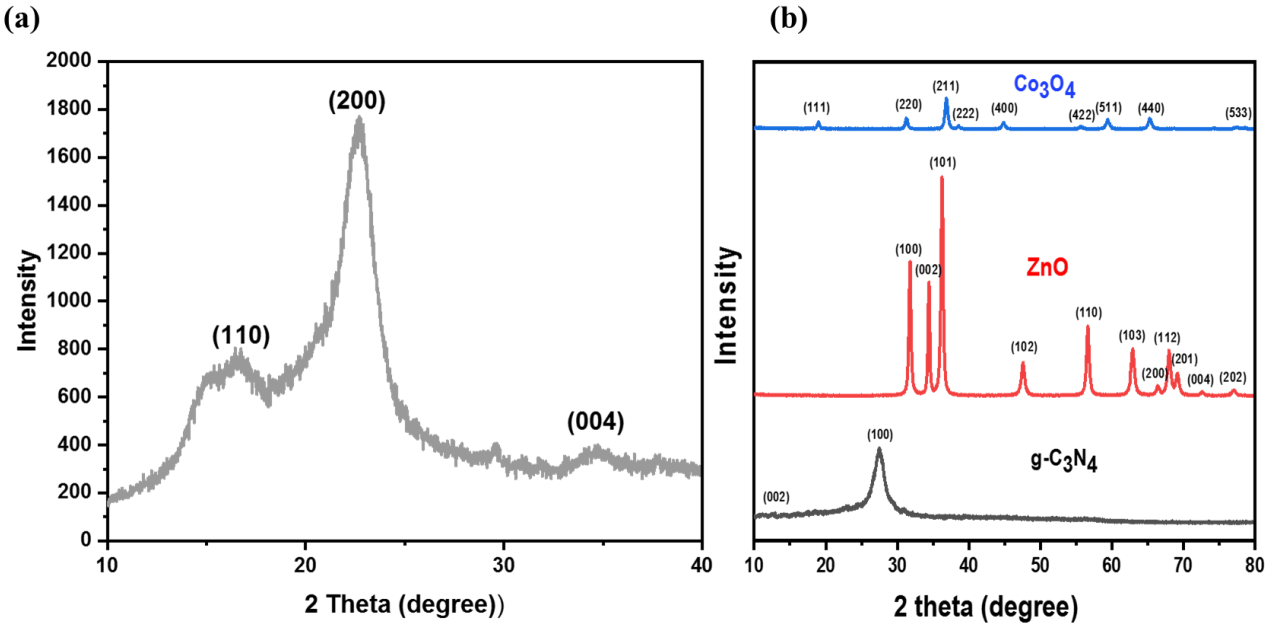

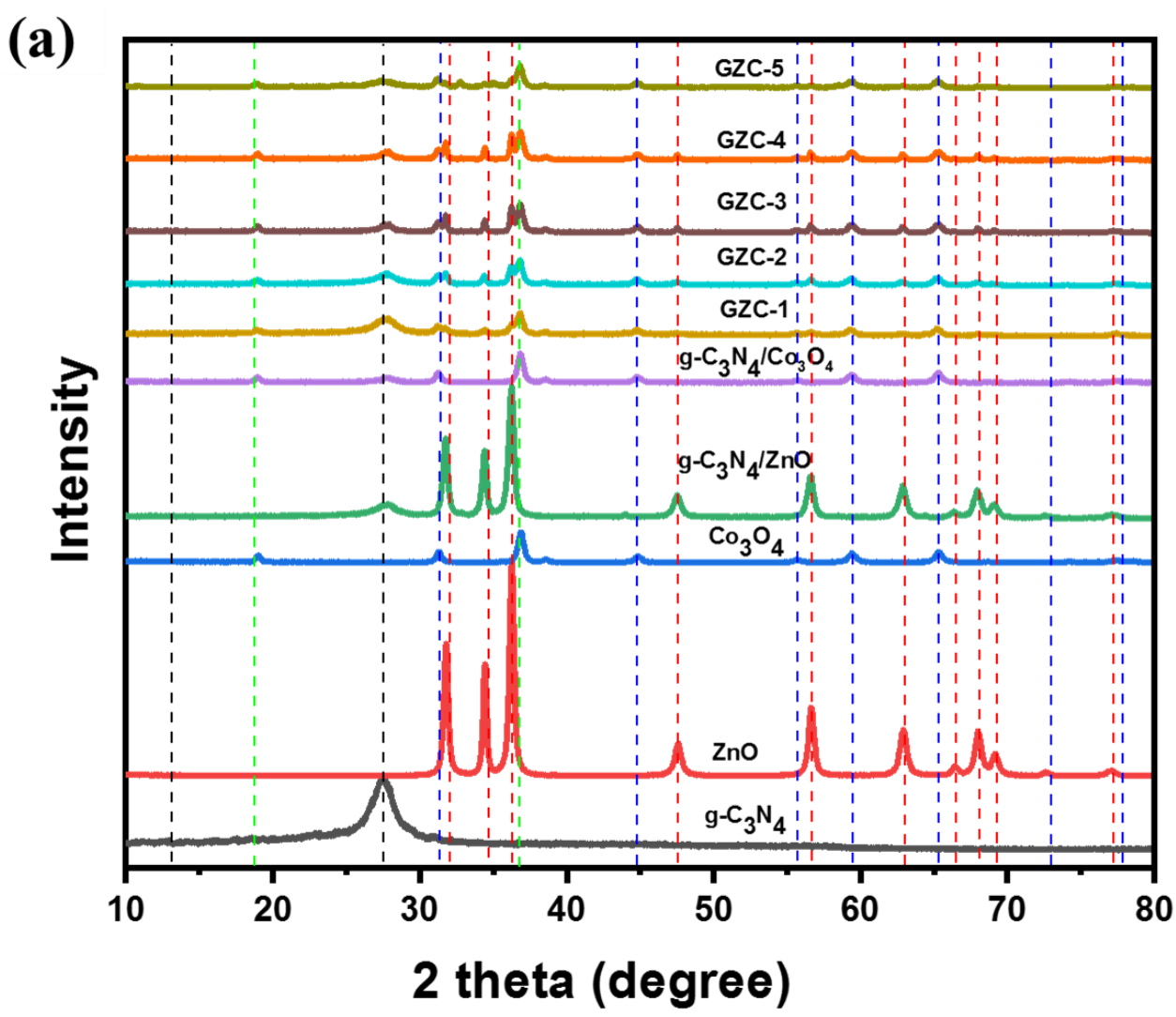

`Figure 4.1 XRD patterns of (a) cellulose (b) g-C_3N_4, ZnO, and Co_3O_4 (c) g-C_3N_4/Co_3O_4, g-C_3N_4/ZnO, and g-C_3N_4/ZnO/Co_3O_4 composite.

4.4.2 FTIR Analysis

The chemical bond of the as-prepared samples is analyzed through FTIR analysis. In Figure-4.2, three distinct bands were found in the spectrum of the pure g-C_3N_4 models, which were similar to the previous literature. The series of small vibration peaks in the wavenumber range of 1200–1650 cm^{-1} including 1238, 1318, 1410, 1574, and 1640 cm^{-1} are the characteristic peaks of heterocyclic aromatic C–N bonds, which are highly associated with the C = N, C–N, and C–N–C functional groups (L. Liu et al., 2008; W. Wang, Yu, Xia, Wong, & Li, 2013; Xiang, Yu, & Jaroniec, 2011; Shengming Yin, Han, Zhou, & Xu, 2015). The broad peak in the vicinity of 3000-3500 cm^{-1} is

ascribed to N–H stretching and deformation modes from residual amino groups (-NH_2, -NH) and that of O–H of the physically adsorbed water, respectively(F. Liu et al., 2017). The sharp typical peak at approximately 808 cm^{-1} corresponds to the s-triazine ring organization in g-C_3N_4 (Sheng Yin et al., 2016).

In Figure-4.2, the FTIR spectra of Co_3O_4, Three broad absorption bands were observed at ~ 3316, ~ 1400–1500, and ~ 430–830 cm^{-1}. The OH stretching and bending vibrations are represented by a broad band centered at 3416 cm^{-1} and a sharp band at 1635 cm^{-1}, which confirm that atmospheric water molecules are absorbed in the Co_3O_4 (Diallo, Beye, Doyle, Park, & Maaza, 2015; Mansournia & Rakhshan, 2016). Moreover, there are two particular bands produced from the stretching vibrations of the cobalt-oxygen bond. The first one is at 654 cm^{-1} and results from the vibrations of Co (III)-O bonds. Also, the second one is at 558 cm^{-1} and is related to Co-O stretching (Fouad, Makhlouf, Ali, & El-Sayed, 2011; F. Liu et al., 2017; Tang, Wang, & Chien, 2008).

In Figure-4.2, the FTIR spectra of ZnO, it was revealed that a broad absorption band at 3400 cm^{-1} was observed due to the stretching mode of O–H groups present in the sample might be due to moisture. The two absorption bands, found between 1380 cm^{-1} and 1420 cm^{-1} referred to the bending vibrations of the O–H groups (Cao et al., 1998). A sharp peak was also observed at 1110 cm^{-1} due to the stretching mode of the Zn–O bond (Qamar et al., 2021). The characteristic bands support the formation of the g-C_3N_4, ZnO, and Co_3O_4 phases as claimed in XRD analysis. After the addition of g-C_3N_4, ZnO, and Co_3O_4 the FTIR spectra of the GZC-3 composite only contain bands related to the corresponding g-C_3N_4, Co_3O_4, and ZnO functional groups, respectively, which confirms that the effective formation of g-C_3N_4-ZnO-Co_3O_4 composite as illustrated in Figure-4.2.

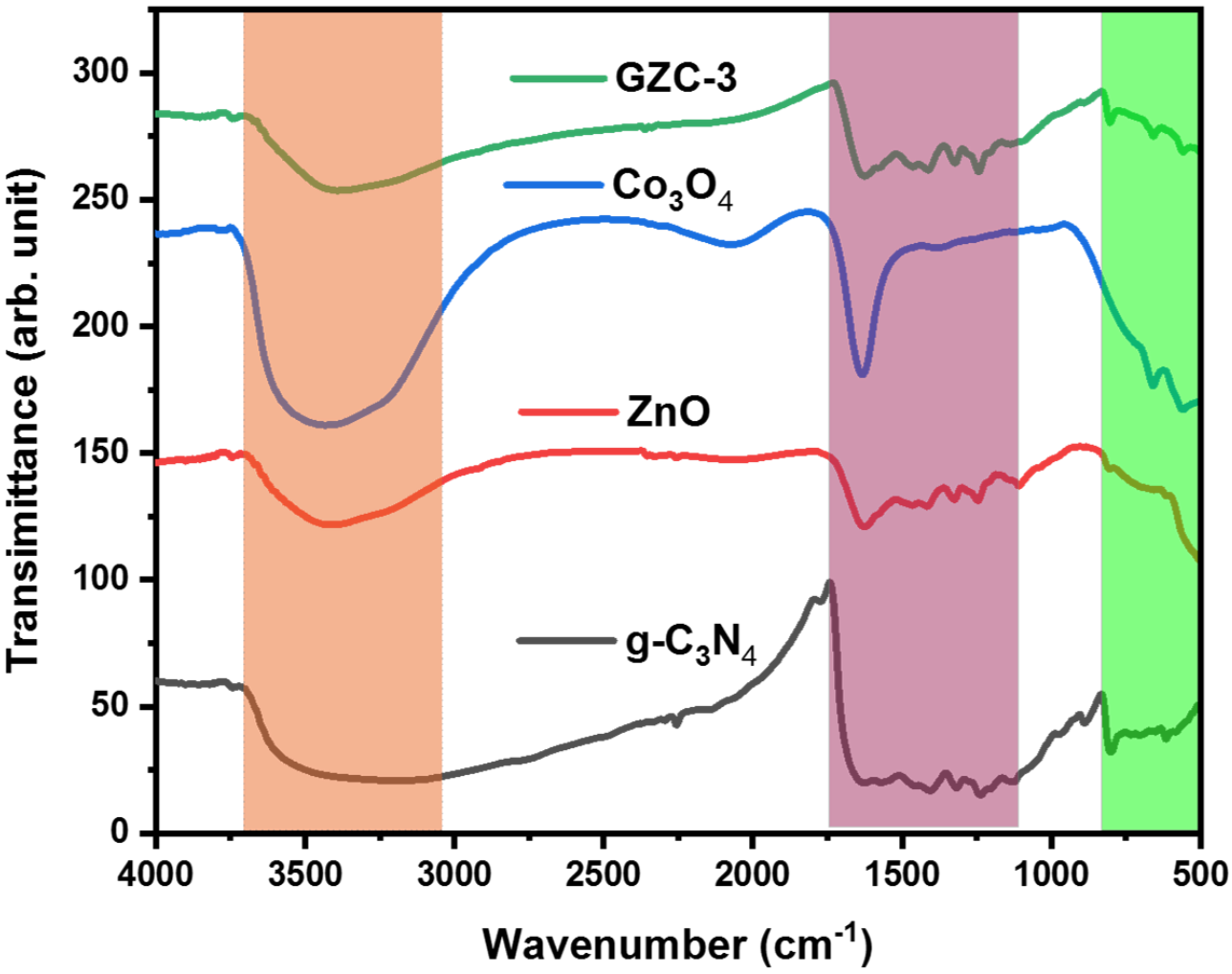

Figure 4.2 FTIR spectra of g-C_3N_4, ZnO, Co_3O_4, and GZC-3 composite.

4.1.3 SEM Analysis

The morphologies of all prepared samples were studied using SEM analysis. Cellulose templates can bind metal cations and regulate the particle size of metal oxide during the synthesis process. When cobalt (II) nitrate and zinc nitrate are mixed in a cellulose solution, the cobalt (II) nitrate and zinc nitrate hydrolyze and interact to generate a strong adhesion on the surface of the cellulose because cellulose is rich in hydrogen bonds and a hydroxyl macromolecule. The physical space from cellulose makes it difficult to form a large aggregation in the growth of these metal oxides. After calcination, the template is removed, resulting in ZnO and Co_3O_4 with reduced particle sizes and a porous structure.

Figure-4.3 (c and e) shows SEM images of a ZnO and Co_3O_4 template with cellulose, which has a characteristic of spherical and flowery-like form with a decreased size. In contrast, the catalyst generated without the use of cellulose has an aggregated shape and irregular big particle size (Figure-4.3 (b and d)). It was discovered that using a cellulose template to prepare ZnO and Co_3O_4 prevented particle aggregation, resulting in spherical and flower-like particle morphology and decreased particle size. The smaller granularity allows for faster passage of light-excited carriers to the particle surface for participation in the photocatalytic process, substantially lowering the carrier recombination rate (Wei, Faraj, Yao, Xie, & Lai, 2021). Furthermore, the flower-like structure allows the material to scatter light multiple times.

Figure-4.3 (a) displays a sheet-like structure for g-C_3N_4 which is often observed for g-C_3N_4 pyrolyzed from urea. Figure-4.3 (f) shows the morphology of the GZC-3 composite, indicating that the GZC-3 composite contains regular and scattered particles of ZnO and Co_3O_4 over the surface of g-C_3N_4.

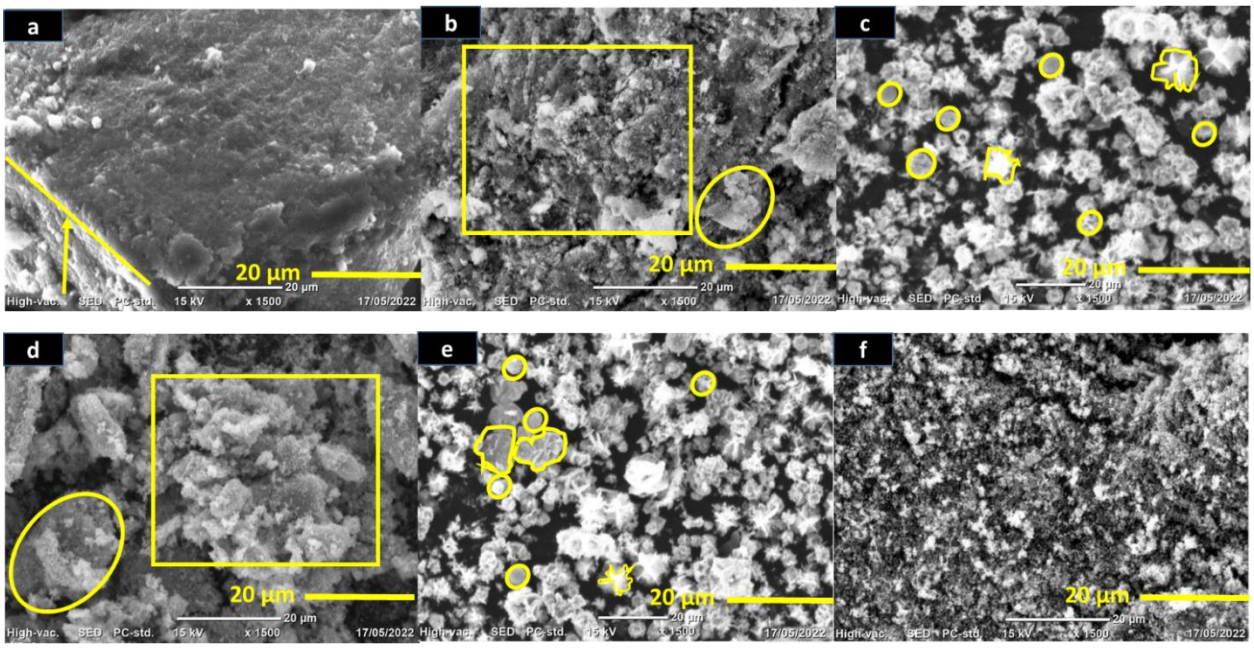

Figure 4.3 SEM image of (a) g-C_3N_4, (b) ZnO (without cellulose), (c) ZnO (with cellulose), (d) Co_3O_4(without cellulose), (e) Co_3O_4(with cellulose),and (f) GZC-3 composite.

4.1.4 UV Analysis

Using a UV–vis spectrometer, the optical absorption of as-prepared pure g-C_3N_4, ZnO, Co_3O_4, and composite samples was examined (Figure-4.4). As seen in the Figure-4.4 (a), pure ZnO exhibits

greater absorption in the UV region at wavelengths 382–384 nm, corresponding to an intrinsic band transition, which is consistent with earlier research (Suneel Kumar, Reddy, Kumar, Shankar, & Krishnan, 2018), and also Co_3O_4 exhibited a strong absorption tail at a wavelength longer than 500 nm (X. Zhao et al., 2018). Pure g-C_3N_4 displayed high absorption capabilities between 250 and 380 nm, with an absorption edge at 460 nm, which is still too large for efficient visible-light harvesting and leaves the majority of the visible light spectrum unexplored. The addition of Co_3O_4 particles to the g-C_3N_4-ZnO composite increased absorption strength while also redshifting the wavelength towards the visible light area (shifted to lower energy), as seen in Figure-4.4 (a). This might be because of the significant interaction between the bare samples. As a consequence, the addition of Co_3O_4 particles in g-C_3N_4 exhibits better visible light absorption, resulting in a higher number of electron-hole pairs, which is beneficial for wastewater treatment.

Furthermore, in the as-prepared samples, the energy bandgap was evaluated using the Tauc plot using UV–visible absorption spectra. The calculated energy bandgap was shown in Figure-4.4 (a, b, c, d, and e). The band gaps determined using Tauc's plots are determined to be 2.84, 3.16, 1.85, 2.93, 2.21, 2.63, 2.56, 2.47, 2.39, and 2.29 for g-C_3N_4, ZnO, Co_3O_4, GZ, GC, GZC-1, GZC-2, GZC-3, GZC-4, and GZC-5 composite, respectively. The energy bandgap in g-C_3N_4-ZnO composite decreases from 2.84 to 2.23 eV when Co_3O_4 particles are introduced. As a result, it may contribute to the increased photoactivity of g-C_3N_4 samples.

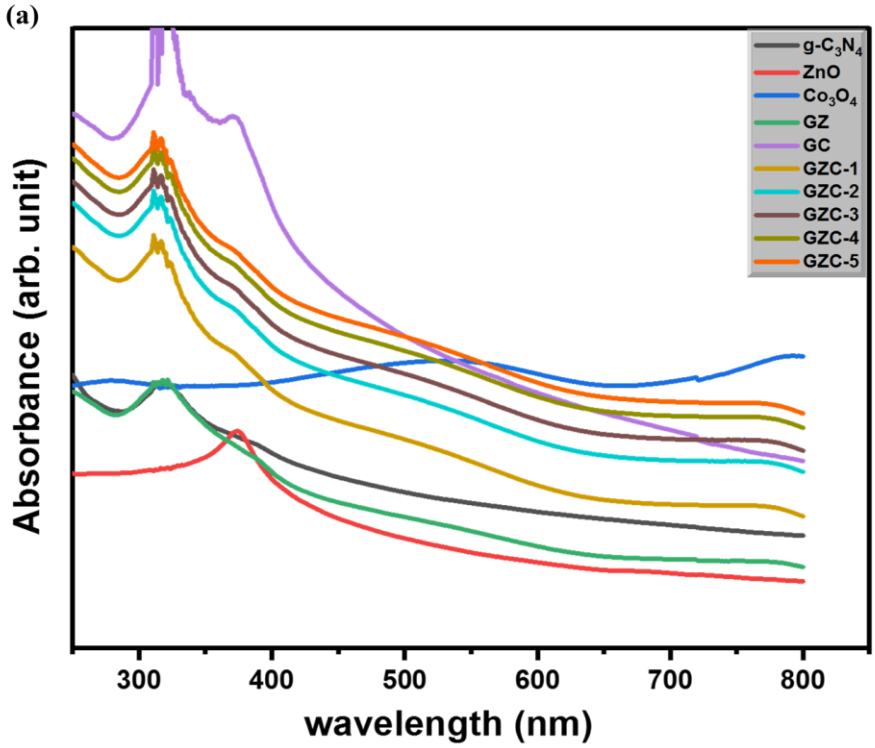
(a)
Absorbance (arb. unit)
wavelength (nm)
300
400
500
600
700
800
g-C3N4
ZnO
Co3O4
GZ
GC
GZC-1
GZC-2
GZC-3
GZC-4
GZC-5

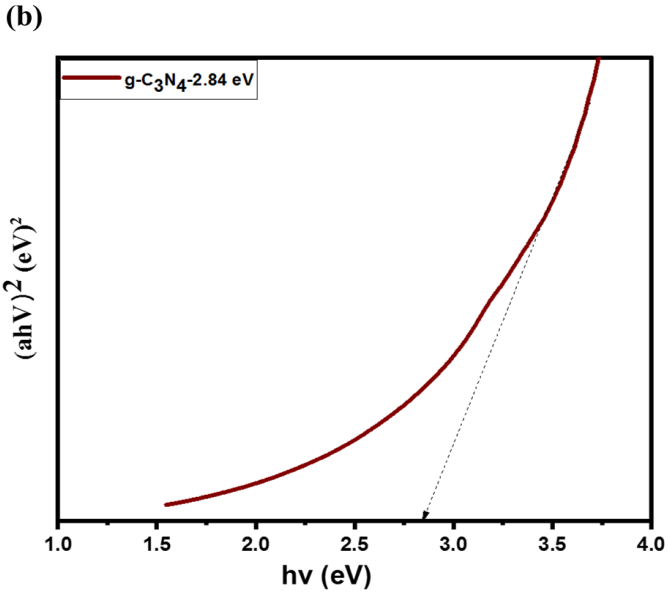
(b)
g-C3N4-2.84 eV
(ahV)2 (eV)2
hv (eV)
1.0
1.5
2.0
2.5
3.0
3.5
4.0

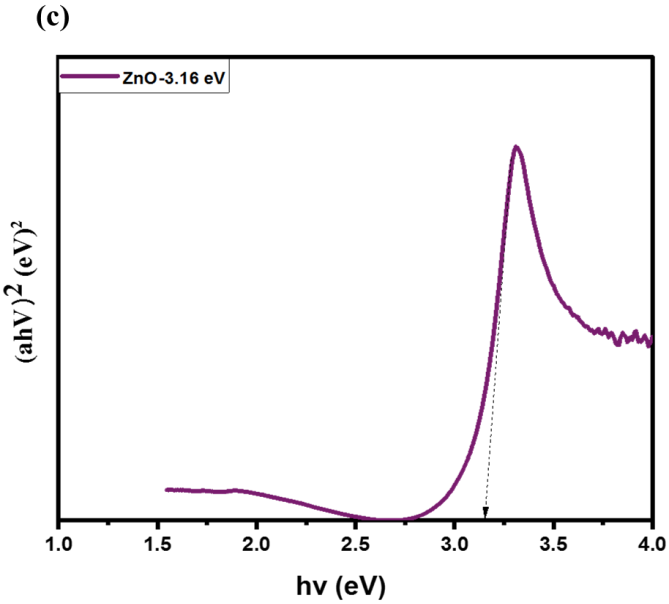
(c)
ZnO-3.16 eV
(ahV)2 (eV)2
hv (eV)
1.0
1.5
2.0
2.5
3.0
3.5
4.0

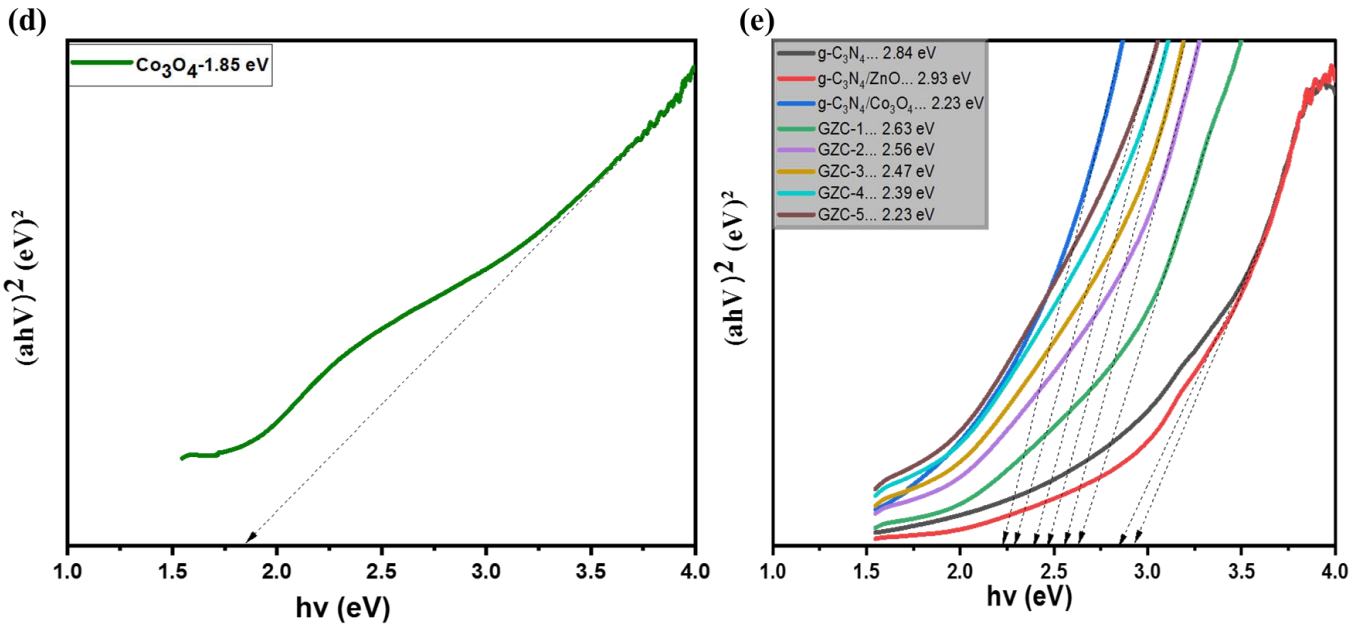

Figure 4.4 (a) UV-DRS spectra of all samples (b, c, and d) Tauc plot of g-C_3N_4, Co_3O_4, ZnO GZ, GC, GZC-1, GZC-2, GZC-3, GZC-4, and GZC-5 composite

4.1.5 BET Surface Area and Pore Size Analysis

From the BET measurements summarized in Table-4.1, In comparison to cellulose templated and non-cellulose template metal oxide samples, the surface area of ZnO without cellulose is 484.707 m^2/g compared to cellulose templated 538.563 m^2/g, and the surface area of cobalt oxide without cellulose is 48.673 m^2/g compared to cellulose templated 520.102 m^2/g. For cellulose templated ZnO and Co_3O_4, the total pore volume was 0.15 cm^3/g and 0.16 cm^3/g, respectively, whereas they were 0.11cm^3/g and 0.10 cm3/g for ZnO and Co_3O_4 without cellulose. The results show that using cellulose to prepare ZnO and Co_3O_4 is advantageous, with higher total pore volume and specific surface area, which can be attributed to high-temperature cellulose decomposition and the formation of a porous network structure of ZnO and Co_3O_4. g-C_3N_4 synthesized from the thermal polycondensation of a typical N-rich precursor, generally shows a limited surface area (<10 m^2/g^{-1}) (Q. Zheng et al., 2017). The sulfuric acid-treated g-C_3N_4 surface area and pore volumes show 47.136 m^2/g^{-1} and 0.09 cm^3/g respectively. As we can observe from Table-4.1 surface area of the GZC-3 composite (60.578 m^2/g) and the pore volume (0.12 cm^3/g) increased from bare g-C_3N_4. Increasing a photocatalyst surface area typically increases its reactivity because it provides more reaction sites and lowers the recombination of photogenerated electrons and holes (F. Guo et al., 2019). Because holes are substantially less mobile than electrons (Luque & Hegedus, 2011),

increasing surface area may enhance hole migration to the surface and subsequent reactions rather than hole recombination with electrons and resulting energy loss. Additionally, increasing the pore capacity of the GZC-3 composite allows for easier absorption of contaminants.

Table-4.1 Surface area and Total pore volume of samples

Samples	Surface area (m^2/g)	Total pore volume (cm^3/g)
ZnO (without cellulose)	**484.707**	**0.11**
ZnO (with cellulose)	**538.563**	**0.15**
Co_3O_4 (without cellulose)	**48.673**	**0.1**
Co_3O_4 (with cellulose)	**520.102**	**0.16**
g-C_3N_4	**47.136**	**0.09**
GZC	**60.578**	**0.12**

4.1.6 Photoluminescence (PL) Analysis

To examine the recombination extent of the photogenerated e^-/h^+ carriers in the prepared samples, photoluminescence (PL) spectra of the different weight percent of ZnO and Co_3O_4 were recorded. The room temperature PL spectra of pure g-C_3N_4 and all composites at exciton wavelength of 326 nm are shown in Figure-4.5. g-C_3N_4 has the maximum PL intensity by exhibiting wide emission peaks at 419 and 467 nm (Ahmad, 2020), demonstrating a high e^-/h^+ recombination rate in these catalysts. Coupling these catalysts showed significant PL quenching. In general, coupling two or more semiconductors prevents e^-/h^+ recombination and boosts photocatalytic activity. It can be observed from Figure-4.5 that PL emission intensity lowers in the following order g-C_3N_4 > GC > GZ > GZC-5 > GZC-4 > GZC-1 > GZC-2 > GZC-3. Among all synthesized catalysts GZC-3 reveals the lowest PL emission intensity than its counterparts, indicating the most effective inhibition for the recombination of photogenerated electron-hole pairs in these catalysts. Owing to effective charge separation, thus has the highest photocatalytic activities. The findings will be displayed in the photodegradation section.

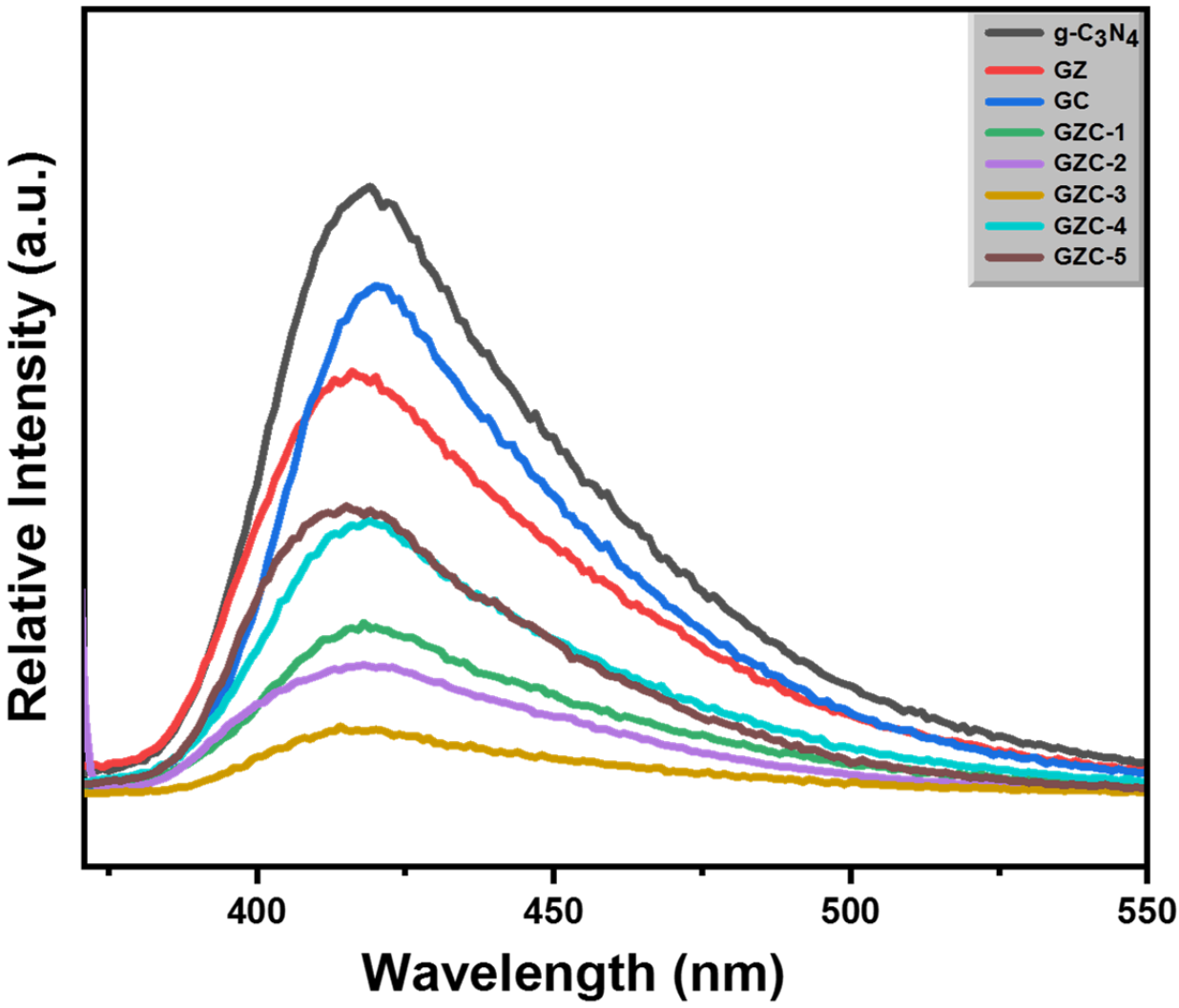

Figure 4.5 Photoluminescence emission spectra of g-C_3N_4, GZC-1, GZC-2, GZC-3, GZC-4, and GZC-5

4.1.7 The Nyquist Plots

Electrochemical impedance spectroscopy (EIS) is a powerful technique for understanding the transport of interface charges (B. Yu, Meng, Khan, Qin, & Liu, 2020). We examined the charge transfer resistances and interfacial charge separation efficiency of bare g-C_3N_4 and g-C_3N_4/ZnO/Co_3O_4 composite by electrochemical impedance spectroscopy (EIS) as shown in the Figure-4.6. During interfacial transport, the composites possess the smallest EIS semicircle radius compared to bare g-C_3N_4, implying the lowest impedance, which will permit the rapid transfer of photo charges. Based on the above results, GZC-3 has greater photocarrier separation and faster

charge transfer, which will enhance the lifetime of photocarriers thereby increasing the efficiency of photocatalysts. , which is also seen in photoluminescence as well.

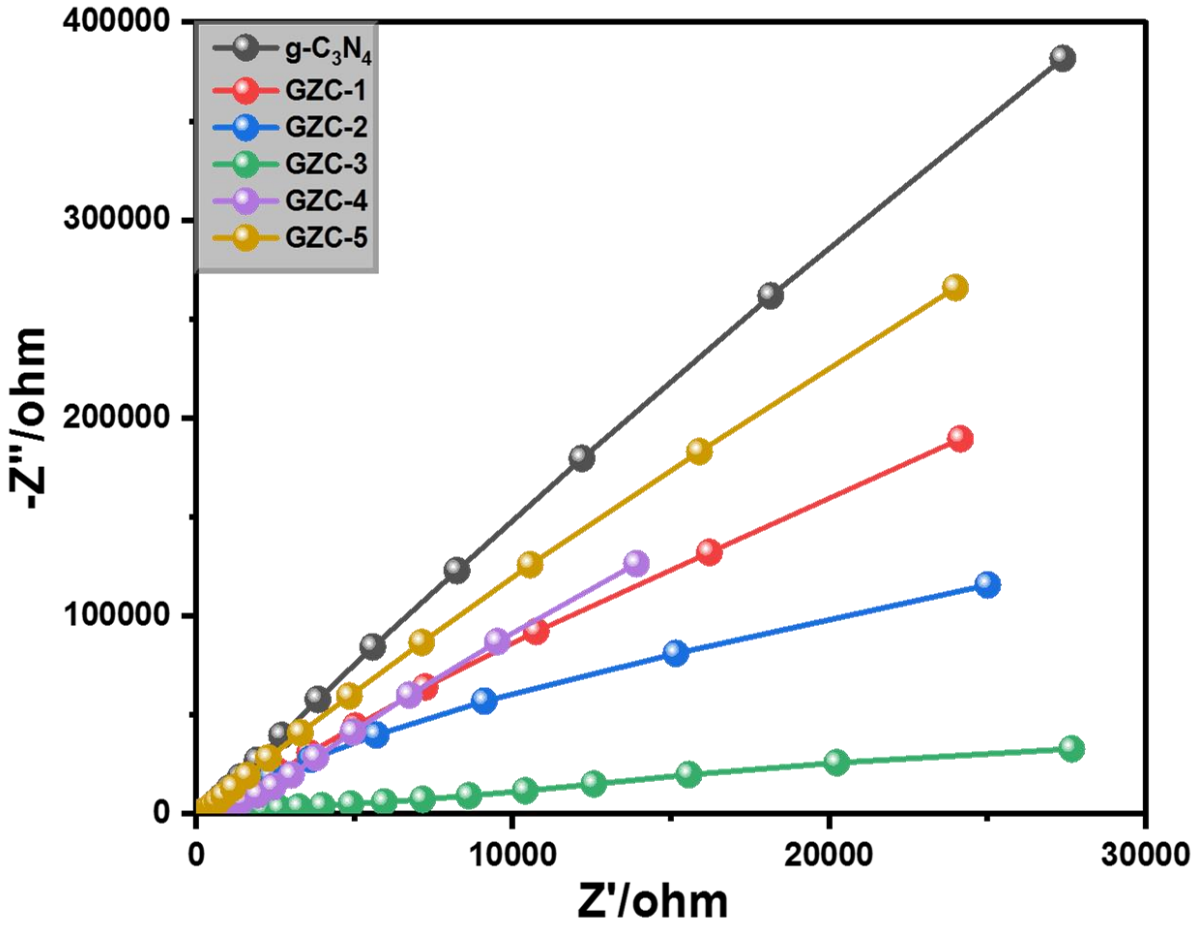

Figure 4.6 electrochemical impedance spectroscopy g-C_3N_4, GZC-1, GZC-2, GZC-3, GZC-4, and GZC-5

4.1.8 Photocatalytic Activity of the Samples

The degradation of the organic dye Methyl blue (MB) was used to assess the photocatalytic activity of as-prepared samples. Under visible light irradiation, the photocatalytic degradation efficiencies of various photocatalysts with different compositions were tested. Figure-4.7 (a-d) depicts the photocatalytic performances of various catalysts on the degradation of MB when exposed to visible light. Figure-4.7 (a) depicts the change in concentration of MB dye over time in the presence of GZC-3. The C_t/C_0 ratio, (where C_0 is the initial concentration of MB after the equilibrium adsorption and C_t is the concentration MB after visible light illuminated at a time (t)). As it is indicated in Figure-4.7 (b), the blank test indicates that in the absence of catalysts, MB is only weakly degraded, showing that photolysis can be discarded. The g-C_3N_4, ZnO, and Co_3O_4 exhibited photocatalytic degradation efficiency of 41.92, 45.10, and 50.40% of MB, respectively.

When g-C_3N_4, ZnO, and Co_3O_4 are combined to form binary or ternary composites, the resulting composite photocatalysts exhibit improved photodegradation activity. In particular, the ternary composite g-C_3N_4/ZnO/Co_3O_4 shows the most potential for photodegradation of MB. Among these composites, the GZC-3 composite had the maximum photodegradation activity, which photocatalysis 97.4% MB degradation after 60 minutes of photoreaction.

The degradation kinetic study is carried out to highlight the photodegradation activity of the materials as shown in Figure-4.7 (c). The pseudo-first-order kinetic equation $-\ln (C_t/C_0) = k_{app}t$ can be used to fit the degradation kinetic plots, where k_{app} and t represent the apparent first-order reaction rate constant and irradiation time. The resulting correlation coefficient values are shown in Table-4.2, they are all close to one, indicating that the photocatalytic degradation process follows the first-order reaction. On the other hand, observing the results of the kinetic plot in the Figure-4.7 (d), the GZC-3 composite has the largest value of k_{app} (0.001136 min^{-1}); in contrast, the k_{app} values for bare g-C_3N_4, ZnO, and Co_3O_4 are respectively 0.000137, 0.000154 and 0.0002025 min^{-1}. This implies that the GZC-3 composite has a photodegradation activity that is about 8.29, 7.38, and 5.60 times larger than that of bare g-C_3N_4, ZnO, and Co_3O_4, respectively.

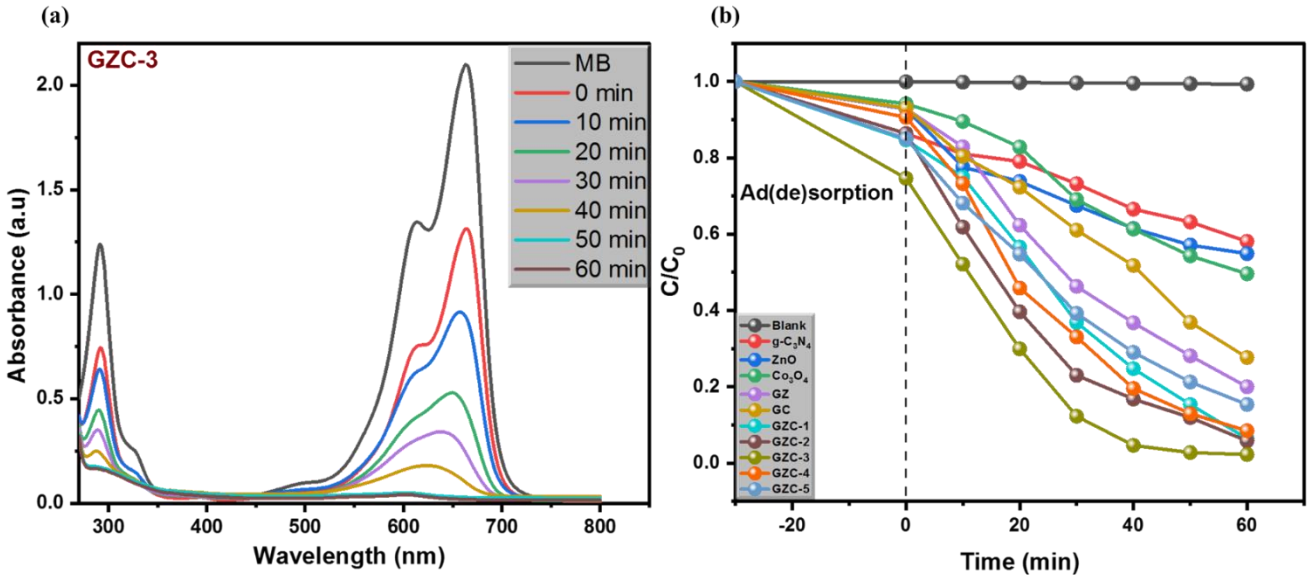

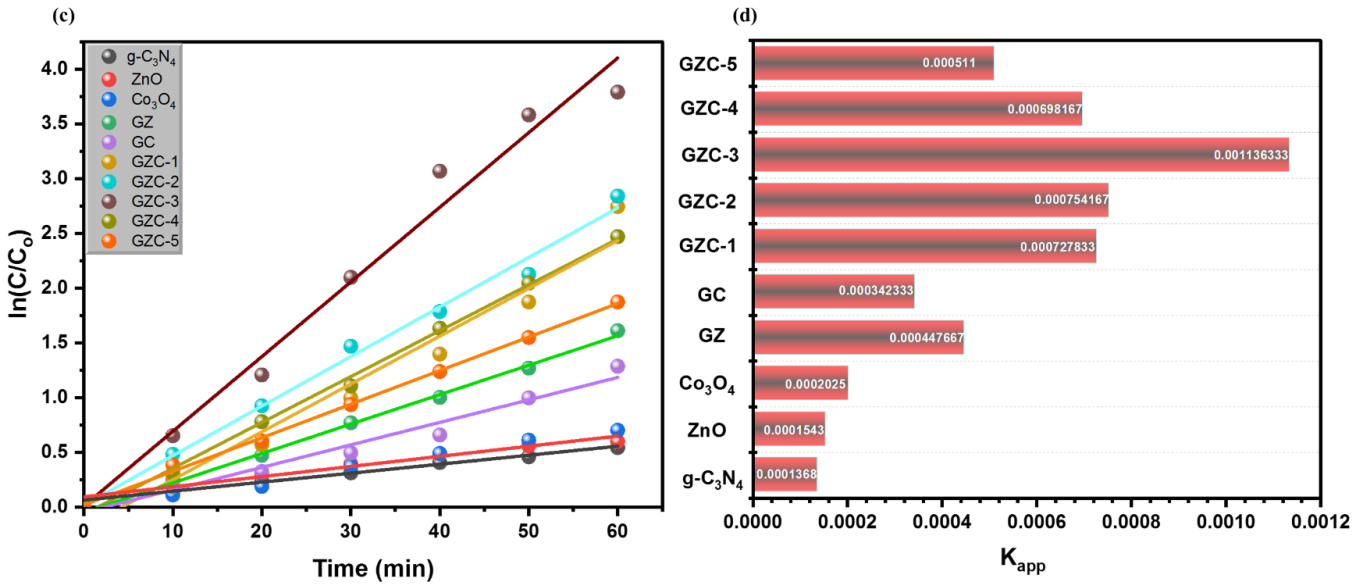

Figure 4.7 (a) Photocatalytic degradation of MB dyes (b) First-order kinetics in MB (c) degradation rate constant k (min^{-1}) of the as-prepared samples against g-C_3N_4, GZ, GC, GZC-1, GZC-2, GZC-3, GZC-4, and GZC-5

Table-4.2 Efficiency, K_{app}, R^2 values of the as-prepared samples.

Samples	Efficiency (%)	Kapp (min^{-1})	Correlation coefficient (R^2)
g-C_3N_4	**41.92**	**0.000137**	**0.94606**
ZnO	**45.1**	**0.000154**	**0.91847**
Co_3O_4	**50.4**	**0.000203**	**0.99151**
GZC-1	**93.56**	**0.000728**	**0.95585**
GZC-2	**94.16**	**0.000754**	**0.99036**
GZC-3	**97.74**	**0.001136**	**0.97613**
GZC-4	**91.54**	**0.000698**	**0.99648**
GZC-5	**84.64**	**0.000511**	**0.99774**
GC	**72.35551**	**0.000342**	**0.96373**
GZ	**80.01815**	**0.000448**	**0.99567**

4.1.9 Recyclability

The photostability of the GZC-3 composite is an important factor for practical application. Hence the stability. To investigate the recyclability of the GZC-3 composite, after finishing the photocatalytic reaction, the catalyst particles were separated from the dye solution, washed many times in double distilled water, and dried in an oven between each cycle. The catalyst particles were then utilized in fresh dye solutions under the same reaction conditions for another photocatalytic assay. The cyclic test was done four times, and the results are shown in Figure-4.8. A consistent MB degradation rate for all four cycles demonstrates that the GZC-3 composite may be employed four times without significant degradation efficiency reduction. The reusability results revealed a little decrease in photocatalytic degradation efficiency in each cycle. As shown in Figure-4.8, the photocatalytic degradation efficiency of the GZC-3 composite decreased from 97.4 percent to 93.4 % after the fourth cycle. But the negligible degradation efficiency dropping was observed which may be due to the loss of catalyst particles during the recovery process. It confirmed that the GZC-3 composite shows strong stability after four successive cycles against mixed organic dyes MB dyes which could be favorable for the real wastewater treatment process.

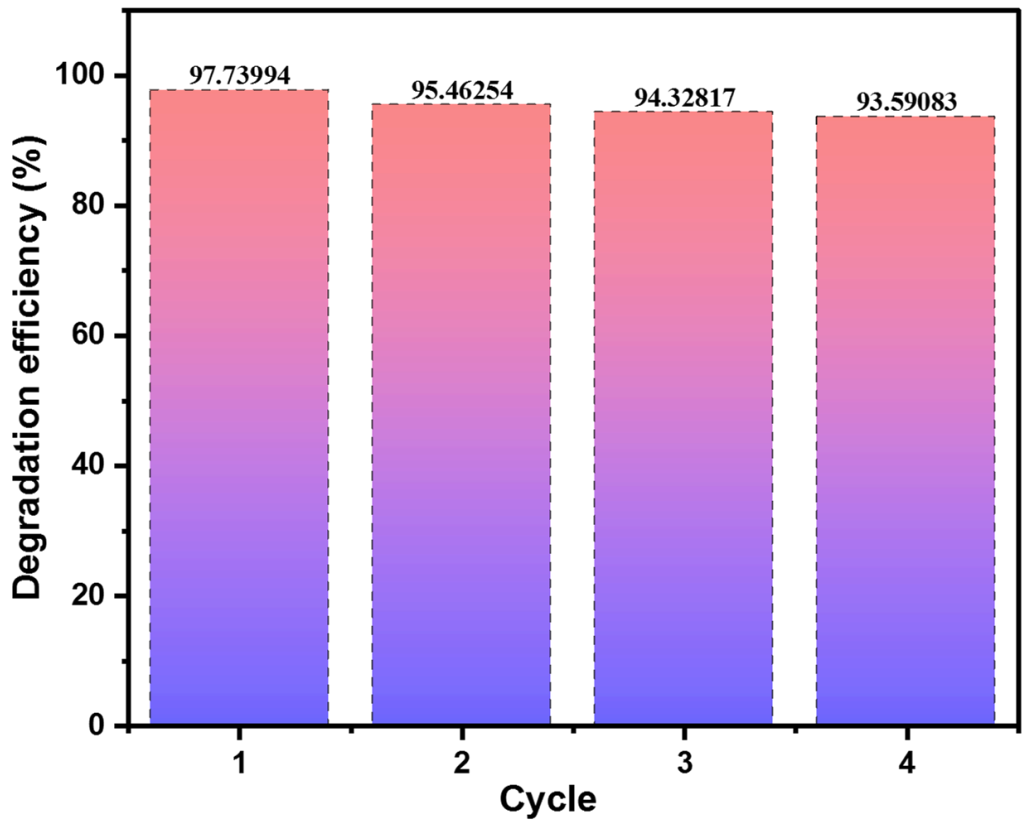

Figure 4.8 Recycle test of the GZC-3 composite.

4.1.10 Reaction Mechanism

To understand the photocatalytic mechanism of the g-C_3N_4/ZnO/Co_3O_4 ternary composites, the CB and VB potentials of g-C_3N_4, ZnO and Co_3O_4 were determined using the Mott-Schottky method Using electrochemical measurements at 800 Hz, Mott–Schottky plots of g-C_3N_4, ZnO, and Co_3O_4 are plotted in Figure-4.9 (a-c). By extrapolating the linear portion of the plot to the x-axis, we obtain the flat band potentials (V_{FB}) of g-C_3N_4, ZnO, and Co_3O_4 as -1.45, -1.01, and 1.42 V, respectively, versus Ag/AgCl electrodes. With reference to a normal hydrogen electrode (NHE), the flat band potential of the three semiconductors is correspondingly obtained as $V_{FB,\ g\text{-}C3N4}$ -1.25 V, $V_{FB,ZnO}$ -0.83 V, and $V_{FB,Co3O4}$ 2.82 V vs NHE. g-C_3N_4 and ZnO a behave as n-type semiconductivity due to the positive slope of their Mott–Schottky plots, and Co_3O_4 behaves as p-type semiconductivity due to the negative slope of its Mott–Schottky plot. As a result, the CB and VB potentials (vs NHE) of g-C_3N_4, ZnO, and Co_3O_4 are obtained, as seen in Figure-4.9 (d).

When the composite photocatalysts are irradiated by simulated sunlight the electrons on g-C_3N_4, ZnO, and Co_3O_4 are transferred from VB to CB. Owing to the staggered band structure configuration of g-C_3N_4, ZnO, and Co_3O_4, the Z-scheme electron transfer process could occur between the semiconductors. Meanwhile, under the driving of the potential variance, the photo-electrons are moved from the CB of the ZnO and Co_3O_4 transferred to the VB of g-C_3N_4. Consequently, the photogenerated electrons of g-C_3N_4 are finally transferred to the CB of g-C_3N_4 resulting in the whole process being revealed like a Z-scheme-based charge transfer process.

It is generally accepted that in most photocatalytic systems the main reactive species causing the dye degradation include photo excited holes and electron, hydroxyl ($OH^{\bullet}$) radicals, and superoxide ($O^{\bullet}$) radicals. The superoxide radicals are mainly produced through the reaction of adsorbed O_2 species with the photogenerated electrons in the CB of g-C_3N_4. This reaction process is thermodynamically feasible due to the sufficiently negative CB potential of g-C_3N_4 (-1.25 vs NHE) compared to E^o ($O^{\bullet}/O_2$) = -0.33 vs NHE. Furthermore, the VB potential of g-C_3N_4 (1.589 eV) is lower than that of $H_2O/OH^{\bullet}$ (2.32 eV). As a result, they are unable to convert water molecules into hydroxyl radicals (C. Jin et al., 2020; N. Yang et al., 2018). The main role of the photogenerated holes in the VB of ZnO and Co_3O_4 is to react with OH or H_2O species to produce $OH^{\bullet}$ radicals. The sufficiently positive VB potentials of ZnO (2.349 V Vs NHE) and Co_3O_4 (1.66 V Vs NHE) confirm these feasible reactions ($E^0(OH^{\bullet}/H_2O)$ =2.32 V Vs NHE) (C. Jin et al., 2020).

These observed electron transfer paths matched well with the direct dual Z-scheme mechanism which could enhance the transfer and separation efficiency of photo-generated charge carriers besides maintaining the strong redox capability for highly effective degradation of organic dye. The great separation efficiency of charge carriers gradually increases the contribution of e-h+ pairs to the oxidation and reduction processes. When compared to pristine samples, the g-C_3N_4/ZnO/Co_3O_4 composite catalyst has more free charge carriers, resulting in greater contributions to the degradation process. It is also observed in photoluminces and EIS measurements give support to the efficient separation of photoexcited electron/hole pairs in the g-C_3N_4/ZnO/Co_3O_4 composite.

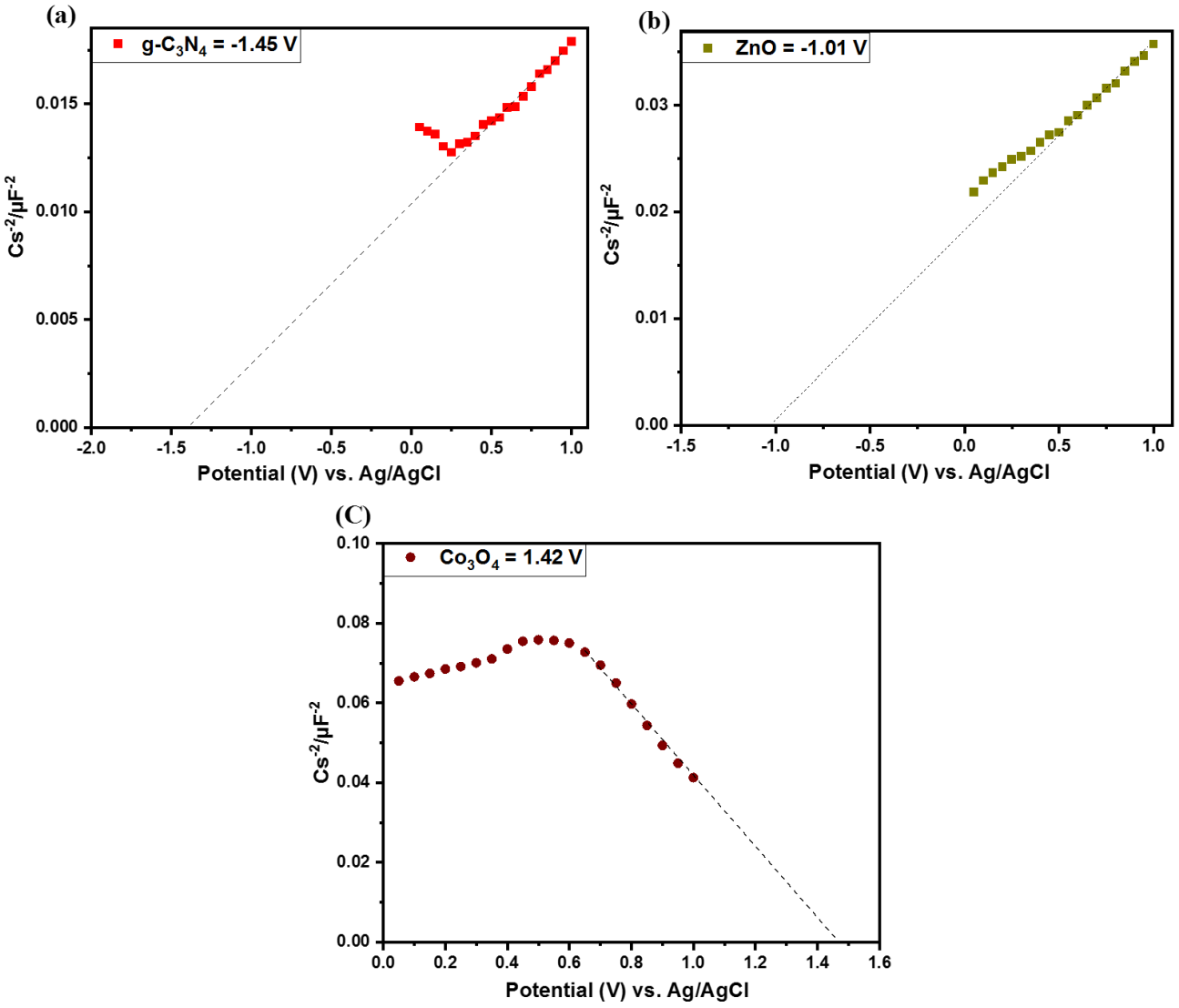

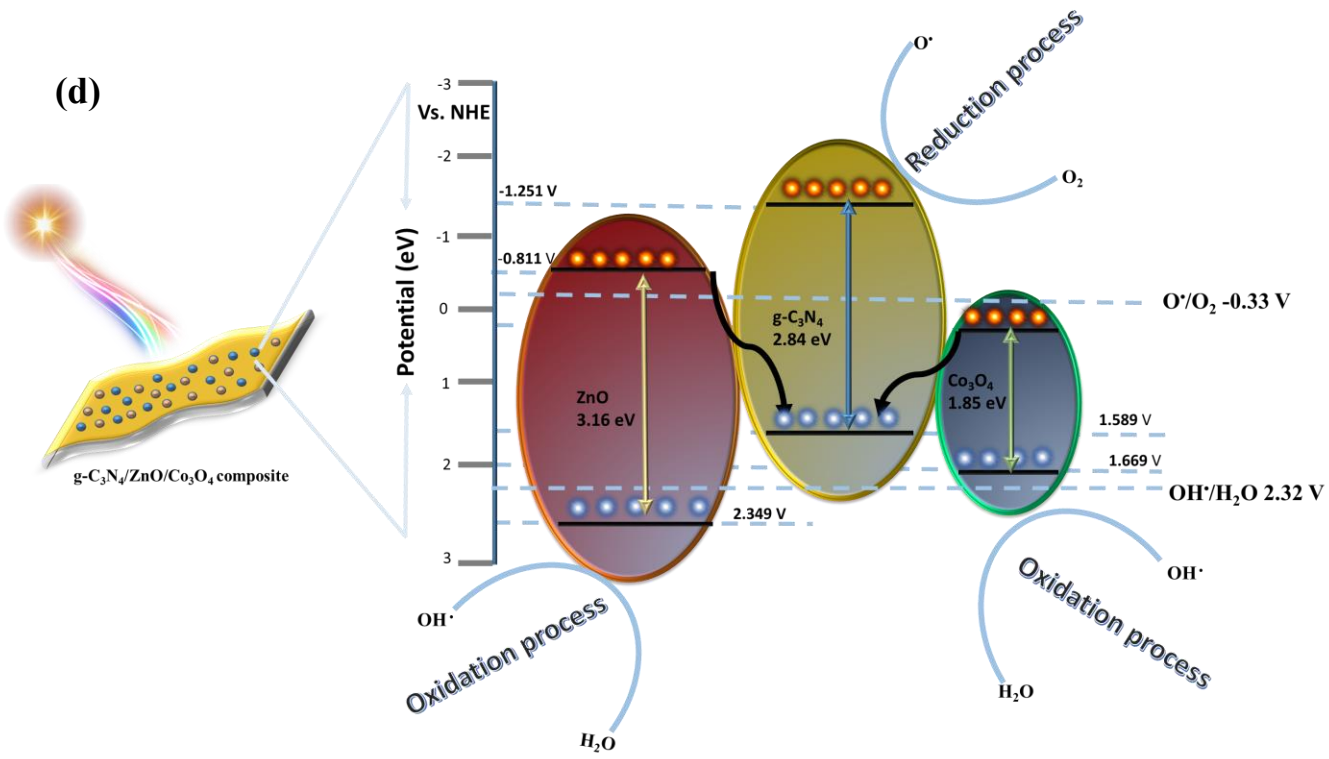

Figure 4.9 (a)–(c) Mott–Schottky plots of g-C_3N_4, ZnO, and Co_3O_4, respectively. (d) Possible photocatalytic degradation mechanism of g-C_3N_4/ZnO/Co_3O_4 composite against MB.

4.2 Conclusion

In summary, a dual Z-scheme g-C_3N_4/ZnO/Co_3O_4 composite was synthesized through a simple wet impregnation method. The phase, morphology and optical behavior of the synthesized samples are confirmed through various characterization techniques. It has been found that utilizing cellulose to prepare metal oxide increases surface area and inhibits agglomeration with greater particulate dispersion. While applying chemical exfolation, the surface area of graphatic carbon nitride increases, which has a positive influence on photocatalytic performance. The photocatalytic performance of the g-C_3N_4/ZnO/Co_3O_4 composite was higher than bare and other hybrid samples against MB organic dyes. The highest degradation efficiency was achieved for the GZC-3 heterojunction, which induced 97.4% degradation of MB within 60 min under visible light irradiation. The excellent photocatalytic performance of g-C_3N_4/ZnO/Co_3O_4 composite is due to the perfect band alignment, higher surface area, extended visible light absorption, and favorable charge carrier recombination respectively. In addition, the GZC-3 composite exhibit excellent photostability and stable cycle performance. A probable photocatalytic mechanism was suggested based on Mott–Schottky plots. This study may create a novel dual Z scheme g-C_3N_4/ZnO/Co_3O_4 photocatalyst for sewage treatment and other environmental remediation activities.

4.3 REFERENCE

Acharya, L., Nayak, S., Pattnaik, S. P., Acharya, R., & Parida, K. (2020). Resurrection of boron nitride in pn type-II boron nitride/B-doped-g-C3N4 nanocomposite during solid-state Z-scheme charge transfer path for the degradation of tetracycline hydrochloride. *Journal of colloid and interface science, 566*, 211-223.

Ahmad, I. (2020). Comparative study of metal (Al, Mg, Ni, Cu and Ag) doped ZnO/g-C3N4 composites: Efficient photocatalysts for the degradation of organic pollutants. *Separation and Purification Technology, 251*, 117372.

Alaghmandfard, A., & Ghandi, K. (2022). A Comprehensive Review of Graphitic Carbon Nitride (g-C3N4)–Metal Oxide-Based Nanocomposites: Potential for Photocatalysis and Sensing. *Nanomaterials, 12*(2), 294.

Ali, I., & Kim, J.-O. (2021). Optimization of photocatalytic performance of a gC3N4–TiO2 nanocomposite for phenol degradation in visible light. *Materials Chemistry and Physics, 261*, 124246.

Amorin, L. H., Suzuki, V. Y., de Paula, N. H., Duarte, J. L., da Silva, M. A. T., Taft, C. A., & La Porta, F. d. A. (2019). Electronic, structural, optical, and photocatalytic properties of graphitic carbon nitride. *New Journal of Chemistry, 43*(34), 13647-13653.

Amutha, C., Dhanalakshmi, A., Lawrence, B., Kulathuraan, K., Ramadas, V., & Natarajan, B. (2014). Influence of concentration on structural and optical characteristics of nanocrystalline ZnO thin films synthesized by Sol-Gel dip coating method. *Progress in Nanotechnology and Nanomaterials, 3*(1), 13-18.

Bai, X., Li, J., & Cao, C. (2010). Synthesis of hollow carbon nitride microspheres by an electrodeposition method. *Applied surface science, 256*(8), 2327-2331.

Bernhard, A. M., Peitz, D., Elsener, M., Wokaun, A., & Kröcher, O. (2012). Hydrolysis and thermolysis of urea and its decomposition byproducts biuret, cyanuric acid and melamine over anatase TiO2. *Applied Catalysis B: Environmental, 115*, 129-137.

Brodowska, A. J., Nowak, A., & Śmigielski, K. (2018). Ozone in the food industry: Principles of ozone treatment, mechanisms of action, and applications: An overview. *Critical reviews in food science and nutrition, 58*(13), 2176-2201.

Cai, H., Wang, B., Xiong, L., Bi, J., Yuan, L., Yang, G., & Yang, S. (2019). Orienting the charge transfer path of type-II heterojunction for photocatalytic hydrogen evolution. *Applied Catalysis B: Environmental, 256*, 117853.

Cao, H., Zhao, Y., Ong, H., Ho, S., Dai, J. Y., Wu, J. Y., & Chang, R. (1998). Ultraviolet lasing in resonators formed by scattering in semiconductor polycrystalline films. *Applied Physics Letters, 73*(25), 3656-3658.

Chang, F., Xie, Y., Li, C., Chen, J., Luo, J., Hu, X., & Shen, J. (2013). A facile modification of g-C3N4 with enhanced photocatalytic activity for degradation of methylene blue. *Applied Surface Science, 280*, 967-974.

Cui, Y., Zhang, J., Zhang, G., Huang, J., Liu, P., Antonietti, M., & Wang, X. (2011). Synthesis of bulk and nanoporous carbon nitride polymers from ammonium thiocyanate for photocatalytic hydrogen evolution. *Journal of Materials Chemistry, 21*(34), 13032-13039.

Das, D., Banerjee, D., Das, B., Das, N., & Chattopadhyay, K. (2017). Effect of cobalt doping into graphitic carbon nitride on photo induced removal of dye from water. *Materials Research Bulletin, 89*, 170-179.

Das, S., & Daud, W. W. (2014). RETRACTED: Photocatalytic CO2 transformation into fuel: A review on advances in photocatalyst and photoreactor: Elsevier.

de Lima, B. R. M., do Nascimento, N. M. P., Zamian, J. R., da Costa, C. E. F., do Nascimento, L. A. S., Carneiro-Moreira, S. G., & da Rocha Filho, G. N. (2020). Higher dye degradation using a visible-light

photocatalyst made of mesoporous graphitic carbon nitride prepared with the Tween-40 surfactant. *Environmental Chemistry Letters, 18*(4), 1413-1422.

Diallo, A., Beye, A., Doyle, T. B., Park, E., & Maaza, M. (2015). Green synthesis of Co3O4 nanoparticles via Aspalathus linearis: physical properties. *Green Chemistry Letters and Reviews, 8*(3-4), 30-36.

Dong, F., Li, Y., Wang, Z., & Ho, W.-K. (2015). Enhanced visible light photocatalytic activity and oxidation ability of porous graphene-like g-C3N4 nanosheets via thermal exfoliation. *Applied surface science, 358*, 393-403.

Dong, G., Zhang, Y., Pan, Q., & Qiu, J. (2014). A fantastic graphitic carbon nitride (g-C3N4) material: electronic structure, photocatalytic and photoelectronic properties. *Journal of photochemistry and photobiology C: photochemistry reviews, 20*, 33-50.

Dontsova, D., Pronkin, S., Wehle, M., Chen, Z., Fettkenhauer, C., Clavel, G., & Antonietti, M. (2015). Triazoles: a new class of precursors for the synthesis of negatively charged carbon nitride derivatives. *Chemistry of Materials, 27*(15), 5170-5179.

Du, C., Zhang, Z., Tan, S., Yu, G., Chen, H., Zhou, L., . . . Deng, F. (2021). Construction of Z-scheme g-C3N4/MnO2/GO ternary photocatalyst with enhanced photodegradation ability of tetracycline hydrochloride under visible light radiation. *Environmental Research, 200*, 111427.

Dubey, S., Kumar, J., Kumar, A., & Sharma, Y. C. (2018). Facile and green synthesis of highly dispersed cobalt oxide (Co3O4) nano powder: Characterization and screening of its eco-toxicity. *Advanced Powder Technology, 29*(11), 2583-2590.

Dyjak, S., Kiciński, W., & Huczko, A. (2015). Thermite-driven melamine condensation to C x N y H z graphitic ternary polymers: towards an instant, large-scale synthesis of gC 3 N 4. *Journal of materials chemistry A, 3*(18), 9621-9631.

Ehrmaier, J., Domcke, W., & Opalka, D. (2018). Mechanism of photocatalytic water oxidation by graphitic carbon nitride. *The Journal of Physical Chemistry Letters, 9*(16), 4695-4699.

Eom, T.-H., Lee, C.-H., Kim, J.-H., & Lee, C.-H. (2005). Development of an ion exchange system for plating wastewater treatment. *Desalination, 180*(1-3), 163-172.

Feng, S., Chen, T., Liu, Z., Shi, J., Yue, X., & Li, Y. (2020). Z-scheme CdS/CQDs/g-C3N4 composites with visible-near-infrared light response for efficient photocatalytic organic pollutant degradation. *Science of the total Environment, 704*, 135404.

Focazio, M. J., Kolpin, D. W., Barnes, K. K., Furlong, E. T., Meyer, M. T., Zaugg, S. D., . . . Thurman, M. E. (2008). A national reconnaissance for pharmaceuticals and other organic wastewater contaminants in the United States—II) Untreated drinking water sources. *Science of the total Environment, 402*(2-3), 201-216.

Fonash, S. (2010). Solar Cell Device Physics 2nd edn (New York: Academic): Academic Press, Burlington, MA, USA.

Fouad, O. A., Makhlouf, S. A., Ali, G. A., & El-Sayed, A. (2011). Cobalt/silica nanocomposite via thermal calcination-reduction of gel precursors. *Materials Chemistry and Physics, 128*(1-2), 70-76.

Fox, M. A., & Dulay, M. T. (1993). Heterogeneous photocatalysis. *Chemical reviews, 93*(1), 341-357.

Fujishima, A., & Honda, K. (1972). Electrochemical photolysis of water at a semiconductor electrode. *nature, 238*(5358), 37-38.

Gabriel, T., Belete, A., Syrowatka, F., Neubert, R. H., & Gebre-Mariam, T. (2020). Extraction and characterization of celluloses from various plant byproducts. *International Journal of Biological Macromolecules, 158*, 1248-1258.

Ganganboina, A. B., Nguyen, M. D., Nguyen, T. H. L., Kuncoro, E. P., & Doong, R.-A. (2021). Boron and phosphorus co-doped one-dimensional graphitic carbon nitride for enhanced visible-light-driven photodegradation of diclofenac. *Chemical Engineering Journal, 425*, 131520.

Gillan, E. G. (2000). Synthesis of nitrogen-rich carbon nitride networks from an energetic molecular azide precursor. *Chemistry of Materials, 12*(12), 3906-3912.

Gizaw, Z. (2014). Food safety practice and associated factors of food handlers working in substandard food establishments in Gondar Town, Northwest Ethiopia, 2013/14.

Gong, Y., Quan, X., Yu, H., & Chen, S. (2017). Synthesis of Z-scheme Ag2CrO4/Ag/g-C3N4 composite with enhanced visible-light photocatalytic activity for 2, 4-dichlorophenol degradation. *Applied Catalysis B: Environmental, 219*, 439-449.

Goswami, M., Adhikary, N. C., & Bhattacharjee, S. (2018). Effect of annealing temperatures on the structural and optical properties of zinc oxide nanoparticles prepared by chemical precipitation method. *Optik, 158*, 1006-1015.

Gu, Q., Gong, X., Jia, Q., Liu, J., Gao, Z., Wang, X., . . . Xue, C. (2017). Compact carbon nitride based copolymer films with controllable thickness for photoelectrochemical water splitting. *Journal of Materials Chemistry A, 5*(36), 19062-19071.

Guo, F., Li, M., Ren, H., Huang, X., Shu, K., Shi, W., & Lu, C. (2019). Facile bottom-up preparation of Cl-doped porous g-C3N4 nanosheets for enhanced photocatalytic degradation of tetracycline under visible light. *Separation and Purification Technology, 228*, 115770.

Guo, S., Tang, Y., Xie, Y., Tian, C., Feng, Q., Zhou, W., & Jiang, B. (2017). P-doped tubular g-C3N4 with surface carbon defects: universal synthesis and enhanced visible-light photocatalytic hydrogen production. *Applied Catalysis B: Environmental, 218*, 664-671.

Han, C., Ge, L., Chen, C., Li, Y., Xiao, X., Zhang, Y., & Guo, L. (2014). Novel visible light induced Co3O4-g-C3N4 heterojunction photocatalysts for efficient degradation of methyl orange. *Applied Catalysis B: Environmental, 147*, 546-553.

He, C., Zhang, J., Zhang, W., & Li, T. (2019). Type-II InSe/g-C3N4 heterostructure as a high-efficiency oxygen evolution reaction catalyst for photoelectrochemical water splitting. *The Journal of Physical Chemistry Letters, 10*(11), 3122-3128.

He, R., Liang, H., Li, C., & Bai, J. (2020). Enhanced photocatalytic hydrogen production over Co3O4@ g-C3N4 pn junction adhering on one-dimensional carbon fiber. *Colloids and Surfaces A: Physicochemical and Engineering Aspects, 586*, 124200.

Hignite, C., & Azarnoff, D. L. (1977). Drugs and drug metabolites as environmental contaminants: chlorophenoxyisobutyrate and salicylic acid in sewage water effluent. *Life Sciences, 20*(2), 337-341.

Hong, J., Xia, X., Wang, Y., & Xu, R. (2012). Mesoporous carbon nitride with in situ sulfur doping for enhanced photocatalytic hydrogen evolution from water under visible light. *Journal of Materials Chemistry, 22*(30), 15006-15012.

Hong, Y., Tian, C., Jiang, B., Wu, A., Zhang, Q., Tian, G., & Fu, H. (2013). Facile synthesis of sheet-like ZnO assembly composed of small ZnO particles for highly efficient photocatalysis. *Journal of materials chemistry A, 1*(18), 5700-5708.

Hu, C., Chu, Y.-C., Wang, M.-S., & Wu, X.-H. (2017). Rapid synthesis of g-C3N4 spheres using microwave-assisted solvothermal method for enhanced photocatalytic activity. *Journal of Photochemistry and Photobiology A: Chemistry, 348*, 8-17.

Hu, S., Li, F., Fan, Z., Wang, F., Zhao, Y., & Lv, Z. (2015). Band gap-tunable potassium doped graphitic carbon nitride with enhanced mineralization ability. *Dalton Transactions, 44*(3), 1084-1092.

Hu, S., Yang, L., Tian, Y., Wei, X., Ding, J., Zhong, J., & Chu, P. (2015). Simultaneous nanostructure and heterojunction engineering of graphitic carbon nitride via in situ Ag doping for enhanced photoelectrochemical activity. *Applied Catalysis B: Environmental, 163*, 611-622.

Huang, J., Li, D., Li, R., Zhang, Q., Chen, T., Liu, H., . . . Liu, G. (2019). An efficient metal-free phosphorus and oxygen co-doped g-C3N4 photocatalyst with enhanced visible light photocatalytic activity for the degradation of fluoroquinolone antibiotics. *Chemical Engineering Journal, 374*, 242-253.

Huang, T., Chen, J., Zhang, L., Khataee, A., Han, Q., Liu, X., . . . Wang, X. (2022). Precursor-modified strategy to synthesize thin porous amino-rich graphitic carbon nitride with enhanced photocatalytic

degradation of RhB and hydrogen evolution performances. *Chinese Journal of Catalysis, 43*(2), 497-506.

Hube, S., Eskafi, M., Hrafnkelsdóttir, K. F., Bjarnadóttir, B., Bjarnadóttir, M. Á., Axelsdóttir, S., & Wu, B. (2020). Direct membrane filtration for wastewater treatment and resource recovery: A review. *Science of the total Environment, 710*, 136375.

Ji, X., Yuan, X., Wu, J., Yu, L., Guo, H., Wang, H., . . . Zhao, Y. (2017). Tuning the photocatalytic activity of graphitic carbon nitride by plasma-based surface modification. *ACS applied materials & interfaces, 9*(29), 24616-24624.

Jia, T., Fu, F., Li, J., Deng, Z., Long, F., Yu, D., . . . Wang, W. (2020). Rational construction of direct Z-scheme SnS/g-C3N4 hybrid photocatalyst for significant enhancement of visible-light photocatalytic activity. *Applied Surface Science, 499*, 143941.

Jiang, L., Yuan, X., Zeng, G., Liang, J., Chen, X., Yu, H., . . . Xiong, T. (2018). In-situ synthesis of direct solid-state dual Z-scheme WO3/g-C3N4/Bi2O3 photocatalyst for the degradation of refractory pollutant. *Applied Catalysis B: Environmental, 227*, 376-385.

Jin, C., Kang, J., Li, Z., Wang, M., Wu, Z., & Xie, Y. (2020). Enhanced visible light photocatalytic degradation of tetracycline by MoS2/Ag/g-C3N4 Z-scheme composites with peroxymonosulfate. *Applied Surface Science, 514*, 146076.

Jin, R., Hu, S., Gui, J., & Liu, D. (2015). A convenient method to prepare novel rare earth metal ce-doped carbon nitride with enhanced photocatalytic activity under visible light. *Bulletin of the Korean Chemical Society, 36*(1), 17-23.

Jo, W.-K., & Natarajan, T. S. (2015). Influence of TiO2 morphology on the photocatalytic efficiency of direct Z-scheme g-C3N4/TiO2 photocatalysts for isoniazid degradation. *Chemical Engineering Journal, 281*, 549-565.

Jourshabani, M., Shariatinia, Z., & Badiei, A. (2017). Controllable synthesis of mesoporous sulfur-doped carbon nitride materials for enhanced visible light photocatalytic degradation. *Langmuir, 33*(28), 7062-7078.

Jung, H., Pham, T.-T., & Shin, E. W. (2018). Interactions between ZnO nanoparticles and amorphous g-C3N4 nanosheets in thermal formation of g-C3N4/ZnO composite materials: The annealing temperature effect. *Applied surface science, 458*, 369-381.

Khurram, R., Nisa, Z. U., Javed, A., Wang, Z., & Hussien, M. A. (2022). Synthesis and Characterization of an α-Fe2O3-Decorated g-C3N4 Heterostructure for the Photocatalytic Removal of MO. *Molecules, 27*(4), 1442.

Kong, X., Liu, X., Zheng, Y., Chu, P. K., Zhang, Y., & Wu, S. (2021). Graphitic carbon nitride-based materials for photocatalytic antibacterial application. *Materials Science and Engineering: R: Reports, 145*, 100610.

Kroke, E., Schwarz, M., Horath-Bordon, E., Kroll, P., Noll, B., & Norman, A. D. (2002). Tri-s-triazine derivatives. Part I. From trichloro-tri-s-triazine to graphitic C 3 N 4 structures. *New Journal of Chemistry, 26*(5), 508-512.

Kumar, S., Karthikeyan, S., & Lee, A. F. (2018). g-C3N4-based nanomaterials for visible light-driven photocatalysis. *Catalysts, 8*(2), 74.

Kumar, S., Reddy, N. L., Kumar, A., Shankar, M. V., & Krishnan, V. (2018). Two dimensional N-doped ZnO-graphitic carbon nitride nanosheets heterojunctions with enhanced photocatalytic hydrogen evolution. *International journal of hydrogen energy, 43*(8), 3988-4002.

Kumar, S., Surendar, T., Kumar, B., Baruah, A., & Shanker, V. (2014). Synthesis of highly efficient and recyclable visible-light responsive mesoporous gC 3 N 4 photocatalyst via facile template-free sonochemical route. *Rsc Advances, 4*(16), 8132-8137.

Le, S., Jiang, T., Zhao, Q., Liu, X., Li, Y., Fang, B., & Gong, M. (2016). Cu-doped mesoporous graphitic carbon nitride for enhanced visible-light driven photocatalysis. *Rsc Advances, 6*(45), 38811-38819.

Lee, K. E., Morad, N., Teng, T. T., & Poh, B. T. (2012). Development, characterization and the application of hybrid materials in coagulation/flocculation of wastewater: A review. *Chemical Engineering Journal, 203*, 370-386.

Lei, L., Wang, W., Wang, C., Zhang, M., Zhong, Q., & Fan, H. (2021). In situ growth of boron doped g-C3N4 on carbon fiber cloth as a recycled flexible film-photocatalyst. *Ceramics International, 47*(1), 1258-1267.

Lellis, B., Fávaro-Polonio, C. Z., Pamphile, J. A., & Polonio, J. C. (2019). Effects of textile dyes on health and the environment and bioremediation potential of living organisms. *Biotechnology Research and Innovation, 3*(2), 275-290.

Li, J., Shen, B., Hong, Z., Lin, B., Gao, B., & Chen, Y. (2012). A facile approach to synthesize novel oxygen-doped g-C 3 N 4 with superior visible-light photoreactivity. *Chemical communications, 48*(98), 12017-12019.

Li, J., Zhang, X., Raziq, F., Wang, J., Liu, C., Liu, Y., . . . Qin, C. (2017). Improved photocatalytic activities of g-C3N4 nanosheets by effectively trapping holes with halogen-induced surface polarization and 2, 4-dichlorophenol decomposition mechanism. *Applied Catalysis B: Environmental, 218*, 60-67.

Li, N., Tian, Y., Zhao, J., Zhang, J., Zuo, W., Kong, L., & Cui, H. (2018). Z-scheme 2D/3D g-C3N4@ ZnO with enhanced photocatalytic activity for cephalexin oxidation under solar light. *Chemical Engineering Journal, 352*, 412-422.

Li, W., Li, G., Sun, J., Zou, R., Xu, K., Sun, Y., . . . Hu, J. (2013). Hierarchical heterostructures of MnO 2 nanosheets or nanorods grown on Au-coated Co 3 O 4 porous nanowalls for high-performance pseudocapacitance. *Nanoscale, 5*(7), 2901-2908.

Li, X., Xiong, J., Gao, X., Huang, J., Feng, Z., Chen, Z., & Zhu, Y. (2019). Recent advances in 3D g-C3N4 composite photocatalysts for photocatalytic water splitting, degradation of pollutants and CO2 reduction. *Journal of Alloys and Compounds, 802*, 196-209.

Li, X., Yu, J., Low, J., Fang, Y., Xiao, J., & Chen, X. (2015). Engineering heterogeneous semiconductors for solar water splitting. *Journal of materials chemistry A, 3*(6), 2485-2534.

Li, X., Zhang, J., Shen, L., Ma, Y., Lei, W., Cui, Q., & Zou, G. (2009). Preparation and characterization of graphitic carbon nitride through pyrolysis of melamine. *Applied Physics A, 94*(2), 387-392.

Li, Y., Meng, M., Ji, C., Teng, S., Gao, L., Qu, R., . . . Zhang, Y. (2019). Soft-template synthesis of hybrid carbon and carbon nitride composites with enhanced photocatalytic activity for the degradation of methylene blue under visible light. *Environmental Progress & Sustainable Energy, 38*(5), 13186.

Li, Y., Wang, X., Huo, H., Li, Z., & Shi, J. (2020). A novel binary visible-light-driven photocatalyst type-I CdIn2S4/g-C3N4 heterojunctions coupling with H2O2: Synthesis, characterization, photocatalytic activity for Reactive Blue 19 degradation and mechanism analysis. *Colloids and Surfaces A: Physicochemical and Engineering Aspects, 587*, 124322.

Li, Y., Zhang, J., Wang, Q., Jin, Y., Huang, D., Cui, Q., & Zou, G. (2010). Nitrogen-rich carbon nitride hollow vessels: synthesis, characterization, and their properties. *The Journal of Physical Chemistry B, 114*(29), 9429-9434.

Lin, B., Xue, C., Yan, X., Yang, G., Yang, G., & Yang, B. (2015). Facile fabrication of novel SiO2/g-C3N4 core–shell nanosphere photocatalysts with enhanced visible light activity. *Applied Surface Science, 357*, 346-355.

Liu, C., Dong, S., & Chen, Y. (2019). Enhancement of visible-light-driven photocatalytic activity of carbon plane/g-C3N4/TiO2 nanocomposite by improving heterojunction contact. *Chemical Engineering Journal, 371*, 706-718.

Liu, F., Su, H., Jin, L., Zhang, H., Chu, X., & Yang, W. (2017). Facile synthesis of ultrafine cobalt oxide nanoparticles for high-performance supercapacitors. *Journal of colloid and interface science, 505*, 796-804.

Liu, G., Niu, P., Sun, C., Smith, S. C., Chen, Z., Lu, G. Q., & Cheng, H.-M. (2010). Unique electronic structure induced high photoreactivity of sulfur-doped graphitic C3N4. *Journal of the American Chemical Society, 132*(33), 11642-11648.

Liu, H., Zhong, L., Govindaraju, S., & Yun, K. (2019). ZnO rod decorated with Ag nanoparticles for enhanced photocatalytic degradation of methylene blue. *Journal of physics and chemistry of solids, 129*, 46-53.

Liu, L., Ma, D., Zheng, H., Li, X., Cheng, M., & Bao, X. (2008). Synthesis and characterization of microporous carbon nitride. *Microporous and Mesoporous Materials, 110*(2-3), 216-222.

Liu, W., Wang, M., Xu, C., & Chen, S. (2012). Facile synthesis of g-C3N4/ZnO composite with enhanced visible light photooxidation and photoreduction properties. *Chemical Engineering Journal, 209*, 386-393.

Liu, X., Jin, A., Jia, Y., Xia, T., Deng, C., Zhu, M., . . . Chen, X. (2017). Synergy of adsorption and visible-light photocatalytic degradation of methylene blue by a bifunctional Z-scheme heterojunction of WO3/g-C3N4. *Applied Surface Science, 405*, 359-371.

Liu, X., Tang, R.-Y., Xia, X.-M., Qin, Y.-Y., & Zhang, X. (2020). The study of visible-light photocatalytic degradation activity of Ag doped g-C3N4 obtained by heating process. *Materials Research Express, 7*(11), 115904.

Liu, Y., Shen, S., Li, Z., Ma, D., Xu, G., & Fang, B. (2021). Mesoporous g-C3N4 nanosheets with improved photocatalytic performance for hydrogen evolution. *Materials Characterization, 174*, 111031.

Liu, Y., Yu, Y.-X., & Zhang, W.-D. (2014). Photoelectrochemical study on charge transfer properties of nanostructured Fe2O3 modified by g-C3N4. *International journal of hydrogen energy, 39*(17), 9105-9113.

Long, Y., Yuan, C., Wang, X., Jin, D., Zhou, H., Wang, Q., . . . Wang, Q. (2021). Dielectric barrier discharge plasma-assisted modification of g-C3N4/Ag2O/TiO2-NRs composite enhanced photoelectrocatalytic activity. *Journal of Environmental Sciences, 104*, 113-127.

Lu, Q., Deng, J., Hou, Y., Wang, H., Li, H., & Zhang, Y. (2015). One-step electrochemical synthesis of ultrathin graphitic carbon nitride nanosheets and their application to the detection of uric acid. *Chemical Communications, 51*(61), 12251-12253.

Lu, X., Xu, K., Chen, P., Jia, K., Liu, S., & Wu, C. (2014). Facile one step method realizing scalable production of gC 3 N 4 nanosheets and study of their photocatalytic H 2 evolution activity. *Journal of materials chemistry A, 2*(44), 18924-18928.

Luque, A., & Hegedus, S. (2011). *Handbook of photovoltaic science and engineering*: John Wiley & Sons.

Maeda, K., Wang, X., Nishihara, Y., Lu, D., Antonietti, M., & Domen, K. (2009). Photocatalytic activities of graphitic carbon nitride powder for water reduction and oxidation under visible light. *The Journal of Physical Chemistry C, 113*(12), 4940-4947.

Mamba, G., & Mishra, A. (2016). Graphitic carbon nitride (g-C3N4) nanocomposites: a new and exciting generation of visible light driven photocatalysts for environmental pollution remediation. *Applied Catalysis B: Environmental, 198*, 347-377.

Manimozhi, R., Mathankumar, M., & Prakash, A. G. (2021). Synthesis of g-C3N4/ZnO heterostructure photocatalyst for enhanced visible degradation of organic dye. *Optik, 229*, 165548.

Mansournia, M., & Rakhshan, N. (2016). Amine ligand-based hydrothermal synthesis of Co3O4 nanoparticles, characterization and magnetic study. *Journal of Molecular Structure, 1125*, 714-720.

Meng, N., Ren, J., Liu, Y., Huang, Y., Petit, T., & Zhang, B. (2018). Engineering oxygen-containing and amino groups into two-dimensional atomically-thin porous polymeric carbon nitrogen for enhanced photocatalytic hydrogen production. *Energy & Environmental Science, 11*(3), 566-571.

Mishra, B. P., & Parida, K. (2021). Orienting Z scheme charge transfer in graphitic carbon nitride-based systems for photocatalytic energy and environmental applications. *Journal of materials chemistry A, 9*(16), 10039-10080.

Mishra, P., Patnaik, S., & Parida, K. (2019). An overview of recent progress on noble metal modified magnetic Fe 3 O 4 for photocatalytic pollutant degradation and H 2 evolution. *Catalysis Science & Technology, 9*(4), 916-941.

Mishra, P. M., Pattnaik, S., & Devi, A. P. (2021). Green synthesis of bio-based Au@ g-C3N4 nanocomposite for photocatalytic degradation of methyl orange. *Materials Today: Proceedings, 47*, 1218-1223.

Morán, J. I., Alvarez, V. A., Cyras, V. P., & Vázquez, A. (2008). Extraction of cellulose and preparation of nanocellulose from sisal fibers. *Cellulose, 15*(1), 149-159.

Mousavi, M., & Habibi-Yangjeh, A. (2015). Ternary g-C3N4/Fe3O4/Ag3VO4 nanocomposites: novel magnetically separable visible-light-driven photocatalysts for efficiently degradation of dye pollutants. *Materials Chemistry and Physics, 163*, 421-430.

Na, S., Seo, S., & Lee, H. (2020). Recent developments of advanced Ti3+-self-doped TiO2 for efficient visible-light-driven photocatalysis. *Catalysts, 10*(6), 679.

Niu, P., Zhang, L., Liu, G., & Cheng, H. M. (2012). Graphene-like carbon nitride nanosheets for improved photocatalytic activities. *Advanced Functional Materials, 22*(22), 4763-4770.

O'neill, C., Lopez, A., Esteves, S., Hawkes, F., Hawkes, D., & Wilcox, S. (2000). Azo-dye degradation in an anaerobic-aerobic treatment system operating on simulated textile effluent. *Applied microbiology and biotechnology, 53*(2), 249-254.

Ong, W.-J., Tan, L.-L., Ng, Y. H., Yong, S.-T., & Chai, S.-P. (2016). Graphitic carbon nitride (g-C3N4)-based photocatalysts for artificial photosynthesis and environmental remediation: are we a step closer to achieving sustainability? *Chemical reviews, 116*(12), 7159-7329.

Opoku, F., Govender, K. K., van Sittert, C. G. C. E., & Govender, P. P. (2018). Insights into the photocatalytic mechanism of mediator-free direct Z-scheme g-C3N4/Bi2MoO6 (010) and g-C3N4/Bi2WO6 (010) heterostructures: a hybrid density functional theory study. *Applied Surface Science, 427*, 487-498.

Ou, B., Wang, J., Wu, Y., Zhao, S., & Wang, Z. (2019). Degradation of aniline by photoelectro-Fenton process using g-C3N4 based cathode. *Journal of Electroanalytical Chemistry, 848*, 113273.

Palanisamy, G., Bhuvaneswari, K., Srinivasan, M., Vignesh, S., Elavarasan, N., Venkatesh, G., . . . Ramasamy, P. (2021). Two-dimensional g-C3N4 nanosheets supporting Co3O4-V2O5 nanocomposite for remarkable photodegradation of mixed organic dyes based on a dual Z-scheme photocatalytic system. *Diamond and Related Materials, 118*, 108540.

Panneri, S., Ganguly, P., Mohan, M., Nair, B. N., Mohamed, A. A. P., Warrier, K. G., & Hareesh, U. (2017). Photoregenerable, bifunctional granules of carbon-doped g-C3N4 as adsorptive photocatalyst for the efficient removal of tetracycline antibiotic. *ACS Sustainable Chemistry & Engineering, 5*(2), 1610-1618.

Patra, S. K., Rahut, S., & Basu, J. K. (2018). Enhanced Z-scheme photocatalytic activity of a π-conjugated heterojunction: MIL-53 (Fe)/Ag/gC 3 N 4. *New Journal of Chemistry, 42*(23), 18598-18607.

Peng, L., Zheng, R.-r., Feng, D.-w., Yu, H., & Dong, X.-t. (2020). Synthesis of eco-friendly porous g-C3N4/SiO2/SnO2 composite with excellent visible-light responsive photocatalysis. *Arabian Journal of Chemistry, 13*(2), 4275-4285.

Putri, L. K., Ng, B.-J., Er, C.-C., Ong, W.-J., Chang, W. S., Mohamed, A. R., & Chai, S.-P. (2020). Insights on the impact of doping levels in oxygen-doped gC3N4 and its effects on photocatalytic activity. *Applied Surface Science, 504*, 144427.

Qamar, M. A., Shahid, S., Javed, M., Sher, M., Iqbal, S., Bahadur, A., & Li, D. (2021). Fabricated novel g-C3N4/Mn doped ZnO nanocomposite as highly active photocatalyst for the disinfection of pathogens and degradation of the organic pollutants from wastewater under sunlight radiations. *Colloids and Surfaces A: Physicochemical and Engineering Aspects, 611*, 125863.

Qin, Y., Li, H., Dong, H., Ma, C., Li, X., Liu, X., . . . Yan, Y. (2018). Enhanced photocatalytic performance and stability of visible-light-driven Z-scheme CdS/Ag/gC 3 N 4 nanosheets photocatalyst. *New Journal of Chemistry, 42*(15), 12437-12448.

Rajeshwar, K., Osugi, M., Chanmanee, W., Chenthamarakshan, C., Zanoni, M. V. B., Kajitvichyanukul, P., & Krishnan-Ayer, R. (2008). Heterogeneous photocatalytic treatment of organic dyes in air and aqueous media. *Journal of photochemistry and photobiology C: photochemistry reviews, 9*(4), 171-192.

Ran, J., Ma, T. Y., Gao, G., Du, X.-W., & Qiao, S. Z. (2015). Porous P-doped graphitic carbon nitride nanosheets for synergistically enhanced visible-light photocatalytic H 2 production. *Energy & Environmental Science, 8*(12), 3708-3717.

Rono, N., Kibet, J. K., Martincigh, B. S., & Nyamori, V. O. (2021). A comparative study between thermal etching and liquid exfoliation of bulk graphitic carbon nitride to nanosheets for the photocatalytic degradation of a model environmental pollutant, Rhodamine B. *Journal of Materials Science: Materials in Electronics, 32*(1), 687-706.

Sahoo, D. P., Das, K. K., Patnaik, S., & Parida, K. (2020). Double charge carrier mechanism through 2D/2D interface-assisted ultrafast water reduction and antibiotic degradation over architectural S, P co-doped gC 3 N 4/ZnCr LDH photocatalyst. *Inorganic Chemistry Frontiers, 7*(19), 3695-3717.

Sang, Y., Liu, H., & Umar, A. (2015). Photocatalysis from UV/Vis to near-infrared light: towards full solar-light spectrum activity. *ChemCatChem, 7*(4), 559-573.

Schaber, P., Colson, J., Higgins, S., & Thielen, D. (2004). B. Anspach, Brauer J. *Thermochim. Acta, 424*, 131-142.

Schneider, J., Matsuoka, M., Takeuchi, M., Zhang, J., Horiuchi, Y., Anpo, M., & Bahnemann, D. W. (2014). Understanding TiO2 photocatalysis: mechanisms and materials. *Chemical reviews, 114*(19), 9919-9986.

Schwinghammer, K., Mesch, M. B., Duppel, V., Ziegler, C., Senker, J. r., & Lotsch, B. V. (2014). Crystalline carbon nitride nanosheets for improved visible-light hydrogen evolution. *Journal of the American Chemical Society, 136*(5), 1730-1733.

Seddiqi, H., Oliaei, E., Honarkar, H., Jin, J., Geonzon, L. C., Bacabac, R. G., & Klein-Nulend, J. (2021). Cellulose and its derivatives: Towards biomedical applications. *Cellulose, 28*(4), 1893-1931.

Sobahi, T. R., & Amin, M. (2019). Upgrading the photocatalytic achievement of g-C3N4 nanosheets along decoration with Ag@ TiO2 nanospheres for the preparation of vitamin B3. *Applied Nanoscience, 9*(8), 1621-1636.

Song, L., Zhang, S., Wu, X., & Wei, Q. (2012). A metal-free and graphitic carbon nitride sonocatalyst with high sonocatalytic activity for degradation methylene blue. *Chemical Engineering Journal, 184*, 256-260.

Starukh, H., & Praus, P. (2020). Doping of graphitic carbon nitride with non-metal elements and its applications in photocatalysis. *Catalysts, 10*(10), 1119.

Tachibana, Y., Vayssieres, L., & Durrant, J. R. (2012). Artificial photosynthesis for solar water-splitting. *Nature Photonics, 6*(8), 511-518.

Tang, C.-W., Wang, C.-B., & Chien, S.-H. (2008). Characterization of cobalt oxides studied by FT-IR, Raman, TPR and TG-MS. *Thermochimica Acta, 473*(1-2), 68-73.

Tay, Q., Kanhere, P., Ng, C. F., Chen, S., Chakraborty, S., Huan, A. C. H., . . . Chen, Z. (2015). Defect engineered g-C3N4 for efficient visible light photocatalytic hydrogen production. *Chemistry of Materials, 27*(14), 4930-4933.

Teter, D. M., & Hemley, R. J. (1996). Low-compressibility carbon nitrides. *Science, 271*(5245), 53-55.

Thomas, A., Fischer, A., Goettmann, F., Antonietti, M., Müller, J.-O., Schlögl, R., & Carlsson, J. M. (2008). Graphitic carbon nitride materials: variation of structure and morphology and their use as metal-free catalysts. *Journal of Materials Chemistry, 18*(41), 4893-4908.

Thorat, N., Yadav, A., Yadav, M., Gupta, S., Varma, R., Pillai, S., . . . Patel, N. (2019). Ag loaded B-doped-g C3N4 nanosheet with efficient properties for photocatalysis. *Journal of environmental management, 247*, 57-66.

Tian, J., Liu, Q., Asiri, A. M., Sun, X., & He, Y. (2015). Ultrathin graphitic C3N4 nanofibers: hydrolysis-driven top-down rapid synthesis and application as a novel fluorosensor for rapid, sensitive, and selective detection of Fe3+. *Sensors and Actuators B: Chemical, 216*, 453-460.

Tonda, S., Kumar, S., Kandula, S., & Shanker, V. (2014). Fe-doped and-mediated graphitic carbon nitride nanosheets for enhanced photocatalytic performance under natural sunlight. *Journal of materials chemistry A, 2*(19), 6772-6780.

Tong, Z., Yang, D., Shi, J., Nan, Y., Sun, Y., & Jiang, Z. (2015). Three-dimensional porous aerogel constructed by g-C3N4 and graphene oxide nanosheets with excellent visible-light photocatalytic performance. *ACS applied materials & interfaces, 7*(46), 25693-25701.

Umena, Y., Kawakami, K., Shen, J.-R., & Kamiya, N. (2011). Crystal structure of oxygen-evolving photosystem II at a resolution of 1.9 Å. *nature, 473*(7345), 55-60.

Vinodgopal, K., & Kamat, P. V. (1995). Enhanced rates of photocatalytic degradation of an azo dye using SnO2/TiO2 coupled semiconductor thin films. *Environmental science & technology, 29*(3), 841-845.

Wang, C.-H., Qin, D.-D., Shan, D.-L., Gu, J., Yan, Y., Chen, J., . . . Quan, J.-J. (2017). Assembly of gC 3 N 4-based type II and Z-scheme heterojunction anodes with improved charge separation for photoelectrojunction water oxidation. *Physical Chemistry Chemical Physics, 19*(6), 4507-4515.

Wang, J.-C., Cui, C.-X., Kong, Q.-Q., Ren, C.-Y., Li, Z., Qu, L., . . . Jiang, K. (2018). Mn-Doped g-C3N4 nanoribbon for efficient visible-light photocatalytic water splitting coupling with methylene blue degradation. *ACS Sustainable Chemistry & Engineering, 6*(7), 8754-8761.

Wang, J., Chen, R., Xiang, L., & Komarneni, S. (2018). Synthesis, properties and applications of ZnO nanomaterials with oxygen vacancies: A review. *Ceramics International, 44*(7), 7357-7377.

Wang, K., Li, Q., Liu, B., Cheng, B., Ho, W., & Yu, J. (2015). Sulfur-doped g-C3N4 with enhanced photocatalytic CO2-reduction performance. *Applied Catalysis B: Environmental, 176*, 44-52.

Wang, W., Yu, J. C., Xia, D., Wong, P. K., & Li, Y. (2013). Graphene and g-C3N4 nanosheets cowrapped elemental α-sulfur as a novel metal-free heterojunction photocatalyst for bacterial inactivation under visible-light. *Environmental science & technology, 47*(15), 8724-8732.

Wang, X., Blechert, S., & Antonietti, M. (2012). Polymeric graphitic carbon nitride for heterogeneous photocatalysis. ACS Catal 2: 1596–1606.

Wang, X., Maeda, K., Thomas, A., Takanabe, K., Xin, G., Carlsson, J. M., . . . Antonietti, M. (2009). A metal-free polymeric photocatalyst for hydrogen production from water under visible light. *Nature materials, 8*(1), 76-80.

Wang, Y., Di, Y., Antonietti, M., Li, H., Chen, X., & Wang, X. (2010). Excellent visible-light photocatalysis of fluorinated polymeric carbon nitride solids. *Chemistry of Materials, 22*(18), 5119-5121.

Wang, Y., Li, Y., Bai, X., Cai, Q., Liu, C., Zuo, Y., . . . Cui, L. (2016). Facile synthesis of Y-doped graphitic carbon nitride with enhanced photocatalytic performance. *Catalysis Communications, 84*, 179-182.

Wang, Y., Wang, F., Zuo, Y., Zhang, X., & Cui, L.-F. (2014). Simple synthesis of ordered cubic mesoporous graphitic carbon nitride by chemical vapor deposition method using melamine. *Materials Letters, 136*, 271-273.

Wang, Y., Wang, X., & Antonietti, M. (2012). Polymeric graphitic carbon nitride as a heterogeneous organocatalyst: from photochemistry to multipurpose catalysis to sustainable chemistry. *Angewandte Chemie International Edition, 51*(1), 68-89.

Wang, Y., Wang, Y., Li, Y., Shi, H., Xu, Y., Qin, H., . . . Cui, L. (2015). Simple synthesis of Zr-doped graphitic carbon nitride towards enhanced photocatalytic performance under simulated solar light irradiation. *Catalysis Communications, 72*, 24-28.

Wang, Y., Xu, Y., Wang, Y., Qin, H., Li, X., Zuo, Y., . . . Cui, L. (2016). Synthesis of Mo-doped graphitic carbon nitride catalysts and their photocatalytic activity in the reduction of CO2 with H2O. *Catalysis Communications, 74*, 75-79.

Wang, Y., Yu, D., Wang, W., Gao, P., Zhong, S., Zhang, L., . . . Liu, B. (2020). Synthesizing Co3O4-BiVO4/g-C3N4 heterojunction composites for superior photocatalytic redox activity. *Separation and Purification Technology, 239*, 116562.

Wang, Z.-T., Xu, J.-L., Zhou, H., & Zhang, X. (2019). Facile synthesis of Zn (II)-doped g-C3N4 and their enhanced photocatalytic activity under visible light irradiation. *Rare Metals, 38*(5), 459-467.

Wang, Z., Guan, W., Sun, Y., Dong, F., Zhou, Y., & Ho, W.-K. (2015). Water-assisted production of honeycomb-like gC 3 N 4 with ultralong carrier lifetime and outstanding photocatalytic activity. *Nanoscale, 7*(6), 2471-2479.

Wei, K., Faraj, Y., Yao, G., Xie, R., & Lai, B. (2021). Strategies for improving perovskite photocatalysts reactivity for organic pollutants degradation: A review on recent progress. *Chemical Engineering Journal, 414*, 128783.

Wen, J., Xie, J., Chen, X., & Li, X. (2017). A review on g-C3N4-based photocatalysts. *Applied Surface Science, 391*, 72-123.

Wu, Y., Song, M., Chai, Z., Huang, J., & Wang, X. (2020). Facile construction of bi2moo6/bi/g-c3n4 toward efficient photocatalytic oxidation of indoor gaseous formaldehyde with a wide concentration range under visible light irradiation. *ACS Sustainable Chemistry & Engineering, 8*(20), 7710-7720.

Wu, Y., Wang, H., Sun, Y., Xiao, T., Tu, W., Yuan, X., . . . Chew, J. W. (2018). Photogenerated charge transfer via interfacial internal electric field for significantly improved photocatalysis in direct Z-scheme oxygen-doped carbon nitrogen/CoAl-layered double hydroxide heterojunction. *Applied Catalysis B: Environmental, 227*, 530-540.

Xia, P., Zhu, B., Cheng, B., Yu, J., & Xu, J. (2018). 2D/2D g-C3N4/MnO2 nanocomposite as a direct Z-scheme photocatalyst for enhanced photocatalytic activity. *ACS Sustainable Chemistry & Engineering, 6*(1), 965-973.

Xiang, Q., Yu, J., & Jaroniec, M. (2011). Preparation and enhanced visible-light photocatalytic H2-production activity of graphene/C3N4 composites. *The Journal of Physical Chemistry C, 115*(15), 7355-7363.

Xiong, T., Cen, W., Zhang, Y., & Dong, F. (2016). Bridging the g-C3N4 interlayers for enhanced photocatalysis. *Acs Catalysis, 6*(4), 2462-2472.

Xu, J., Brenner, T. J., Chen, Z., Neher, D., Antonietti, M., & Shalom, M. (2014). Upconversion-agent induced improvement of g-C3N4 photocatalyst under visible light. *ACS Applied Materials & Interfaces, 6*(19), 16481-16486.

Xu, J., & Shalom, M. (2016). Electrophoretic deposition of carbon nitride layers for photoelectrochemical applications. *ACS Applied Materials & Interfaces, 8*(20), 13058-13063.

Xu, J., Wu, H.-T., Wang, X., Xue, B., Li, Y.-X., & Cao, Y. (2013). A new and environmentally benign precursor for the synthesis of mesoporous gC 3 N 4 with tunable surface area. *Physical Chemistry Chemical Physics, 15*(13), 4510-4517.

Xu, M., Han, L., & Dong, S. (2013). Facile fabrication of highly efficient g-C3N4/Ag2O heterostructured photocatalysts with enhanced visible-light photocatalytic activity. *ACS applied materials & interfaces, 5*(23), 12533-12540.

Xu, Q., Zhang, L., Cheng, B., Fan, J., & Yu, J. (2020). S-scheme heterojunction photocatalyst. *Chem, 6*(7), 1543-1559.

Xu, Y., & Gao, S.-P. (2012). Band gap of C3N4 in the GW approximation. *International journal of hydrogen energy, 37*(15), 11072-11080.

Yadav, R. M., Kumar, R., Aliyan, A., Dobal, P. S., Biradar, S., Vajtai, R., . . . Ajayan, P. M. (2020). Facile synthesis of highly fluorescent free-standing films comprising graphitic carbon nitride (gC 3 N 4) nanolayers. *New Journal of Chemistry, 44*(6), 2644-2651.

Yaghoubi, H., Li, Z., Chen, Y., Ngo, H. T., Bhethanabotla, V. R., Joseph, B., . . . Takshi, A. (2015). Toward a visible light-driven photocatalyst: the effect of midgap-states-induced energy gap of undoped TiO2 nanoparticles. *Acs Catalysis, 5*(1), 327-335.

Yan, S., Li, Z., & Zou, Z. (2009). Photodegradation performance of g-C3N4 fabricated by directly heating melamine. *Langmuir, 25*(17), 10397-10401.

Yan, S., Lv, S., Li, Z., & Zou, Z. (2010). Organic–inorganic composite photocatalyst of gC 3 N 4 and TaON with improved visible light photocatalytic activities. *Dalton Transactions, 39*(6), 1488-1491.

Yang, L., Liu, X., Liu, Z., Wang, C., Liu, G., Li, Q., & Feng, X. (2018). Enhanced photocatalytic activity of g-C3N4 2D nanosheets through thermal exfoliation using dicyandiamide as precursor. *Ceramics International, 44*(17), 20613-20619.

Yang, N., Lv, X., Zhong, S., Qian, D., Han, S., Li, D., . . . Jiang, W. (2018). Preparation of Z-scheme AgI/Bi 5 O 7 I plate with high visible light photocatalytic performance by phase transition and morphological transformation of BiOI microspheres at room temperature. *Dalton Transactions, 47*(33), 11420-11428.

Yang, S., Gong, Y., Zhang, J., Zhan, L., Ma, L., Fang, Z., . . . Ajayan, P. M. (2013). Exfoliated graphitic carbon nitride nanosheets as efficient catalysts for hydrogen evolution under visible light. *Advanced materials, 25*(17), 2452-2456.

Yang, Y., Guo, W., Guo, Y., Zhao, Y., Yuan, X., & Guo, Y. (2014). Fabrication of Z-scheme plasmonic photocatalyst Ag@ AgBr/g-C3N4 with enhanced visible-light photocatalytic activity. *Journal of hazardous materials, 271*, 150-159.

Ye, S., Wang, R., Wu, M.-Z., & Yuan, Y.-P. (2015). A review on g-C3N4 for photocatalytic water splitting and CO2 reduction. *Applied Surface Science, 358*, 15-27.

Yi, X.-H., Ma, S.-Q., Du, X.-D., Zhao, C., Fu, H., Wang, P., & Wang, C.-C. (2019). The facile fabrication of 2D/3D Z-scheme g-C3N4/UiO-66 heterojunction with enhanced photocatalytic Cr (VI) reduction performance under white light. *Chemical Engineering Journal, 375*, 121944.

Yin, S., Di, J., Li, M., Sun, Y., Xia, J., Xu, H., . . . Li, H. (2016). Ionic liquid-assisted synthesis and improved photocatalytic activity of pn junction g-C3N4/BiOCl. *Journal of Materials Science, 51*(10), 4769-4777.

Yin, S., Han, J., Zhou, T., & Xu, R. (2015). Recent progress in gC 3 N 4 based low cost photocatalytic system: activity enhancement and emerging applications. *Catalysis Science & Technology, 5*(12), 5048-5061.

Yu, B., Meng, F., Khan, M. W., Qin, R., & Liu, X. (2020). Synthesis of hollow TiO2@ g-C3N4/Co3O4 core-shell microspheres for effective photooxidation degradation of tetracycline and MO. *Ceramics International, 46*(9), 13133-13143.

Yu, Y., Zhou, Q., & Wang, J. (2016). The ultra-rapid synthesis of 2D graphitic carbon nitride nanosheets via direct microwave heating for field emission. *Chemical Communications, 52*(16), 3396-3399.

Yuan, J., Yi, X., Tang, Y., Liu, C., & Luo, S. (2020). Efficient photocatalytic hydrogen evolution and CO2 reduction: enhanced light absorption, charge separation, and hydrophilicity by tailoring terminal and linker units in g-C3N4. *ACS applied materials & interfaces, 12*(17), 19607-19615.

Yuan, S., Li, Z., & Wang, Y. (2013). Effective degradation of methylene blue by a novel electrochemically driven process. *Electrochemistry Communications, 29*, 48-51.

Zhang, J., Chen, X., Takanabe, K., Maeda, K., Domen, K., Epping, J. D., . . . Wang, X. (2010). Synthesis of a carbon nitride structure for visible-light catalysis by copolymerization. *Angewandte Chemie International Edition, 49*(2), 441-444.

Zhang, J., Chen, Y., & Wang, X. (2015). Two-dimensional covalent carbon nitride nanosheets: synthesis, functionalization, and applications. *Energy & Environmental Science, 8*(11), 3092-3108.

Zhang, J., Guo, F., & Wang, X. (2013). An optimized and general synthetic strategy for fabrication of polymeric carbon nitride nanoarchitectures. *Advanced Functional Materials, 23*(23), 3008-3014.

Zhang, J., Hu, S., & Wang, Y. (2014). A convenient method to prepare a novel alkali metal sodium doped carbon nitride photocatalyst with a tunable band structure. *RSC Advances, 4*(108), 62912-62919.

Zhang, L., Wang, H., Chen, Z., Wong, P. K., & Liu, J. (2011). Bi2WO6 micro/nano-structures: synthesis, modifications and visible-light-driven photocatalytic applications. *Applied Catalysis B: Environmental, 106*(1-2), 1-13.

Zhang, M., Zhang, Y., Tang, L., Zeng, G., Wang, J., Zhu, Y., . . . He, W. (2019). Ultrathin Bi2WO6 nanosheets loaded g-C3N4 quantum dots: A direct Z-scheme photocatalyst with enhanced photocatalytic activity towards degradation of organic pollutants under wide spectrum light irradiation. *Journal of colloid and interface science, 539*, 654-664.

Zhang, N., Yang, M.-Q., Liu, S., Sun, Y., & Xu, Y.-J. (2015). Waltzing with the versatile platform of graphene to synthesize composite photocatalysts. *Chemical reviews, 115*(18), 10307-10377.

Zhang, X.-S., Tian, K., Hu, J.-Y., & Jiang, H. (2015). Significant enhancement of photoreactivity of graphitic carbon nitride catalysts under acidic conditions and the underlying H+-mediated mechanism. *Chemosphere, 141*, 127-133.

Zhang, Y., Thomas, A., Antonietti, M., & Wang, X. (2009). Activation of carbon nitride solids by protonation: morphology changes, enhanced ionic conductivity, and photoconduction experiments. *Journal of the American Chemical Society, 131*(1), 50-51.

Zhao, K., Khan, I., Qi, K., Liu, Y., & Khataee, A. (2020). Ionic liquid assisted preparation of phosphorus-doped g-C3N4 photocatalyst for decomposition of emerging water pollutants. *Materials Chemistry and Physics, 253*, 123322.

Zhao, X., Lu, Z., Wei, M., Zhang, M., Dong, H., Yi, C., . . . Yan, Y. (2018). Synergetic effect of carbon sphere derived from yeast with magnetism and cobalt oxide nanochains towards improving photodegradation activity for various pollutants. *Applied Catalysis B: Environmental, 220*, 137-147.

Zheng, Q., Durkin, D. P., Elenewski, J. E., Sun, Y., Banek, N. A., Hua, L., . . . Shuai, D. (2016). Visible-light-responsive graphitic carbon nitride: rational design and photocatalytic applications for water treatment. *Environmental science & technology, 50*(23), 12938-12948.

Zheng, Q., Shen, H., & Shuai, D. (2017). Emerging investigators series: advances and challenges of graphitic carbon nitride as a visible-light-responsive photocatalyst for sustainable water purification. *Environmental Science: Water Research & Technology, 3*(6), 982-1001.

Zheng, Y., Lin, L., Wang, B., & Wang, X. (2015). Graphitic carbon nitride polymers toward sustainable photoredox catalysis. *Angewandte Chemie International Edition, 54*(44), 12868-12884.

Zhou, L., Xu, Y., Yu, W., Guo, X., Yu, S., Zhang, J., & Li, C. (2016). Ultrathin two-dimensional graphitic carbon nitride as a solution-processed cathode interfacial layer for inverted polymer solar cells. *Journal of materials chemistry A, 4*(21), 8000-8004.

Zhou, L., Zhang, H., Sun, H., Liu, S., Tade, M. O., Wang, S., & Jin, W. (2016). Recent advances in non-metal modification of graphitic carbon nitride for photocatalysis: a historic review. *Catalysis Science & Technology, 6*(19), 7002-7023.

Zhou, P., Yu, J., & Jaroniec, M. (2014). All-solid-state Z-scheme photocatalytic systems. *Advanced Materials, 26*(29), 4920-4935.

Zhu, B., Xia, P., Li, Y., Ho, W., & Yu, J. (2017). Fabrication and photocatalytic activity enhanced mechanism of direct Z-scheme g-C3N4/Ag2WO4 photocatalyst. *Applied Surface Science, 391*, 175-183.

Zhu, J., Wei, Y., Chen, W., Zhao, Z., & Thomas, A. (2010). Graphitic carbon nitride as a metal-free catalyst for NO decomposition. *Chemical communications, 46*(37), 6965-6967.

Zhu, J., Xiao, P., Li, H., & Carabineiro, S. A. (2014). Graphitic carbon nitride: synthesis, properties, and applications in catalysis. *ACS applied materials & interfaces, 6*(19), 16449-16465.

Zhu, Y., Wan, T., Wen, X., Chu, D., & Jiang, Y. (2019). Tunable Type I and II heterojunction of CoOx nanoparticles confined in g-C3N4 nanotubes for photocatalytic hydrogen production. *Applied Catalysis B: Environmental, 244*, 814-822.